Spring 2022

INVESTIGATION OF THE STRUCTURE, CHEMISTRY AND FUNCTIONAL PERFORMANCE OF NOVEL BIOCHARS

Julie Elizabeth Muretta

INVESTIGATION OF THE STRUCTURE, CHEMISTRY AND FUNCTIONAL PERFORMANCE OF NOVEL BIOCHARS

by

Julie Elizabeth Muretta

A dissertation submitted in partial fulfillment of the
requirements for the degree of

Doctor of Philosophy:
Materials Science

Montana Technological University
2022

INVESTIGATION OF THE STRUCTURE, CHEMISTRY AND FUNCTIONAL PERFORMANCE OF NOVEL BIOCHARS

By

JULIE ELIZABETH MURETTA

M.S., Montana State University, Bozeman, MT, 2018
B.S., Montana State University, Bozeman, MT, 2013

Dissertation
presented in partial fulfillment of the requirements
for the degree of

Doctor of Philosophy
in Materials Science

Montana Technological University
Butte, MT

April 2022

Approved by:

Dario Prieto-Centurion, Co-Chair
Mechanical Engineering Department

John D. Kirtley, Co-Chair
Chemistry and Geochemistry Department

Jerome Downey
Metallurgical and Materials Engineering Department

Robert A. Walker
Chemistry and Biochemistry, Montana State University

Angela Lueking, Dean
Montana Technological University Graduate School

Muretta, Julie, Ph.D., April 2022

Investigation of the Structure, Chemistry and Functional Performance of Novel Biochars

Co-Chairperson: Dario Prieto-Centurion

Co-Chairperson: John D. Kirtley

Biochars are a class of carbonaceous materials possessing high degrees of structural and chemical disorder in both organic and inorganic constituent phases. Despite this disorder, and in some cases because of this disorder, biochars have shown strong performance in adsorbing and even sequestering contaminants from soil, surface water and air. Biochar is the carbonaceous, solid product of heating carbonaceous feedstock in an oxygen-limited environment above 250°C, usually sourced from inexpensive, locally available agricultural and forestry wastes which can otherwise be difficult and expensive to dispose of. Biochar possesses attractive functional properties like high specific surface area, high micropore volume, and tunable surface chemistry which are key to performance in separation technologies and environmental remediation. In this work, two high-performing biochars were investigated: one from cottonwood feedstock and one sourced from locally available bovine bone waste. In the wood-based biochar, the synergistic impacts of potassium content and lignin microstructure were investigated for their role in determining biochar structure and function. The performance of these biochars was tested in dynamic adsorption of gaseous ammonia, a growing threat to human and environmental health, in which all biochars outperformed a commercial activated carbon. Breakthrough times showed no correlation with surface area of the adsorbents, contrary to expectation. Biochar sourced from pyrolyzed bovine bone has shown strong performance against a range of other materials in removing Cu^{2+} from acid mine waste. In-depth characterization of the mineral and organic phases of this novel biochar revealed that disorder may be key to its strong performance in Cu^{2+} removal.

Keywords: Biochar, Bone Char, Ammonia Breakthrough, Porous Carbon

Dedication

I dedicate this dissertation to my children, Harry, Elizabeth, and Benjamin. Being a grad student parent is challenging, but it is even more challenging for your children. I love you with all of my being and am so thankful every day for your love and proud of who you have become. Always keep the light of learning, and always remember:

> "Nothing in this world can take the place of persistence. Talent will not: nothing is more common than unsuccessful men with talent. Genius will not; unrewarded genius is almost a proverb. Education will not: the world is full of educated derelicts. Persistence and determination alone are omnipotent." – Calvin Coolidge

Acknowledgements

I would first and foremost like to thank my family – my kids, my brother and sister, and my mother - who have given me unbelievable moral support through all of this. Without them this could not have happened. Thank you all. I love you. This is for you. I would also like to thank Dr. Beverly Hartline for encouragement to come back to grad school and for providing initial funding. I am also grateful for your example of personal and professional excellence, your mentorship and your friendship. Thank you to my two co-advisers, Dr. Dario Prieto-Centurion and Dr. John Kirtley, for excellence in mentoring and teaching. You have set a superb example for me to follow in all future endeavors. Your dedication to and support of this Ph.D. in the face of a pandemic was exceptional and I am so grateful. Thank you to all my committee members: Dr. Jerome Downey, Dr. Rob Walker, and Dr. Karen Wesenberg. Your commitment to my Ph.D. and to the program is admirable and greatly appreciated. Thank you also to Dr. Richard LaDouceur and Dr. Ronald White for continued support through access to lab resources and funding. I could not have finished this without your support. A great many others have contributed to this work and it is certain that this Ph.D. could not have been completed otherwise. First and foremost, tremendous thanks to Jade Uriarte and Gia Luciano, for laboratory assistance and biochar preparation. Thanks to Max Wohlgenant for biochar furnace work and keeping it running. Thanks to Dalton Compton and Dr. Nicholas Stadie (Montana State University, Chemistry and Biochemistry) for nitrogen adsorption measurements. And thanks to so many others who provided discussion, assistance, training, or instrumentation. Your contributions made this Ph.D. possible: Gary Wyss (CAMP), Dr. Cristina Stefanescu (CAMP), Nancy Oyer (CAMP), Dr. David Hutchins, Kristopher Bosch, Blaine Berrington, Abdul Sommed-Hadi, Daniel Goettlich, Kelsi Mcenaney, Dr. Alysia Cox, Eva Barahona, and Ashley Huft (MBMG). I would also like to extend special gratitude to Dr. Wellington Muchero (ORNL, Biosciences Division), for generously donating the biomass used in this study, and Dr. Arthur Ragauskas (University of Tennessee – Governor's Chair for Biorefining) and Dr. Chang Geun Yoo (SUNY-Syracuse, College of Environmental Science and Forestry) for allowing us to report their unpublished biomass compositional data. Finally, tremendous thanks to Army Research Labs for the continued financial support, it is greatly appreciated.

Research was sponsored by the Combat Capabilities Development Command Army Research Laboratory and was accomplished under Cooperative Agreement Number W911NF-20-2-0163. The views and conclusions contained in this document are those of the authors and should not be interpreted as representing the official policies, either expressed or implied, of the Combat Capabilities Development Command Army Research Laboratory or the U.S. Government.

Table of Contents

List of Tables

List of Figures

List of Equations

1. Introduction and Motivation

Since the beginning of the Industrial Revolution, human consumption of natural resources and associated emissions of pollutants has increased in rate and scope leading to destabilization of global nutrient cycles, reduced availability of fresh water, increase in global atmospheric particulate matter, especially $PM_{2.5}$, and climate destabilization [1,2]. Consumption of fossil fuels is responsible for a large percentage of these effects [1]. Other contributors include industrialized agriculture, mining, energy production, and industrial emissions and waste [3–6]. These pollutant sources have the cumulative effects of reducing air and water quality with far-reaching implications for human and ecological health and quality of life [7]. Much of the burden of air and water pollution is borne by those who are least responsible for creating it [7].

Ambient air quality is decreasing globally largely due to increasing concentrations of suspended particulate matter. Fossil fuel consumption, agriculture, industry and natural sources contribute to the formation of the most problematic pollutant, particulate matter less than 2.5 microns in size ($PM_{2.5}$) [5,8–10]. Agricultural sources, i.e. ammonia based fertilizer and manure from concentrated animal feeding operations produced 85% of global ammonia emission in 2015 [8]. Buildings and other industrial sources also represented significant sources [8]. Ammonia is toxic to humans at levels as low as 100 ppm [11]. Ammonia forms particulate matter by reacting with atmospheric NO_x and SO_x and dust particles in the atmosphere [9,12]. Recent efforts to reduce harmful NO_x and SO_x emissions from fossil fuel sources like coal combustion and vehicular emissions has compounded the problem because those technologies rely on ammonia as a reactant and have low efficiency [12]. According to the 2019 Global Burdens of Disease Study, $PM_{2.5}$ was responsible for 6.4 million premature human deaths and 93 billion days of illness globally, resulting in healthcare costs exceeding 9.1 trillion USD [6,7]. Ammonia-related

PM caries a heavy environmental cost, too, as it contributes to acidification of rain and surface waters, eutrophication of soil and water, and reduces biodiversity [9,11,12].

Poor water quality is another increasing problem largely driven by agriculture, industrial and mining activities, particularly in developing countries [2,13–17]. In those locations many people do not have access to water which has been adequately treated, instead relying on boiling, chlorination, or solar disinfection, which do not effectively remove many contaminants [15]. Contaminants like pesticide runoff and heavy metals from fossil fuel combustion, industrial and mining activities, are toxic to aquatic life and also disrupt the ecological nutrient balance, for instance creating toxic algal blooms [18,19]. Heavy metals are a primary sources of ground water and surface water pollution are difficult to mitigate because they come into direct contact with surface or groundwaters by natural processes like runoff [14,16,20]. Heavy metals toxification of surface waters is not just a problem for developing countries. Butte, MT is home to the largest superfund site in the United States due to ongoing copper and molybdenum mining activities close to the headwaters of the regional watershed and to the town's urban center [21]. Elevated levels of heavy metals persist in soils and surface waters in the area surrounding Butte despite decades of remediation, illustrating the tremendous challenges in remediating heavy metals pollution [21,22].

The effects of particulate matter, the nitrogen balance of soil and water, and the availability of fresh water have all been identified as key factors determining the stability of Earth's regulatory systems [1]. The safe threshold for the nitrogen cycle, global biodiversity and climate change have already been exceeded [1]. Ammonia emissions play a role in all of those systems therefore reducing global atmospheric ammonia emissions is paramount to reversing the trajectory toward global destabilization. While the safe threshold for availability of fresh water may not have been exceeded yet, the impacts of both air- and water-pollution on biodiversity are well-documented, and that threshold has been exceeded [1]. Current state of the art mitigation strategies for air- and water-borne pollutants can be challenging and very costly to implement and reduction in emissions may be the most effective long-term solution, however as the population grows, so do human-related activities that produce PM and water pollution [8]. The need for effective, locally-sourced and environmentally responsible mitigation strategies is greater than ever. It has been proposed that biochar can go far in meeting that need, however there are tremendous challenges associated with the development of the source-structure-function relationships needed to thoughtfully implement biochar in this capacity.

In the remainder of this chapter, adsorbent materials for gaseous ammonia and aqueous heavy metals removal are briefly introduced. Next, concepts of carbon bonding and the development of structure and surface chemistry of carbonaceous adsorbent materials are outlined briefly as they relate to adsorption. I will then discuss some technical background on dynamic adsorption. Finally, I will show how my Ph.D. research addresses ongoing challenges in developing source-structure-function relations for biochar and bone char, and provides new insight into the application of biochar in dynamic gas phase adsorption of ammonia.

1.1. Ammonia and Heavy Metals Pollution Mitigation Strategies

Ammonia, NH_3, is a highly corrosive basic molecule, which derives its reactivity from its pair of lone electrons. It is a strong proton acceptor (a Bronsted base) and will react easily with proton donors (Bronsted acids) like water. For instance, during respiratory exposure for humans, ammonia readily reacts with water to form NH_4OH, which can irritate or even permanently damage lung tissue [23]. Because of its high reactivity, safe exposure levels are very low. This can be challenging to achieve, making ammonia a notoriously problematic pollutant in gaseous form [9,11]. Adsorption has proven to be the most efficient and cost effective means of removal, with activated carbon and metal-organic-frameworks (MOFs) being the most often used for gaseous ammonia adsorption [11,24,25]. MOFs and other nanoporous materials have shown high potential for ammonia mitigation, however they are costly to produce, limiting their widespread use [26]. Activated carbon is much less costly, however carries the burden of a high carbon footprint due to the energy requirement in high temperature processing [27]. Biochar is a novel material which has shown promise in ammonia adsorption due to its oxygen-rich surface chemistry and high surface area [28–33]. Preliminary studies have indicated the potential for biochar only in quasi-static ammonia applications, however, and the potential for biochar in dynamic adsorption is only speculative at this point. Much more work is needed to determine its effectiveness in, for instance, removing ammonia from cement plant emissions streams or from synthetic ammonia plant emissions.

Strategies for heavy metals removal are highly dependent on the cation species and the pollutant mechanism. Cation exchange is an attractive and affordable solution but is highly selective [14]. Some treatment methods have inherent disadvantages, for instance zeolites are effective for cation exchange but are quite expensive, membrane filtration is subject to fouling, coagulation results in high burden of sludge removal and treatment and electrodialysis is energy intensive and has low output, therefore their application in, for instance acid mine waste cleanup, is likely to be limited [14,17]. Some of the most effective strategies are also the simplest to deploy, for instance adsorbent technologies represent the most efficient and affordable solutions, particularly for removal of multiple species at the same time [34]. Activated carbon is the most commonly used adsorbent for heavy metals adsorption attributed to its chemical inertness, non-specific adsorption and mechanical stability, however it can also be expensive and has lower capacity compared to other methods [34]. Another novel adsorbent technology which has shown great promise in metals remediation is biochar made from pyrolyzed animal bone [35,36]. The history of bone char in removing ash and colorants in sugar purification is well-documented and lends merit to the application of bone char in metals remediation [37–39]. In more recent laboratory batch experiments, bone char has been observed to remove heavy metals species by multiple mechanisms including cation exchange, dissolution/chemical precipitation and adsorption and outperforms granulated activated carbon and biomass-biochars [36,40]. The mechanism and capacity is largely determined by the pH of the solution and the metal species as well as the structure of the bone char, which is not well-understood [36,38]. More thorough characterization of bone char is needed to provide guidance in the appropriate preparation and application for environmental remediation of heavy metals-laden water such as the treatment of acid mine waste.

1.2. Description of Biochar

Biochar was originally defined as being product of thermochemical conversion of biomass under low oxygen conditions and moderate temperatures (< 700 °C) for use as a soil modifier [41]. Biochar is similar to charcoal and activated carbon in that they are all carbonaceous products of thermochemical conversion, however the processing and application originally differentiated them. Biochar originally referred to granulated, pyrolysis products which were meant for soil application, whereas charcoal refers to a fuel product for heat or energy generation [33,42,43]. Activated carbons are carefully designed porous materials processed by physical or chemical activation processes and multiple carbonization steps [27]. Now, the term biochar is applied more broadly than its previous delegated role as a soil amendment and generally refers to any carbonaceous product of pyrolysis formed from locally sourced biomass feedstock. The range of applications has become similarly broad, with biochars being used for soil improvement and carbon sequestration as well as more technical applications like adsorption and electrochemical technologies [44,45]. The functional properties of biochars are highly dependent on the heating conditions and on the type of feedstock, challenging the development of a source-structure-function relationship.

1.3. Impacts of Feedstock and Pyrolysis Temperature

Biochar is sourced from a range of different sources, including agricultural and forestry wastes, manure, and municipal wastes [44,46,47]. The biopolymer, polysaccharide, and inorganics content and microstructure among these sources is known to differ greatly. Thus, studies on the performance of biochar in a particular application are often not equivalent and may not apply when different feedstocks are used. Some studies have attempted to isolate the impacts of lignin, cellulose and hemicellulose or naturally occurring inorganics (ash) on biochar yield, textural and chemical properties with mixed results [48–54]. The problem is that even among biomass types, for instance grasses or wood, there can be tremendous variation in compositional parameters which affect the biochar product. Additionally, genetic variation within a particular species can also result in variable biomass composition, as can soil chemistry and water and nutrient availability [53,55]. Pretreatments such as acid demineralization, alkali treatments, and steam activation have been used to work around these challenges [44,56]. However, those processes add to the energy and carbon footprints of biochar, for which two of the most attractive attributes are the simplicity in processing and the potential for development of carbon-negative functional materials [45,46]. More work is needed to investigate what can be achieved by streamlining the careful selection of biomass with very specific compositional parameters.

The temperature and rate of heating impact the formation of structure in biochars as well. Biochar can be formed by two primary types of pyrolysis: fast and slow. Fast pyrolysis is characterized by very high heating rate (> 300°C/min.) to intermediate temperatures (< 600°C), while slow pyrolysis is characterized by a much slower heating rate (5-10°C/min.) and higher final temperatures (600°C to 800°C). With slower heating comes longer vapor residence time, thus enabling secondary reactions between vapor phase and solid phase. While char yield is typically higher in slow pyrolysis, a faster heating rate enhances the removal of gaseous species, and typically produces more porosity.

HTT has a direct relationship with aromaticity of biochars. It is worthwhile to review the general trends in structure for biomass pyrolysis from room temperature up to >700°C. Keiluweit, *et al*. presented a model that has largely been accepted by others which illustrates these trends very well [46]. With initial heating of biomass beyond 150°C, dehydration and depolymerization reactions begin, initially in hemicellulose, with -OH groups leaving as water. Above 200°C depolymerization of lignin and cellulose begin and typically continue up to 300°C. In this temperature range, Transition Char is formed with the onset of aromatic ring formation begins, and significant ketone, aldehyde, and carboxyl -CO groups are observed due to dehydration and decomposition of lignin and cellulose. Between 300 – 700°C, Amorphous Char forms. Condensation of aromatic rings begins in this stage and the amount of pyranones, quinones, and furans increases. Volatile matter, tar-like light hydrocarbons and PAH's, decreases as does the content of heteroatom species, including oxygen and nitrogen. Above 700°C, the degree of ordering in aromatic phases increases drastically. The formation of turbostratic stacking of aromatic clusters has been observed by X-ray absorption near-edge fine-edge spectroscopy [46]

1.4. Bonding and Structure in Non-graphitizing Carbons

Carbon chemistry plays a definitive role in the structure of biochar. In pyrolysis, feedstock hydrocarbon structures undergo thermochemical conversion processes like dehydration, decarboxylation, and condensation. The resulting carbonaceous skeleton can be much different from that of the original cellulosic chain or lignin structures. Bone char consists of a carbonaceous phase of pyrolyzed collagen in addition to the biogenic apatite inorganic phase, therefore the impacts of carbon structure pertain to bone chars as well.

Carbon has the unique capacity to form extended networks of covalent bonds with other carbon atoms as well as with oxygen, nitrogen, sulfur and hydrogen, forming the building blocks of living matter, including biomass. Carbon has six electrons, two in the 1s orbital, two in the 2s orbital, and two in the 2p orbital. The four outer 2s and 2p electrons form different types of hybridized orbitals in bonding, known as sp^1, sp^2 and sp^3 hybridized bonds, based on the electron configuration of the atoms with which they form covalent bonds. This is the reason for the vast diversity of carbonaceous materials on the planet. Sp^3 hybridization results in four equivalent sigma bonding electrons which organize themselves in a tetrahedral structure at 109° from each other. Saturated hydrocarbons, for instance methane, and diamond all have sp^3 hybridization. For sp^2 hybridization, three equivalent sigma bonding orbitals are formed from the two 2s electrons and one of the 2p electrons in a trigonal planar configuration, spaced 120° apart, with the remaining 2p electron remaining in a delocalized π-orbital oriented perpendicular to the plane of the others. Graphite, graphene, and linear chains such as trans-polyacetylene exhibit this type of hybridization. Finally, sp^1 hybridization occurs when the 2s and 2p electrons form two hybridized orbitals, which orient at 180° from each other forming linear bonded structures, for instance C_2H_2, acetylene.

Carbon bonding is critical in understanding the development of structure in porous carbons. Rosalind Franklin did some of the earliest work characterizing the structure of pyrolytic carbons [57]. Her pioneering crystallographic studies formed the basis of understanding for graphitization at high temperatures, and she was the first to describe non-graphitizing carbons, a category to which biochar and activated carbon both belong. Non-graphitizing carbons tend to be mechanically robust and porous, with the micropores now known to derive from curvature and stacking misalignment of the fundamental aromatic clusters [58]. For graphitizing carbons, sufficient heat treatment times and temperatures (>2000°C) provided enough thermal energy for aromatic clusters within the material to re-order themselves into extended, stacked networks with long-range translational symmetry. For non-graphitizing carbons, even extended high temperature heat treatment would not produce this long-range order. Multiple models have been developed for the structure of primary aromatic clusters which would explain this behavior. Early models assumed that all of the carbon was formed of sp^2 hybridized bonds, with crosslinking that inhibited rearrangement of fundamental aromatic clusters even at high temperatures [57]. However, sp^2 crosslinking would not explain the impediment to re-organization. The model of Oberlin proposed that folded, extended, interconnecting networks of aromatic rings formed the basic structure, much like the staircases in a famous Escher print, and that this interconnectivity prevented graphitization [59]. Harris proposed that the presence of 5-, 6- and 7- membered rings resulted in warped, fullerene-like fundamental structures [60]. Other models have accounted for the presence of sp^3 hybridized carbon in non-graphitizing carbons, suggesting that it forms clusters of diamond-like carbon which occupy regions between sp^2 clusters, thus preventing graphitization [61]. Despite the diversity of these models, they all agree that the fundamental structural elements of non-graphitizing, pyrolytic carbons are clusters of aromatic rings similar to defected graphene particles [27,46,47,52,62–64]. In biochar, these structures are *not* microcrystalline graphite (or graphene), and do not show long-range order, being oriented randomly and containing planar defects as well as generally high levels of stacking defects, factors which challenge the formulation of a general model for biochar structure.[58,65] High levels of defects including holes, unpaired electrons, high hydrogen and heteroatom content, the presence of mineral phases and other forms of carbon including tar and coke complicate the definition of standardized, predictive model for biochar structure-function relations [46,52,57,66]. One notable biochar structural model accounts for the presence of 5-, 6- and 7- membered rings, vacancies, oxygen, hydrogen, and unpaired electrons [52].

In general, the size and stacking of aromatic condensates increases with heat treatment temperature (HTT) [20,46,47,65,67]. The size and stacking of condensates are sometimes collectively called order or aromaticity and will be referred to by both names in this paper. The ratio of sp^2 to sp^3 carbon also increases with HTT as hydrocarbons undergo thermochemical conversion into more thermally stable sp^2 hybridized structures [46,52,65]. The nature of pyrolysis processes, in which hydrogen- and oxygen-containing species volatilize and skeletal carbons condense into aromatic ring structures, are characterized by consistent decrease in the ratios of hydrogen and oxygen to carbon according to dehydration, demethylation, and decarboxylation reactions. The atomic ratios H/C (aromaticity index) and (O+N)/C (polarity index) for non-graphitizing aromatic carbons, first proposed by Van Krevelen in 1950 as metrics for comparing the order of different ranks of coal, have recently been proposed as predictive metrics for biochar adsorption performance because it has since been observed that biomass feedstocks and biochar show the same trends in aromaticity and polarity with increased HTT [46,47,68].

Pore formation is initiated during pyrolysis as volatiles escape the bulk, leaving voids (Figure 1). With further heating, skeletal carbon condenses into aromatic structures as oxygen and hydrogen bonds are broken during further volatilization. Open pores are formed when these gases escape efficiently from the bulk, exposing these spaces between aromatic layers to larger channels, known as mesopores. If the porosity is sufficiently open, adsorbates can enter micropores where dispersion forces are strongest, and remain for a longer period of time than molecules adsorbed on macropore surfaces. If volatiles are not able to exit the bulk material during pyrolysis, they can clog pathways out of the structure, resulting in “closed porosity”. Activation processes are designed to prevent or remove closed porosity in activated carbon and increase surface area available to adsorbates, but in biochar some level of closed porosity is expected to exist [27]. Surface area measurements in biochars can vary dramatically for this reason. Micropores are molecular scale cavities which form during pyrolytic volatilization and reorganization processes. They are found throughout the bulk solid as a sort of “negative molecular space”. It is convenient to think of micropores as branching off from mesopores, however micropores exist throughout the bulk and may not connect directly to mesopores. Diffusion through a microporous network is responsible for high uptake and fast adsorption kinetics [63].

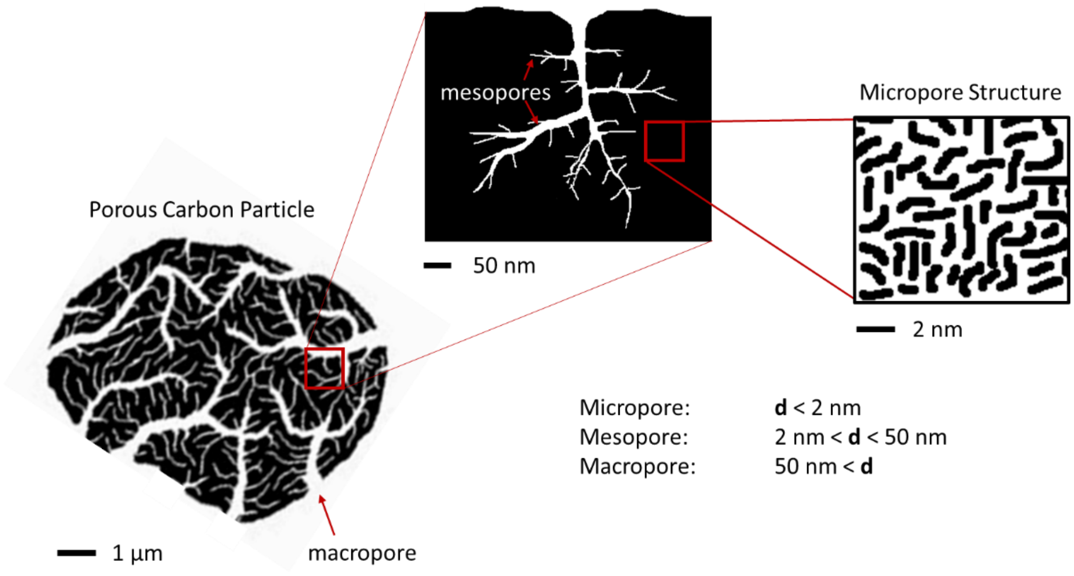

Figure 1: Schematic of the different scales and hierarchy for porosity in activated carbon. Note in the micropore structure diagram (right), black lines represent condensed aromatic regions similar to highly defected graphene. The white spaces in between represent microporosity. The structure of microporosity shown here is hypothetical, but is intended to illustrate that microporosity is associated with the misalignment of layers or stacked structures.

In addition to micropores (d < 2 nm), larger spaces known as mesopores (2 nm < d < 50 nm) and macropores (d > 50 nm) are present in biochar. While micropores can be considered as the spaces between randomly oriented aromatic layers, mesopores are largely considered to be larger spaces formed by diffusion of carbon atoms away from the pore center during thermally-induced reorganization processes.[27] Rehrmann, *et al.* pointed out that for smaller particles, the ratio of micro- and mesopores opening to the surface is greater than for larger particles, which, in part, accounts for faster diffusion observed in smaller particles.[69] Macropores opening to the surface of the particle are usually associated with the existence of plant cellular structures, visible in Figure 2.

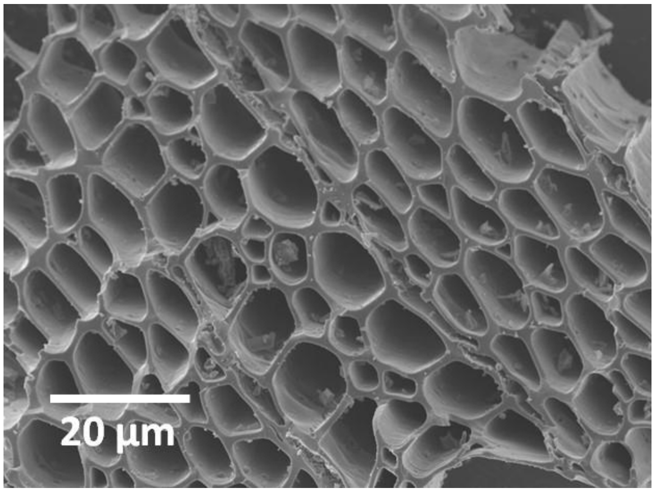

Figure 2: Biochar particle at 2000X magnification, pyrolyzed at 700°C. The natural cellular structure of the cottonwood feedstock is still apparent, however chemically biochar is much different from the precursor feedstock. Biochar can have a very high external surface area relative to microporosity, which might have proven to be important in ammonia dynamic adsorption.

1.5. Technical Background on Dynamic Adsorption

In the design of dynamic filtration systems, for instance in treating industrial gas purification or in respirator cartridges, it is critical to know the timeframe and range of toxin concentrations over which the adsorbent material provides protection. Breakthrough analysis is the means by which this can safely be determined. The breakthrough concentration, which can be selected as anywhere between 1% and 50% of the influent concentration, is defined as a pre-determined maximum allowable level of adsorbate in the water or gas stream, and the breakthrough time is the time at which this concentration is reached in the effluent stream [69,70].

In a dynamic adsorption, or breakthrough, experiment, adsorbate is carried into an isothermal packed adsorbent column via carrier gas at a constant concentration, C_0. The concentration of adsorbate at the outlet of the packed bed, C, is monitored continuously until the concentration reaches that of the inlet concentration (saturation). As adsorption begins at the inlet of the packed bed, the local bulk concentration decreases, and a concentration gradient, known as the mass transfer zone (MTZ), is established in the flow direction, Figure 3. The length and shape of the MTZ are determined by the mass transfer processes and experimental parameters like adsorbent particle size, flow rate and influent concentration. The shape of the breakthrough curve can provide valuable information regarding the diffusion processes occurring in the mass transfer zone [71,72]. The optimal case is long breakthrough time indicating high uptake capacity and steep concentration profile indicating low mass transfer resistance from bulk to particle to micropore.

Dynamic adsorption occurs by three fundamental processes: bulk diffusion of the adsorbate from the moving fluid to the particle surface, diffusion along the particle surface, micropore diffusion, and adsorption. In a dynamic adsorption experiment, the overall rate of adsorption is observed, with either mass transfer resistance in the bulk fluid or micropore diffusion being the rate limiting step. The rate of adsorption, particularly physisorption, is much faster than either diffusion process, and is not considered as the rate limiting step [69]. However chemisorption has been observed to impact the overall rate of adsorption in oxygenated activated carbons [73]. The relative impact of each fundamental process is determined by the characteristics of the packed bed, the flow rate, the chemistry of the target adsorbate and the size, microstructure, and chemistry of the particles themselves.

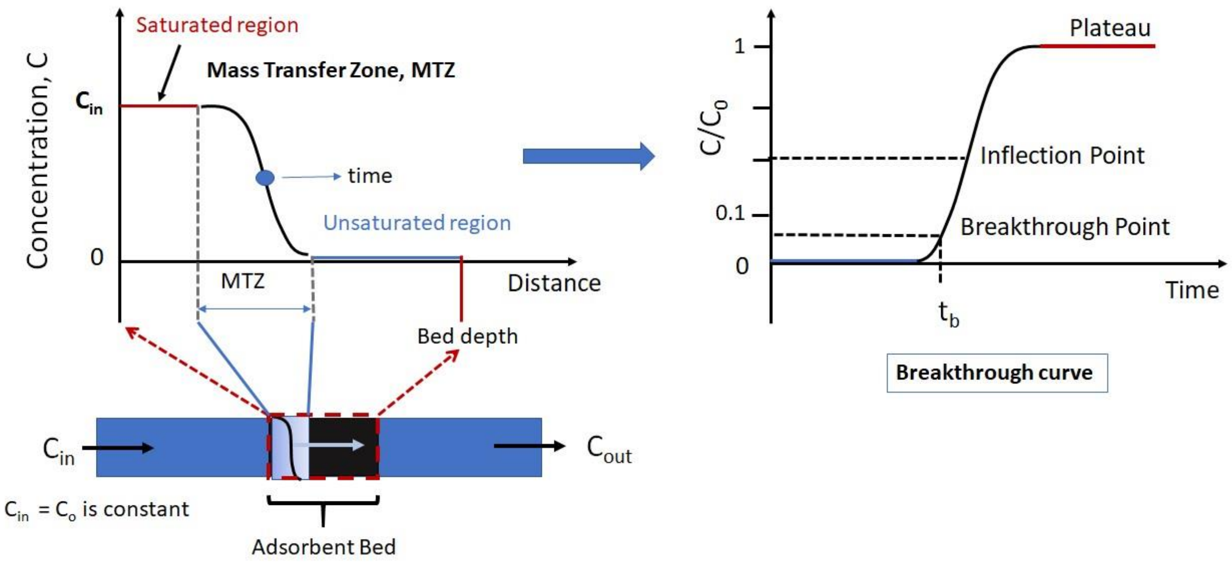

Figure 3: (left) Schematic of the packed bed and concentration gradient and (right) breakthrough curve for a typical breakthrough experiment. In the diagram at lower left, the superimposed MTZ does not imply any radial dependence of the concentration gradient, it is just shown to help the reader understand the axial dependence. In fact, the assumption of no radial dependence is made for breakthrough experiments. The shape of the breakthrough curve (right) reflects the shape of the MTZ moving though the bed over time.

Bulk diffusion across the fluid boundary layer is driven by the concentration gradient between the bulk fluid and the particle surface as adsorbate is taken up by adsorbent. Flux of adsorbate to the surface of the particle is proportional to the concentration gradient and therefore inversely proportional to the boundary layer thickness. In the case where a process is bulk diffusion limited, process control can be accomplished by altering the flow rate to alter the boundary layer thickness or changing the influent concentration to alter the driving force for diffusion. Decreasing flow rate or decreasing concentration both increase the breakthrough time (because these processes are first-order with respect to the concentration of contaminant up to concentrations relevant for breakthrough) while an increase in flow rate or concentration have the opposite effect.

As particle size decreases, the impacts of intraparticle diffusion and surface adsorption processes become increasingly important [70]. For particles smaller than ∼150 µm this is especially true, and the dependence on flow rate is drastically diminished [69]. Factors such as surface charge (related to oxygen content), adsorbate/pore size limitations (steric hindrance), ash content, pore structure, aromaticity, and surface chemistry may show individual or collective effects on breakthrough behavior.

1.6. Structure of Dissertation

The first primary focus of this dissertation was to investigate gaps in biochar source-structure-function relationships which will be critical to understand if biochar is to be used as a functional material of technical significance. Therefore, this study is largely focused on the characterization aspects of biochar, establishing more mature source-structure relationships. The second primary focus was to extend that relationship to the “function” aspect, in which the dynamic adsorption of ammonia by biochar was investigated. This research has contributed new insight to the broader field of biochar and bone char source-structure-function relations. I have also demonstrated that biochar has strong potential in dynamic adsorption of ammonia, thus validating its utility and laying a solid groundwork in this area.

In Chapter 2 of this dissertation, I show the impacts of lignin microstructure and potassium content on biochar structure and chemistry. Unique genetic variants of cottonwood, for which the biopolymer content and lignin microstructure were already well-characterized were used to isolate the impacts of lignin microstructure, and water-demineralization was used to alter potassium content. In this chapter, I present results of thermal gravimetry, mass spectrometry, ash analysis, Raman and IR spectroscopy and N_2 adsorption. These results show direct links between the content of specific lignin monomeric units and aromaticity of the resulting biochars.

Demineralization was linked to other important results indicate that demineralization increases the oxygen content of resulting biochars, and may result in more cross-linked sp^3 phases – important for mechanical stability and pore structure of biochars.

Chapter 3 describes the results of dynamic adsorption (breakthrough experiments) of 1% ammonia by biochar and a comparative activated carbon. These results are the first that I have seen for biochar in dynamic ammonia adsorption. Biochars showed breakthrough times nearly twice as long as for the high surface area activated carbon, indicating surface area alone does not determine breakthrough capacity. The small particle size selected for this study indicates that diffusion is limited by intra-particle processes, which are related to the structure and chemistry of the materials. Due to the presence of C=O functional groups observed with IR spectroscopy, chemisorption is suspected to play a large role in the high capacity and the diffusion limitations

In Chapter 4, I review relevant structural aspects of bone char formed from pyrolyzed bovine femur. Bone char literature has widely mis-characterized the structure of the mineral phase of bone char, and this work corrects that interpretation, providing a sound foundation for understanding the high uptake capacity of heavy metals by bone char observed by others [40]. In this work I also provide new insight into the structure and chemistry of the carbonaceous phase of bone char. This result supports the hypothesis that the carbonaceous phase is involved in heavy metals adsorption, and not just the mineral phase as is typically assumed, which may have strong implications for removal of Cu^{2+}.

Supplemental figures and data for each chapter are presented in the Appendices. Appendix A is the supplemental information to accompany Chapter 2, Appendix B is the supplemental information to accompany Chapter 3, and Appendix C is the supplemental information to accompany Chapter 4. Other supporting information and methods which have not been, and will not be submitted for publication are presented in additional appendices beyond Appendix C.

Chapter 4 is currently under revision for publication. It has been recommended for publication after revision. Chapter 3 has been submitted for publication. Chapter 2 is in preparation for publication, and is expected to be submitted within the next few weeks. Each of these chapters is intended as a stand-alone publication, therefore there is some repetition of introductory material which is pertinent to char structure and dynamic adsorption. It is expected that there may be some minor modifications to each before final publication.

Overview of Author's Contributions

Chapter 2 is a characterization study of the impacts of lignin S/G and potassium on biochar structure and chemistry. The author performed all characterization experiments except N_2 adsorption and ICP-OES and processed/analyzed all data except S_{BET} and pore volume.

Chapter 3 is a study of the dynamic adsorption of 1% ammonia by biochar and activated carbon. The author conducted dynamic adsorption experiments and analyzed data. The author also took Raman and DRIFTS measurements.

Chapter 4 is a characterization study of bone char. The author conducted all characterization except XRD and N_2 adsorption/desorption.

The author wrote chapters 2-4 and participated in editing chapters 2-4 with co-authors.

2. Significance of Lignin S/G and Potassium in Formation of Biochar Structure and Chemistry[1]

2.1. Introduction

Biochar is the carbonaceous, solid product of heating biomass in an oxygen-limited environment above 250°C, usually sourced from inexpensive, locally available agricultural and forestry wastes which can otherwise be difficult and expensive to dispose of [43]. Interest in biochar has received a boost in the last couple of decades toward more technical applications because it has been identified as a carbon sequestration resource with far-reaching global impacts [41,43,45,46,74,75]. It is thus very attractive as a carbon negative, economical, high performing functional material and as feedstock for more advanced materials processing [44]. Biochar possesses attractive functional properties like high specific surface area, high micropore volume, and tunable surface chemistry. Its strong potential as an adsorbent for separation technologies and environmental remediation has been demonstrated [28,29,32,44,67,74,76–79]. Because it can be produced at lower temperatures than activated carbon (< 900°C) using little to no additional physical or chemical activation, biochar is attractive from the perspective of minimizing the cost, energy input and carbon footprints associated with the development of high-performing functional materials in a range of applications. Therefore, gaining a firm understanding of biochar properties that can be optimized through the use of feedstock selection and minimal processing is increasingly important.

The properties of pyrolytic carbons, a category to which biochar and activated carbon belong, strongly depend on the highest heat treatment temperature, activation, and feedstock

---

[1] Muretta, J.E., Uriarte, J., Compton, D., Stadie, N.P., Prieto-Centurion, D., LaDouceur, R., Kirtley, J.D. Significance of Lignin S/G and Potassium in Formation of Biochar Structure and Chemistry. *Manuscript in Progress*.

[27,46,47,80]. Without activation, broad diversity in feedstock composition has been observed to challenge the development of predictive models for biochar yield, structure, and surface chemistry based on biomass source. From one type to another there is natural variation in important properties like cellulose to lignin ratio (C/L), lignin composition, ash content, and ash composition [46,52,81–85]. While some recent studies consider trends associated with biomass type (herbaceous plants, grasses, hardwoods, and softwoods) important properties are known to vary even within sources of the same type based on genetic variation, what part of the plant is used, soil type, and growing conditions [46,54,86]. Identification of specific, measurable feedstock parameters which drive the formation of desirable physical or chemical characteristics of biochar would help streamline future biochar research and design.

Despite these challenges, some important guidelines have been established toward this goal, with lignin and potassium showing some synergy in determining char yield and surface area [48–52,87–89]. A number of studies have attempted to address the impact of lignin and potassium on specific surface area, pore volume, pore size distribution, aromaticity and surface chemistry of resulting chars with some success [52,53,85,89–91]. However, in selecting biomass precursors by which to test these impacts, it is challenging to find comparative materials with different lignin microstructure or potassium content while minimizing variation in other impactful feedstock parameters, and therefore results may not be comparable.

Among woody biomass used for bioenergy technologies, *Populus trichocarpa* (cottonwood) is attractive for its rapid growth habit and tolerance of a range of soil and climate conditions [81]. Genetic variation among *P. trichocarpa* has been found to cause predictable differences in lignin molecular structure which reduce biomass recalcitrance to microbial digestion in carbohydrate extraction [81,82,86]. It is proposed in this present study that use of *P.*

trichocarpa genetic variants as model feedstock for biochar production allows a means of investigating the role of lignin molecular structure in determining biochar yield, structure and surface chemistry.

In this work, the objectives were to investigate the impacts of naturally occurring potassium and lignin microstructure on porosity, aromaticity, and surface chemistry of resulting biochars formed by pyrolysis to 700°C. Lignin microstructure was altered using two genetic variants of *P. trichocarpa* known to have similar C/H/L content but very different ratio of lignin syringyl (S) and guaiacyl (G) monomeric building blocks [86]. DI water leaching of biomass, much less destructive on native plant macromolecular structure than acid leaching, was used to control the potassium content. Assessment of yield, specific surface area, pore volume, surface functional groups, sp^2 and sp^3 hybridized carbon phases, H/C, and proximate and ultimate analysis were used to assess the impacts of these feedstock parameters on char formation at 700°C.

2.1.1. Importance of Lignin Macro-molecular Structure

Lignocellulosic biomass, sourced from herbaceous and woody plants and agricultural waste, is composed of the polysaccharides like cellulose and hemicellulose, lignin, inorganic plant nutrients (ash), trace amounts of other organic substances (proteins and lipids), soil particles, and water. Lignin is present as the second most abundant component (10 – 30%) after cellulose, serving as the “glue” which holds the stiff, structural cellulose microfibrils together much like the epoxy matrix in a carbon fiber composite, also promoting hydrophobicity and offering protection from microbial attack due to its highly aromatic structure [84,92]. Lignin has been observed to form the most char by weight (up to 50% yield by weight), followed by cellulose and hemicellulose [93]. The larger macromolecular structure in lignin is composed of cross-linked phenylpropane monomeric subunits of three primary types, syringyl, guaiacyl, and hydroxyphenyl (H), each having hydroxyl, carboxylic, and methoxy functional groups. These groups are distinguished by the number of methoxy groups – syringyl units have two, guaiacyl units have one, and hydroxyphenyl units have none (Figure 4) [54]. Relative quantities of S and G units and their characteristic interunit crosslink types, which can be ether bonds or C-C bonds, vary between biomass types and even among different genetic variants of the same species [81,86]. For instance, hardwoods are known to have greater percentages of S-units than softwoods, which contain mostly G-units.

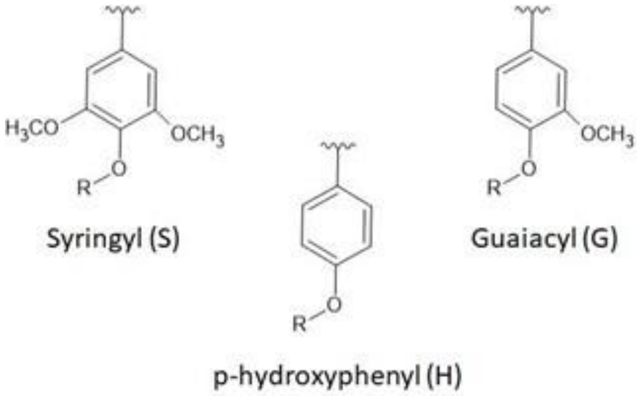

Figure 4: Basic structure of syringyl, guaiacyl, and hydroxyphenyl groups which form the backbone of the lignin macromolecular structure. The difference in methoxy group content is the defining feature of these groups, and has implications in char formation.

The impact of lignin S and G in pyrolytic products formation has been reported in relation to the role methoxy functional groups in forming reaction intermediates [54,90,94,95]. Hosoya, *et al*. proposed that methoxy groups on S and G units are critical for char formation as the methoxy moiety is key in the formation of the critical char intermediate o-quinonemethide [96]. In pyrolysis experiments using sealed ampule reactors containing either syringol and guaiacol, derivatives of S and G units, Asmadi, *et al.* observed differences in reactivity and early stage coke production (both being higher for syringol) which were attributed to the additional methoxy group on syringol [95]. It is possible that the formation of early stage coke in S-rich feedstocks is likely to impact the aromaticity and surface chemistry of resulting chars since coke could become trapped in primary biochar, contributing to yield of more thermally stable and more aromatic char [95,97]. Attempts have been made to understand whether these effects scale for complete biomass [54], however because of the challenges in finding otherwise compositionally similar biomass, results cannot conclusive be linked to lignin S and G.

2.1.2. Potassium as a Catalyst in Char Formation

Ash content and composition also vary widely between biomass types, with herbaceous types, like hemp, and grassy types, like switchgrass, having higher ash content than woody types. Compositional variation in ash occurs between biomass types as well, and even within the same biomass type depending on soil composition, water availability, seasonality, and nutrient availability. Ash is composed primarily of silica, alkali and alkali earth metals and transition metal oxides [92]. Potassium and other alkali and alkali earth metals species (AAEM) are present in biomass in salt or oxide form, integrated into plant cellular structures as essential plant nutrients as well as in soil particles and dust [98].

Potassium levels can vary greatly between biomass types, and previous studies of the effects of potassium have relied on acid demineralization followed by impregnation with potassium salts, a process which is known to have a deleterious impact on other biomass component structures, including lignin [49,52,90,92]. HCl- leaching in particular has been found to catalyze cleavage of the methoxy group on S and G lignin units, making the impacts of these groups on char formation more difficult to quantify with that method [90]. Water leaching, on the other hand, has been observed to preferentially remove a large percentage of naturally occurring potassium without the associated structural degradation [49,54,92,99].

Pyrolysis is a technique for extracting important liquid and gas phase products from biomass which are used in energy production, thus factors which result in optimization of desired products yield have been well-studied [76]. In those studies, the goal is often to minimize biochar formation in favor of more valuable bioenergy products, thus biochar yield is usually reported as it impacts the formation of gaseous and liquid products [48,50,51,54]. During pyrolysis of woody biomass, potassium has been observed to catalyze condensation reactions which are critical to char formation, resulting in higher production of gaseous and solid products over liquid and volatile products [49]. Because of this function, removal of potassium either by acid or water washing reduces biochar yield, typically in favor of the formation of liquid products and certain volatile species [49–52,54,62]. Potassium is known to catalyze gasification of biochar at high temperatures in the presence of CO_2 and H_2O, which may counter its role as a catalyst for condensation reactions, although the extent to which this happens is not well-characterized [49,56,100]. For woody biomass, demineralization has been found to enhance surface area, pore volume (consistent with its role in gasification) , and increase oxygen content in high temperature biochars, but results appear to depend on the relative content of cellulose, hemicellulose and lignin [48,49,52]. The picture is emerging that the synergistic impact of potassium and lignin S/G is not trivial in biochar formation. While the impacts of other biomass components in those previous studies cannot be ruled out, we propose that by utilizing *P. trichocarpa* genetic variants the impacts of other component structures can be held constant, allowing a more pointed investigation of the impacts of potassium and S/G only.

2.1.3. Temperature Effects

The effects of pyrolysis HTT on textural and chemical properties of biochars is well-documented. Specific surface area and pore volume generally increase with temperature up to ~700°C, and then decline with temperature above ~900°C as the degree of carbonization reaches a maximum [76]. Surface chemistry is another fundamental property which impacts adsorption behavior. In biochars, the degree of aromaticity increases and oxygen- and hydrogen- content decrease monotonically with temperature [46,47,101]. For the present study, HTT within the range which was likely to maximize surface area and porosity while achieving non-negligible oxygen and hydrogen content was selected. All biochars used in this study were prepared at 700°C.

2.2. Materials and Methods

2.2.1. Materials Preparation

In this present work, two genetic variants of *P. trichocarpa* which were previously used as feedstocks in carbohydrate extraction studies were used as biochar feedstock in order to take advantage of the detailed lignin characterization and constant composition of other biomass components [86]. Lignin in the two variants selected for this biochar study have been previously characterized by Yoo and Ragauskas, *et al.* according to the methods in reference [86]. Those lignins were found to have very different S/G, but similar biopolymer content (cellulose, hemicellulose, lignin), offering an opportunity to study the effects of S/G on char formation and functional properties. Biopolymer content and lignin S/G are reported in Table I.

Table I: Biopolymer characteristics and lignin S/G of *P. trichocarpa* variants

	Glucan (cellulose)[**]	**Xylan (hemicellulose)**[**]	**Lignin**[**]	**Lignin S/G**
BESC-316	44.1%	18.8%	23.3%	1.67
CHWH-27	49.2%	17.5%	19.4%	3.88

[**] Courtesy of Yoo and Ragauskas, *et al.*

As-received BESC-316 and CHWH-27 were ground and sieved to -8+16 mesh (1.2 – 2.4 mm). Untreated, sieved biomass is labelled as BESC-316 and CHWH-27 from here on. A portion of each sieved, untreated biomass was subjected to demineralization by placing ~10 g of biomass in 1L Nalgene bottle with 1L Type I water for 40 hrs. at room temperature. Samples were drained, air dried at room temperature for 24 hours, and then dried at 70°C in air prior to bagging and storage under ambient conditions. Demineralized biomass is labelled as L-BESC-316 and L-CHWH-27.

Biochar was prepared from untreated and treated materials by pyrolysis at ~15°C/min. to 700°C (5 min. dwell) in a tube furnace (MTI, OTF-1200X) with 60 mm x 60 cm quartz tube under flowing argon (3.0 L/min.). Cooling occurred in the tube furnace under flowing Ar at a rate of ~5°C/min. Biochars are named BC-B and BC-C for those made of untreated biomass, with the B and C denoting BESC-316 and CHWH-27 feedstocks, respectively. Demineralized biochars are labelled as BC-BL40 and BC-CL40 according to the same scheme.

2.2.2. Characterization Methods

Ultimate analysis of all biomass materials was conducted according to ASTM E871, ASTM D1102, CEN/EN 15104 and CEN/EN 15289 to quantify differences in moisture, ash content and biomass elemental composition related to genetic variation and demineralization. Error is quantified according to the method.

Biomass ash was produced through combustion according to NREL/TP-510-42622. Ash composition was quantified by inductively coupled plasma optical emission spectroscopy (ICP-OES) according to EPA Method 200.7. Ash from each biomass was sampled in triplicate. Mean values for Ca, K, Mg, and Na content are reported with standard deviation.

Volatile and recalcitrant carbon were measured using thermal gravimetric analysis (TGA) (TA Instruments, Inc.) adopting the designation for volatile carbon used by Mitchell, *et al.* [102]. Samples were heated in dry argon using Pt TGA pans, heating at 2°C/min. to 900 °C. Volatile carbon was measured as the mass lost at 450 °C minus moisture. The remaining mass represented recalcitrant carbon plus ash. Moisture and ash were measured by heating in dry UHP Ar or 90% UHP O_2/balance UHP Ar at 2°C/min. to 800 °C. Moisture was calculated as the mass lost after holding at 120 °C for 60 minutes. Ash content was measured as the mass remaining after combustion in 90% UHP O_2/balance UHP Ar at 2°C/min to 600 °C.

Thermal decomposition products were measured during TGA runs in oxygen and inert gases with a Pfeiffer ThermoStar electron impact quadrupole mass spectrometer (MS). Mass to charge ratio, m/z, of 2, 18, 28 and 44, corresponding to singly ionized H_2, H_2O, CO, and CO_2 were tracked as well as some characteristic hydrocarbon fragments. Water and CO_2 from combustion were used to calculate hydrogen to carbon atomic ratio (H/C). Products distribution from TGA runs in argon were used to study functional groups and thermal decomposition behaviors.

H/C was calibrated using a coupled TGA and MS to calibrate the area of H_2O and CO_2 ion current peaks based on the thermal decomposition of a reference material, calcium oxalate monohydrate, in 90% UHP O_2/balance UHP Ar. A similar procedure has been reported by others [103,104]. Briefly, calcium oxalate monohydrate decomposes in distinct steps, with the first step representing approximately 12% mass due to loss of water and the third decomposition step, representing approximately 29% mass loss which is due purely to CO_2. By using three different masses of calcium oxalate monohydrate, a linear relation between mass and ion current for water and CO_2 was determined. Mass loss profiles and calibration curves are shown in Appendix A.

Functional groups associated with surface chemistry were investigated using Diffuse Reflectance Infrared Fourier Transform Spectroscopy (DRIFTS). All measurements were taken under ambient conditions with a Shimadzu IR Tracer100 with Harrick Praying Mantis DRIFTS attachment and liquid N_2 cooled mercury-cadmium-telluride detector with atmospheric correction applied. Samples were prepared for DRIFTS by grinding individual powdered samples (~7% wt./wt.) in KBr powder using a mortar and pestle. A reference spectrum collected from pure KBr were used for background subtraction. Spectra were collected in the 4000 – 400 cm^{-1} range at 2 cm^{-1} resolution with 120 accumulations. At least three spectra from each material were collected to test for uniformity. Raw absorbance spectra with background subtraction were normalized to the aromatic C-C stretch at 1585 cm^{-1}. Second derivatives of each raw spectrum were mathematically calculated using OriginPro software (OriginLab, Corp.).

Raman scattering measurements were taken using a Renishaw Raman spectrometer. Measurements were taken for undiluted materials using a 20x LWD objective using a 457 nm emission line from an argon ion laser at 30 μW power and 1 – 5 μm spot size. Scans were taken between 500 – 2300 cm^{-1} with 3-5 second accumulation time and 5 – 20 repetitions in order to achieve sufficient signal/noise at very low laser power. For each material, 3 – 5 randomly chosen particles were analyzed as a check for material homogeneity.

Nitrogen adsorption/desorption isotherms were measured at 77 K between 10-4 and 100 kPa using an automated Micromeritics 3Flex volumetric instrument. The samples were degassed at 130°C under oil-free vacuum to 10-9 kPa for 4 hours prior to measurements. Specific surface area was calculated by the Brunauer-Emmett-Teller (BET) method between the lowest partial pressure and the maximum in the Rouquerol plot [63]. Total pore volume was calculated by the single-point method at $P/P_0 = 0.95$ [105].

2.3. Results and Discussion

2.3.1. Ultimate Analysis of Biomass Feedstock

Ultimate analysis of untreated and demineralized biomass (Table II) showed that BESC-316 and CHWH-27 were chemically quite similar in terms of moisture, C, H, N, O, and S. CHWH-27 contained 0.09% (by wt.) more ash, however upon demineralization ash content for L-BESC-316 and L-CHWH-27 was identical. A reduction in N-content with demineralization indicates that N-rich component structures such as proteins were more water soluble, and were lost during the leaching process.

Table II: Ultimate analysis of biomass feedstock (% wt.)

	BESC-316		**L-BESC-316**	
	As-received	**Dry Basis**	**As-received**	**Dry Basis**
Total Moisture	3.90		2.72	
Ash	0.45	0.46	0.21	0.21
Carbon	46.94	48.84	47.77	49.11
Hydrogen	5.60	5.83	5.82	5.99
Nitrogen	0.25	0.26	0.20	0.21
Oxygen	42.87	44.61	43.27	44.84
Sulfur	<0.01	<0.01	<0.01	<0.01
	CHWH-27		**L-CHWH-27**	
	As-received	**Dry Basis**	**As-received**	**Dry Basis**
Total Moisture	3.67		2.14	
Ash	0.54	0.57	0.20	0.21
Carbon	46.62	48.39	47.47	48.51
Hydrogen	5.50	5.71	5.65	5.77
Nitrogen	0.22	0.22	0.16	0.16
Oxygen	43.44	45.10	44.37	45.34
Sulfur	<0.01	<0.01	<0.01	<0.01

2.3.2. Biomass Ash Compositional Analysis

AAEM content of ash formed by combustion of biomass samples is reported in Table III. Ash from BESC-316 and CHWH-27 contained minor, but statistically significant variation in AAEM composition. BESC-316 ash had a significantly lower levels of potassium and magnesium compared to CHWH-27, with no statistical difference in calcium and sodium levels. Water leaching removed most of K and Na from both BESC-316 and CHWH-27, but was less effective at removing Ca and Mg. Statistically different levels of Ca and K were present in L-BESC-316 compared to L-CHWH-27, but no difference is observed for Mg and Na. Depletion of potassium in demineralized materials offers the opportunity to observe the impacts of S/G on biochar properties without influence from potassium catalytic action.

Table III: AAEM composition of dry biomass quantified by ICP-OES of digested ash, mean of three samples with ± one standard deviation reported

	AAEM species concentration, ppm			
	Ca	**K**	**Mg**	**Na**
BESC-316	645 ± 74	580 ± 61	197 ± 21	12 ± 1
L-BESC-316	502 ± 40	63 ± 6	139 ± 12	1 ± 0
CHWH-27	648 ± 65	1004 ± 87	217 ± 20	11 ± 2
L-CHWH-27	393 ± 39	83 ± 8	119 ± 13	1 ± 0

2.3.3. Biochar Yield

The yield of solid biochar from each material is reported in Table IV. Results agree with the those discussed in Section 2.1.2. In the presence of naturally-occurring ash, the difference in S/G for BESC-316 and CHWH-27 did not result in a significant variation in biochar yield. Demineralized biomass produced less char than untreated biomass, as predicted, with the impact of demineralization being stronger for L-CHWH-27 than for L-BESC-316.

Table IV: Biochar yield ± variance and other properties

	Mean Yield, %	H/C	Moisture (% wt.)	Ash (% wt.)	H (% wt.)	C (% wt.)	O+N** (% wt.)
BC-B	20.35 ± 0.35	0.40	0.98	1.91	1.84	54.61	40.39
BC-BL40	18.50 ± 0.65	0.41	0.83	1.02	1.89	54.85	41.63
BC-C	20.43 ± 0.08	0.37	1.03	2.44	1.68	53.24	41.19
BC-CL40	17.74 ± 0.17	0.47	0.77	0.94	1.98	50.10	46.37

** by difference

As noted in Section 2.1.1, it is challenging to isolate the effects of lignin microstructure in biochar formed from whole biomass. Previous studies indicating synergy between potassium and lignin did not consider lignin microstructure and S/G is usually not reported. In other studies where lignin microstructure was investigated, compositional variation in other biopolymer components, for example cellulose and hemicellulose, challenge any conclusions based solely on S/G [54]. Differences in reactor configuration, i.e. closed ampule vs. flowing inert gas, can also skew the distribution of products as in reference [54].

In this present study, statistically different yields reported for demineralized samples are attributed to the impact of S/G on char formation, with lower S/G resulting in higher char yield. Asmadi and Kwamoto, *et al.* linked a similar observation to the function of the additional methoxy group on S-units [95]. Those authors found that when pure syringol and guaiacol were pyrolyzed in closed ampule reactors to 600°C, major differences in products distribution over time were attributed to the role of the methoxy group. Syringol produced more coke at earlier times compared to guaiacol due to the presence of two methoxy groups compared to one on guaiacol. While a small fraction of coke is likely converted to char at higher temperatures under those conditions, Asmadi proposes that much of it is converted to gaseous species by gasification reactions in the presence of effusing water, CH_4 and CO_2, effectively reducing solid products yield. This agrees with the difference in yield observed for BC-BL40 and BC-CL40, where the higher S/G material produced lower char yield with reduced AAEM content. In a flowing gas reactor, the enhanced formation of gaseous species would likely reduce yield and enhance microporosity as volatiles are carried out of the deeper char structure by gaseous species, thus enhancing interconnected pores [27].

With respect to potassium content, untreated biomass samples contained comparable levels of naturally occurring Ca, Na, and Mg, however naturally occurring potassium was present at nearly twice the level in CHWH-27 compared to BESC-316. It is proposed that based on the similarity of biochar yield for BC-B and BC-C, the impacts of high S/G and high K-content may have opposing impacts on char yield. Further, when potassium content is diminished by washing, reduced yield for the higher S/G sample would be expected based on the discussion above for BC-BL40 and BC-CL40, and this result was indeed observed. From this, it is proposed here that char yield correlates negatively with S/G, which is countered by the positive correlation with K-content.

2.3.4. Thermal Analysis of Biochars

2.3.4.1. Combustion Analysis

Thermal gravimetric studies in oxygen (Figure 5) and inert environment (Figure 6) provided further insight into the composition and structure of the biochars as these properties relate to S/G and K. In its simplest application, combustion TGA provided quantification of moisture, organic, and inorganic components of the biochars. Ash and moisture content are listed in Table IV. Demineralization reduced the ash content of the biochars by approximately half, reflecting the trend observed for whole biomass (Table II). Moisture content of all biochars was < 1.1 wt. %.

The DTG signals associated with combustion TGA indicate differences in peak combustion temperature and rate based on K-content. Peak temperatures and rates of combustion are listed in Table V. Demineralization generally had the effect of increasing the peak temperature and reducing the peak rate. The behavior of the peak combustion temperature was consistent with the role of potassium in catalyzing oxidation reactions [49,51,100,106]. The similarity in temperature and rate of maximum combustion for the two demineralized biochars indicates S/G does not play a deterministic role in the rate and temperature of combustion reactions for these chars.

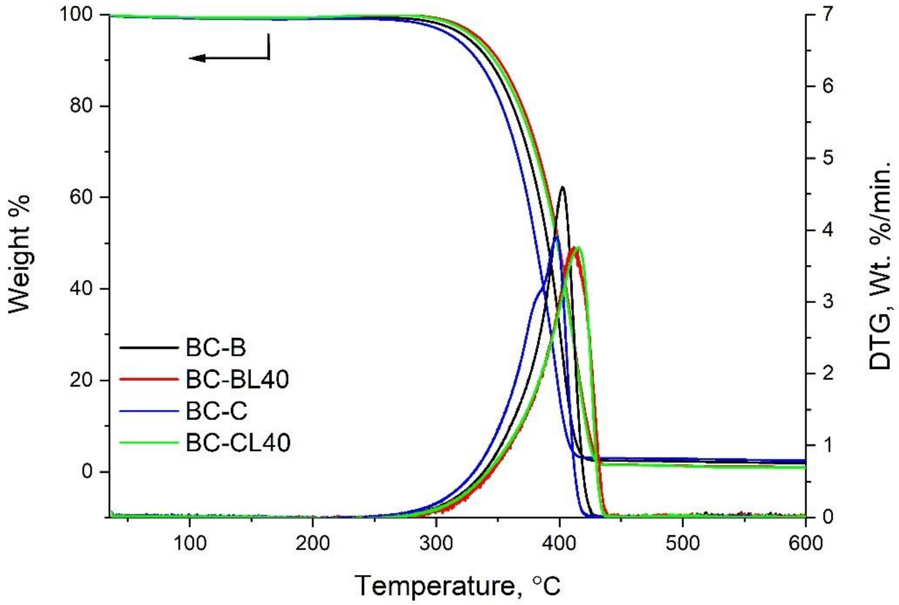

Figure 5: Combustion TGA and DTG results indicate differences in reactivity between untreated and demineralized biochars. Demineralization increases the activation energy needed for peak combustion.

Table V: Summary of combustion and thermal decomposition analysis by TGA

	Combustion in 90% O_2		**Thermal Decomposition in Ar**	
	Max. Temp., °C	**Max. Rate, wt%/min.**	**Volatile Carbon, wt%**	**Recalcitrant Carbon, wt%**
BC-B	402	4.6	4.1	93.0
BC-BL40	413	3.8	3.9	94.3
BC-C	383, 398	3.2, 3.9	3.9	92.6
BC-CL40	415	3.8	4.5	93.8

2.3.4.2. Thermal Decomposition in Argon

Thermal gravimetry of all biochars in argon allowed for the determination of volatile vs recalcitrant carbon, and when coupled with mass spectroscopy, identification of gaseous products linked directly to thermal decomposition of functional groups based on the temperature range over which they are observed. From this, a better understanding of functional group chemistry as well as the hybridization of carbon structures which they are associated with was achieved. During biochar thermal decomposition, oxygen effuses as water vapor (from -OH groups), CO_2 (from carboxylic anhydrides, lactones, and pyrone groups) and to a lesser extent CO (from anhydrides and ether groups), and hydrogen effuses as H and H_2. In this present work, H_2O, CO_2, CO, and H_2 effusion during heating in a TGA were tracked using a quadrupole mass spectrometer, and they were found to be the primary effusing species. The effusion profiles for these species are shown in Figure 7. Assignment of functional group origins for these species was made according to references [107] and compared against the presence of vibrational modes for those groups in the DRIFTS spectra in Section 2.3.5. Some significant differences in quantity of effusing species and, in the case of hydrogen, the temperature range, was observed which are likely to be tied to deterministic role of potassium and S/G on the development of structure and surface chemistry in biochars. There is also the possibility of catalytic action of potassium on both thermal decomposition and gasification processes in biochar. Because the extent and equilibrium of gasification reactions is linked directly to the formation of gaseous species from existing surface functional groups by thermochemical conversion, the extent of any impacts from gasification could not be directly measured by TGA-MS, thus is largely neglected in the following discussion.

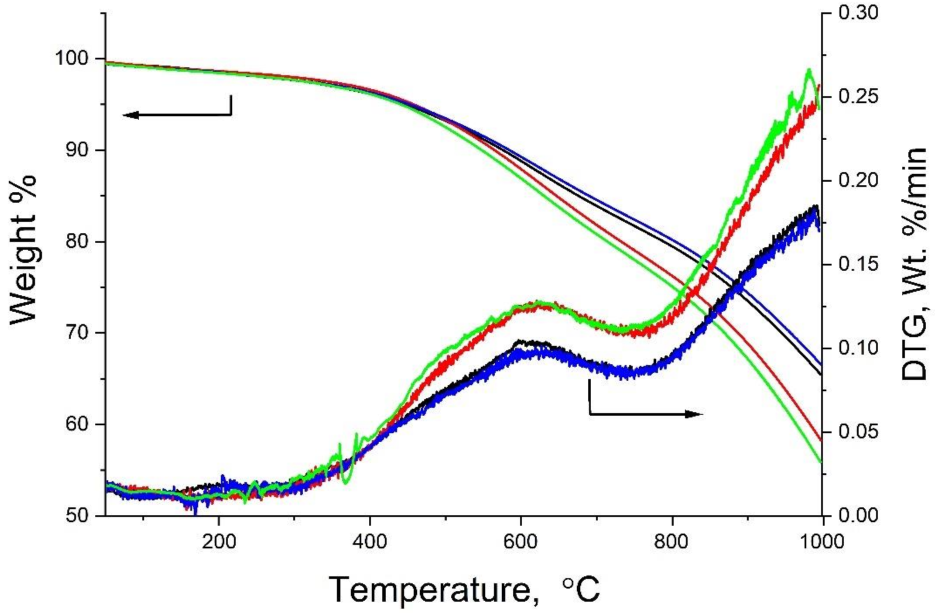

Figure 6: Thermal decomposition TGA and DTG for biochars in inert environment. Demineralized biochars show more weight loss up to 1000°C compared to untreated biochars. This activity is attributed to a higher content of oxygenated functional groups in demineralized chars.

Biochars can contain some labile species, that is, those which are not covalently bonded to the carbonaceous skeleton but are physisorbed on the surface or in pores, and these are collectively known as volatile carbon. The bulk of the carbonaceous skeleton as well as covalently bonded functional groups have higher thermal stability and are collectively referred to as fixed or recalcitrant carbon. Heating to moderate temperatures gives labile species sufficient energy to effuse out of the biochar, but more thermally stable structures remain intact. Volatile carbon and recalcitrant carbon are reported in Table V. All biochars showed very little mass loss up to 450 °C, consistent with the expected low volatiles and polyaromatic hydrocarbon content of biochar prepared at >500 °C [66]. The volatiles content of untreated biochars was not significantly higher than that of demineralized biochars, indicating volatiles clogging pores is not responsible for the low surface areas reported for untreated biochars in Table VII.

As temperature was increased beyond 450 °C, all biochars underwent thermochemical conversion, i.e. carbonization reactions. Multiple mass loss regimes are observed above 450 °C in the DTG signals in Figure 6,7, indicative of carbonization and reorganization processes in different biochar component structures, for instance oxygen-containing functional groups on low-density polymeric structures are likely to begin to degrade at lower temperatures than those associated with aromatic structures, and condensation of aromatic rings is likely to occur at very high temperatures. When coupled with the rate of mass loss from the DTG signal, the evolution of gaseous species within these regimes provides an overall picture of carbonization behavior, as well as clues to the functional group chemistry and carbon-carbon bonding within those structures. The following discussion of gaseous species effusion is based on observations from Figure 7.

2.3.4.3. Effusion of Gaseous Products

The ion current signal from water was difficult to interpret without using the DRIFTS spectra in Section 2.3.5. Some effusion of water can be observed at very low intensity across the entire temperature range. Effusion at low temperatures is due to physisorbed atmospheric water. At temperatures in excess of 120 °C, water would be observed as a product of thermochemical conversion if significant hydroxyl groups were present on the surface, however vibrational modes associated with -OH stretch modes were not observed in the DRIFTS spectra of any materials. Hence, we attribute the very small intensity >600 °C not to existing OH groups but to gasification reactions between other effusing species, for instance according to the well-known water-gas shift reaction ($CO_2 + H_2 \rightarrow CO + H_2O$).

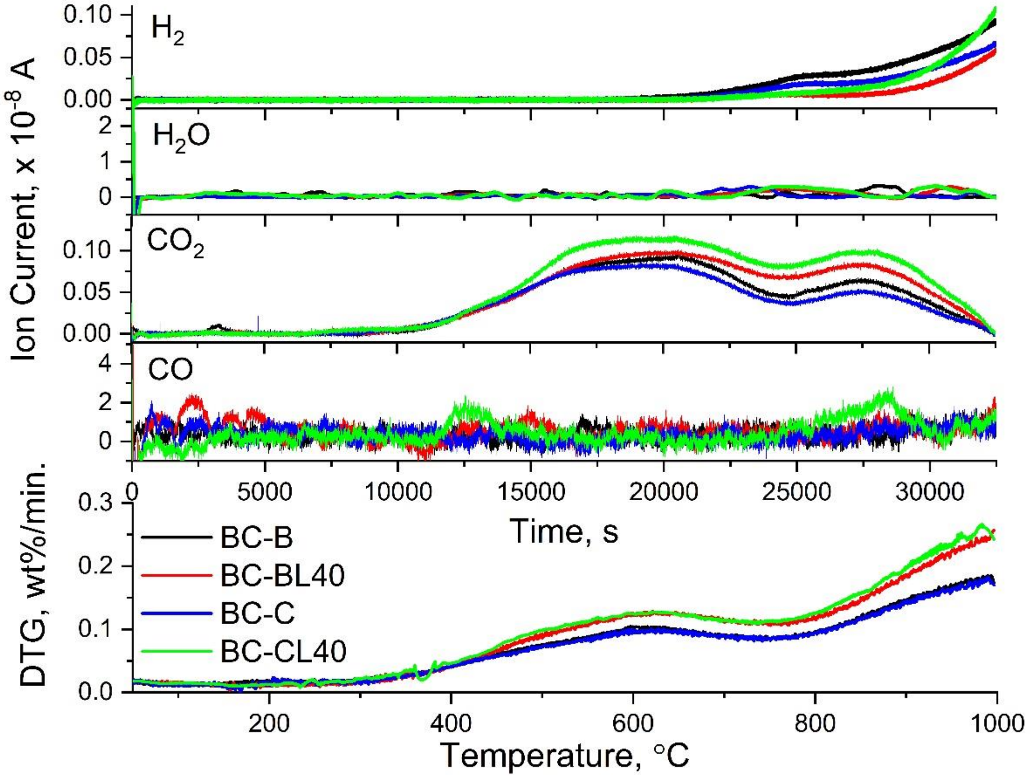

Figure 7: TGA-MS of effusing gases compared to the DTG signal for reference.

The effusion of CO is also observed in very limited amounts, primarily in BC-CL40, although some increase in CO effusion is observed for all biochars above 850 °C. Effusion below 450 °C is attributed to -C=O species on volatiles, while effusion between 450 - 750 °C is attributed to decomposition of carboxylic anhydrides and lactones, which contain two oxygens and are associated with sp^3 hybridized carbons [108]. The higher temperature regime, above 750 °C is attributed to quinone or pyrone groups associated with sp^2 hybridized carbon structures. CO_2 was produced in significant quantities above 450 °C. The small amount observed at approximately 120 °C is attributed to surface adsorbed atmospheric CO_2. From 450 – 750 °C a maximum is observed, which is attributed to decomposition of carboxylic anhydride and lactone groups. The maximum observed between 750 – 950 °C is attributed to ether and pyrone structures. The broad temperature range over which this effusion occurs is partially due to the 2°C/min. heating, but also indicates diversity in the local bonding environment of these groups. The enhanced effusion of CO_2 observed for demineralized biochars compared to untreated biochars over all temperatures is indicative of the lower oxygen content of untreated biochars due to the role of potassium catalysis in reducing oxygen content during the initial biomass pyrolysis [49,52]. BC-CL40 showed the most intense CO_2 signal, indicating the high S/G may produce more residual oxygen functionalities in absence of potassium compared to low S/G lignin. The higher oxygen content of demineralized chars agrees with observations by others for wood-based biochars, but the trend associated with S/G has not been previously reported [49,52]. This trend is supported by the DRIFTS results.

Hydrogen effusion begins above 700 °C with untreated biochars showing a broad peak at 800 °C. BC-B and BC-C show the highest hydrogen effusion below 900 °C and BC-BL40 shows the lowest. All biochars show significant increase in H_2 effusion above 900 °C, with BC-CL40 showing the most dramatic increase by 1000 °C. In amorphous carbons, interpretation of hydrogen effusion is complicated by its relationship to carbon structure and also to gasification reactions [106,109,110]. During high temperature pyrolysis, hydrogen effusion by thermochemical conversion results from hydrogen migration along the carbonaceous skeletal structures during carbonization processes at elevated temperatures. The temperature of hydrogen effusion from annealed amorphous hydrocarbon films was linked by Conway, *et al.* to the degree of cross-linking in sp^3 phases within the carbonized skeleton [109]. Those authors found that hydrogen effusion began >700 °C for films containing higher degrees of cross-linking in sp^3 phases (potentially even regions of diamond-like carbon) whereas carbons with significant low-density polymeric phases produced lower temperature hydrogen effusion. With regard to this present work, the hydrogen effusion profile corresponds with that observed by Conway for highly-cross-linked amorphous carbon, with demineralized chars potentially showing enhanced crosslinking as evidenced by the highest onset temperature for H-effusion.

Gasification provides an alternate explanation in the presence of other effusing species, particularly CO_2. Interaction between effusing gaseous species according to the water-gas shift reaction cannot be completely ruled out. The high intensity of the CO_2 profile observed for demineralized biochars in Figure 7 indicates that there may be sufficient CO_2 present to initiate the reverse water-gas-shift reaction and for temperatures up to 900 °C, hydrogen could be consumed. This behavior was not observed in demineralized chars. Above 900 °C sufficient CO_2 may not be present to drive that reaction, thus significant H_2 effusion is observed above 900 °C. If the assumption is made that no reactions are occurring between effusing CO_2 and H_2, the results can be tied directly to hydrocarbon structure, where potassium and S/G have very different effects. Demineralized chars may form more heavily cross-linked sp^3 phases. High potassium content coupled with high S/G resulted in less hydrogen associated with aromatic rings, hence larger aromatic ring clustering. With potassium largely removed, high S/G had the effect of reducing the size of aromatic rings. For instance, H-effusion for BC-C is higher than for BC-CL40 below 900 °C, but lower above 900 °C. For BC-B compared to BC-BL40, the untreated material has higher H-effusion through the entire range of temperatures, which is inconsistent with H/C for these materials. The basis for the latter is uncertain, comparison of the hydrogen effusion curves for the two demineralized chars indicates that BC-BL40 has the most cross-linking in sp^3 hybridized structures (lower effusion below 900 °C) with more aromatic ring clustering (lower effusion above 900 °C) compared to BC-CL40. For BC-B compared to BC-C, using the same arguments it is argued that BC-C contains more highly cross-linked sp^3 phases and larger aromatic ring clusters.

2.3.4.4. Biochar H/C as an Indicator for Aromaticity

H/C ratios for all biochars are reported in Table IV. In general, demineralization increased H/C, consistent with the trends observed for hydrogen effusion in Section 2.3.4.3. For BC-B and BC-BL40, the low S/G materials, demineralization increased the H-content by only 2.5 wt.%. For BC-C and BC-CL40, the high S/G materials, demineralization increased the H-content by 25 wt.%. Additionally, the effects of high K-content coupled with high S/G result in the lowest hydrogen content (H/C = 0.37), while demineralization of the same feedstock biomass produces biochar with the highest H/C (0.47).

Thermochemical conversion of original hydrocarbon structures of the feedstock biomass during pyrolysis reduces the content of hydrogen and oxygen by dehydration, demethylation and decarbonation reactions, with the degree of reduction in H and O strongly correlated to HTT [46,68]. The reduction in atomic ratios of hydrogen to carbon, H/C, and oxygen to carbon, O/C, are indicators of the extent of these decomposition reactions. This behavior is often represented in a Van Krevelen diagram, in which H/C is plotted vs. O/C or (O+N)/C [68]. H/C is often referred to as the aromaticity index and (O+N)/C as the polarity index for a particular hydrocarbon. Van Krevelen proposed this model in the 1950's for ranking coal, therefore the link between H- and O- content and aromaticity of hydrocarbon materials has been understood for a very long time. More recently, though, H/C has been proposed by Xiao, *et al.* as a simple metric for high temperature biochars linking HTT, size of aromatic clusters, and sorption of organic polyaromatic hydrocarbons [47]. In a comprehensive report which compiled the results of others for previously reported values of H/C as well as their own results for more than three dozen unique feedstocks, those authors found that H/C had a distinct relationship with temperature, which could be modelled using a logistic equation (Figure 2A and 2B in reference [47]). From this, they developed an equation relating H/C to aromatic cluster size based on the assumption of rectangular clusters. The assumption that clusters have a rectangular shape is not definitive, but a way of representing the average degree of clustering within a material, thus the Xiao model was designed such that it would account for oddly shaped aromatic clusters such as those proposed by Brewer, *et al.* and Bourke, *et al.* [52,111]. One observation which can be made from Figure 2A, [47] is that despite the readily apparent general trend in H/C vs. temperature, significant variability still exists in absolute value of H/C that is dependent on feedstock.

Regardless, it is proposed in this present work that the Xiao model represents a very useful starting point for understanding feedstock effects. Since all biochars in this present study were pyrolyzed under identical conditions, variation in H/C is conclusively related to differences in size/shape of aromatic clusters and content of polymeric carbon induced by feedstock alone and not temperature. According to the model:

Eq. 1
$$\frac{H}{C} = \frac{2+2m+2n}{2mn+2m+2n}$$

Utilizing H/C for all biochars reported in Table IV and assuming a hypothetical small cluster size with m = 3 gives n = 4.7, 4.3, 6.1, and 2.9 for BC-B, BC-BL40, BC-C, and BC-CL40, respectively. These results indicate that reduction in potassium content for high S/G materials reduces cluster size by nearly half, while for low S/G materials the effect of potassium on cluster size is negligible. The role of potassium in catalyzing condensation reactions appears to have the greatest effect for high S/G lignin, indicating some synergy among these parameters in determining cluster size. From the calculated n-value, the smallest cluster size was observed for the high S/G, low K biochar, whereas the largest cluster size was observed for the high S/G, high K biochar.

2.3.5. Surface Chemistry Investigation via DRIFTS

Background-subtracted, normalized DRIFTS spectra for the high wavenumber region and the fingerprint region for all biochars are shown in Figures 8a and 8b, respectively. Some characteristic frequencies are annotated in both figures. All spectra have been normalized to the maximum at 1585 cm^{-1}, the aromatic ring C=C stretch, based on the assumption of roughly the same number of aromatic rings per Raman spot size as evidenced by identical I(D)/I(G) reported in Table VI. It is important for the reader to remember that DRIFTS is a semi-quantitative tool, therefore the reason for normalizing the spectra is that it lessens the impact of slight differences in concentration due to inhomogeneous mixing with KBr within the sample holder.

In Figure 8b, the most prominent feature in all four materials is the aromatic C-C stretch at ∼1585 cm^{-1} with alkane C-H bend modes present between 1500 – 1350 cm^{-1}, and aromatic ring C-H out of plane modes between 900 – 700 cm^{-1}. There are three oxygen-related modes, apparent in the C=O conjugated lactone/quinone stretch at 1690 cm^{-1}, the aliphatic ether C-O-C mode at 1050 – 1000 cm^{-1} and aromatic ether mode 1300 – 1210 cm^{-1} [101]. At higher frequencies, several bands associated with C-H stretches of sp^2 and sp^3 carbons are observed in Figure 8a, however no O-H stretch modes are present which likely rules out the presence of phenolic structures and carboxylic acid groups. It does not rule out the presence of carboxylic anhydrides. Importantly, there is no distinct adsorbed water background, consistent with the low

MS water signal and the low moisture content reported in Table IV. This indicates limited adsorption of atmospheric H_2O.

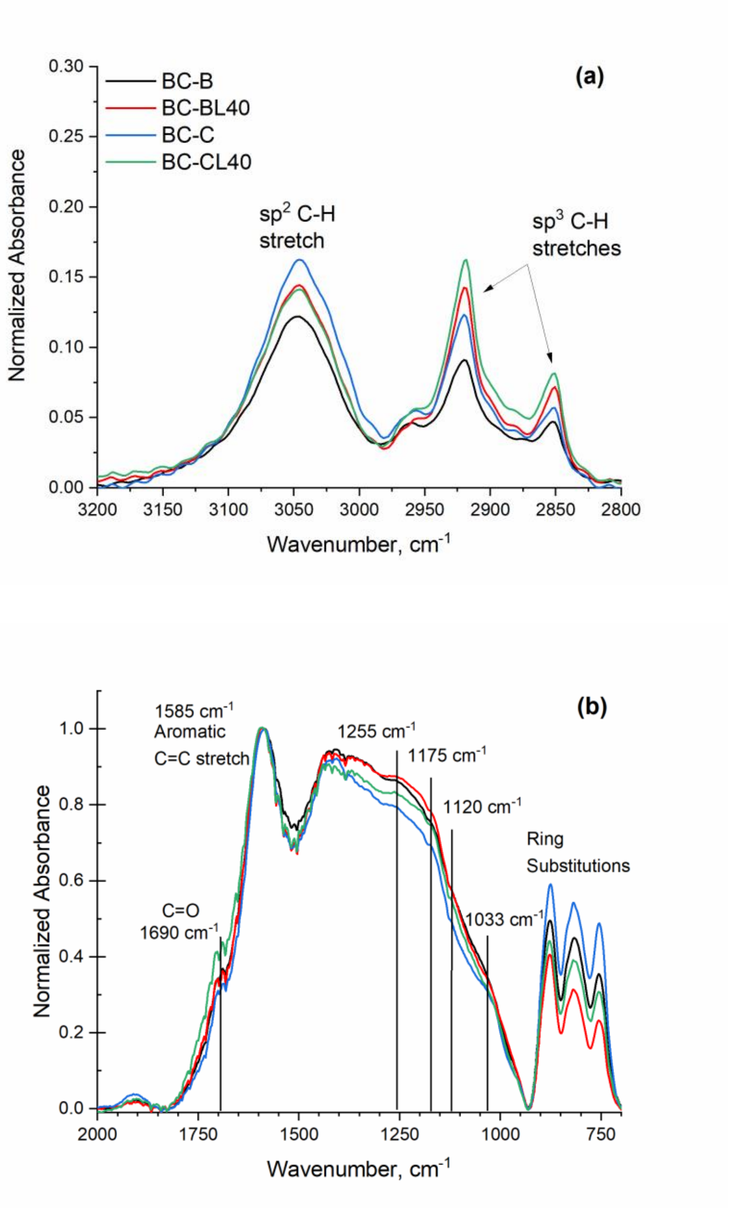

Figure 8: Background-subtracted, normalized DRIFTS Spectra for all biochars. All spectra were normalized to the peak intensity at 1585 cm^{-1} to compare relative intensities of O- and H-containing functional groups. Normalization was done under the assumption of equivalent content of aromatic carbon.

Despite the general similarity in DRIFTS spectra for these biochars, which is attributed to identical pyrolysis conditions, there are some apparent differences in normalized intensity for the characteristic H- and O- containing groups which can be attributed to feedstock. Consistent with variations in H/C in Section 2.3.4.4, differences in intensity associated with hydrogen functional groups are most apparent, and appear to correlate with both S/G and K. In Figure 8a, vibrational modes due to hydrogen associated with sp^2 hybridized carbon (3050 cm^{-1}) and specifically with aromatic ring substitutions (900 – 700 cm^{-1}) indicate BC-C has the most hydrogen associated with these structures. High S/G and low K-content produced lower intensity associated with these groups. For low S/G, demineralization increased the intensity of the band at 3050 cm^{-1} but reduced the intensity of the bands at 900 – 700 cm^{-1}, consistent with the increase in clustering of aromatic rings. The amount of hydrogen associated with sp^3 hybridized carbon showed dependence on K-content, with intensity in the bands between 3000 – 2800 cm^{-1} increasing with demineralization. These results agree with the those from H-effusion analysis and H/C.

Because DRIFTS is a semi-quantitative technique and peak-fitting was not conducted, it is challenging to draw definitive conclusions based on intensity between 1400 – 1000 cm^{-1}. Demineralization has the effect of slightly increasing the intensity between 1300 – 1000 cm^{-1}, which could be attributed to the increase in hydrogen or ether groups, as both C-H bend and C-O-C stretch modes are present in this region. The C=O stretch at 1690 cm^{-1}, attributed to the presence of carboxylic anhydride, quinone and pyrone structures, was most intense for BC-CL40 and least intense for BC-C, in general agreement with the CO_2 effusion results of Section 2.3.4.3 [112,113].

2.3.6. Raman Investigation of Carbon Structure

Raman spectroscopy is used extensively for characterization of amorphous carbon and carbon allotropes because of its high sensitivity to sp^2 hybridization. Biochars are notoriously “messy” materials which contain sp^2 and sp^3 hybridized carbons and heteroatoms within different types of structures, but Raman is effective regardless of the sp^2/sp^3 configuration. Sp^2 hybridized carbon in pyrolytic materials is usually assumed to form aromatic rings, however linear conjugated sp^2 structures can exist as well. Because of the low band gap, sp^2 hybridized carbon bonds have stronger Raman scattering cross section compared to sp^3 hybridized carbons, thus at visible wavelengths the Raman spectrum for amorphous carbons, including biochar, is dominated by that which is due to sp^2 carbon [114].

The dominant features of the biochar Raman spectrum occur in the first-order region between 1000 – 1800 cm^{-1} and are known as the G and D peaks. The G peak originates from bond stretching of sp^2 hybridized carbon pairs, thus both aromatic rings and linear chains exhibit a G peak. The so-called G peak (for graphite) originates from the E_{2g} Raman allowed optical phonon mode at the Brillouin zone center, $\mathbf{\Gamma}$. G peak intensity is considered to be directly proportional to the sp^2 content regardless of defect content [115]. The G peak full width at half maximum, FWHM(G), shows an inverse relationship with the degree of ordering, and saturates at around 15 cm^{-1} for large graphite crystals, however, in amorphous carbons FWHM(G) is generally much wider, often exceeding 100 cm^{-1} [116].

The D peak is only observed when aromatic rings are present because it is due to ring-breathing of aromatic rings. The D peak originates from the A_{1g} optical phonon at $\mathbf{K}$, which is activated by relaxation of the fundamental Raman selection rule caused by the presence of defects such as sp^3 hybridization or very small cluster size [117]. Different types of defects can activate the D peak, for instance edges of ordered sp^2 clusters, sp^3 hybridized species, or heteroatoms. A mathematical relationship between D peak intensity and size of pristine aromatic clusters was developed by Tuinstra and Koenig, but applies only to structures approaching the graphitic limit and therefore does not apply to highly amorphous carbon systems like biochars [118].

Much work has been done to understand the complex Raman spectra of biochars, particularly high temperature chars which are expected to have increased clustering of sp^2 phases. Smith, *et al*. have employed the molecular approach similar to that of Castiglioni, *et al.* in an effort to deconstruct the Raman spectrum of cellulose char [119,120]. Those authors utilized molecular dynamics simulations and model gas phase molecules such as polyaromatic hydrocarbons and trans-polyacetylenes in the development of a model which accurately represents clustering, non-benzene rings, 5- and 7-membered rings, oxygenated structures, vacancies and other defect types. The resulting model incorporates nine Gaussian peaks and one Lorentzian (G peak) which fits raw spectra well, however we propose that with so many degrees of freedom there is a risk of "overfitting". Others have proposed more simplified models, for instance Sadezky, *et al.* have proposed a model for the Raman spectra of diesel soot, implementing a G peak and four D peaks, in which D1 represents the commonly known D peak.

Another model, proposed by Ferrari and Robertson, *et al.* to characterize amorphous carbon films, could account for the Raman D and G peaks in biochars [117]. This model has not been applied extensively to biochars. According to this model, two peaks can satisfactorily fit the first order region, between 1100 – 1700 cm^{-1}. Three parameters for these fitted peaks, position of the G peak (Pos(G)), FWHM(G), and ratio of intensity of the D peak to that of the G peak (I(D)/I(G)), are related to the average degree of order and aromaticity in the material. It is proposed here that this model is appropriate for pyrolysis chars because it accounts for the well-known non-graphitizing behavior, fine size distribution of sp^2 and sp^3 domains, the presence of 5-, 6-, 7- membered aromatic rings, linear conjugated chains, hydrogen and heteroatom content of biochars without risk of “over-fitting” [52,61,117]. This model utilizes only two peaks between 1000 – 2000 cm^{-1} whose parameters are associated with [121]:

1) clustering of sp^2 phase
2) bond-length and bond-angle disorder
3) presence of sp^2 rings or chains
4) sp^2/sp^3 ratio
5) H-content

According to the model of Ferrari and Robertson, the D peak was fit with a single Lorentz function, the G peak was fit with a single Breit-Wigner-Fano function (BWF), and the photoluminescent background was accounted for by including a linear background. A sample fitted curve is shown in Figure 9. Three measurements for each material were taken from three different particles randomly selected within the sample. The average for each parameter is reported in Table VI along with the standard deviation.

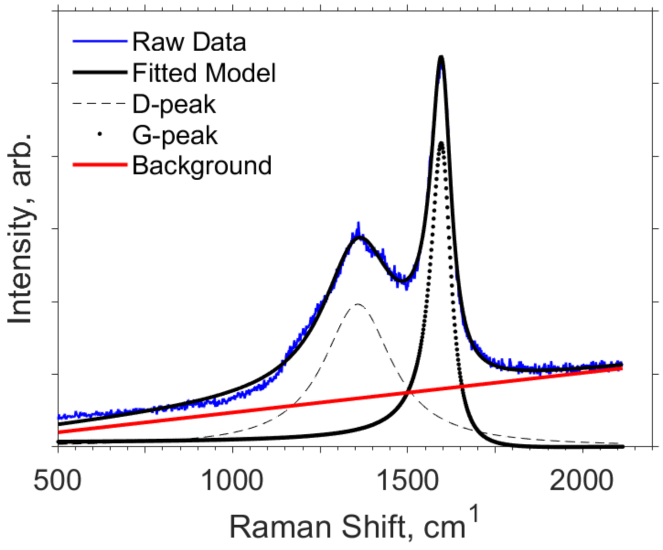

Figure 9: Example of the 2 peak fit of the first-order region of the Raman spectrum used for all materials, in this case BC-B, using 457 nm laser excitation. Raw data (blue) was fit with a Lorentzian D-band (Dashed line), BWF G-band (dotted line) and linear background (red line).

Table VI: Results of peak fitting D and G bands of Raman spectra

	Pos(G)	ID/IG	FWHM(G)
BC-B	1597	0.54	81
BC-BL40	1596	0.55	81
BC-C	1597	0.53	75
BC-CL40	1596	0.53	81

Results of Raman spectroscopy indicates that all biochars contain sp^2 hybridized carbon in the form of rings and chains, evidenced by Pos(G) near 1600 cm^{-1} [121]. Clusters of aromatic rings are indicated by the presence of a D band. I(D)/I(G) was equivalent for all materials, indicating equivalent content of aromatic rings within the laser spot. It is extremely important to note that the size of aromatic clusters cannot be determined by the I(D)/I(G) according to the Tuinstra-Koenig relations [118]. Rather I(D)/I(G) refers to the number of aromatic rings within the laser spot for highly amorphous carbons [121]. For instance, two materials could contain slightly larger clusters and still have the same I(D)/I(G) as a material with single aromatic rings as long as the average number of rings within the laser spot was the same. If that were the case, crosslinking and distribution of sp^3 hybridized carbon phases and hydrogen- and heteroatom content could account for this behavior. No statistically significant difference was found in fitting parameters among the four materials with the exception of FWHM(G) for BC-C. This material showed a mean value for FWHM(G) of 75 cm^{-1}, compared to 81 cm^{-1} for all other materials indicating that material shows more ordering of all sp^2 phases. This could manifest as either larger or just less defected aromatic ring clusters, including lower heteroatom content.

2.3.7. Specific Surface Area and Porosity

Nitrogen volumetric adsorption studies describe the pore space accessible to diatomic nitrogen, which makes this highly effective at assessing microporosity in a wide range of materials [63]. The results of N_2 adsorption calculations for S_{BET} and pore volume are in Table VII. N_2 isotherms are shown in Appendix A. Untreated biochars showed extremely low surface areas and associated pore volume. The root source for this has not been determined, although repeat measurements using different instrumentation (Micromeritics TriStar) support these results as accurate. Demineralized biochars show moderately high surface area, with 11% greater S_{BET} for BC-BL40.

Table VII: Textural properties of untreated and demineralized biochars

	S_{BET}, m^2 g^{-1}	Pore Volume, ml g^{-1}
BC-B	1	-
BC-BL40	427	0.1
BC-C	1	-
BC-CL40	382	0.2

Pore formation is initiated during pyrolysis as gases and volatiles escape the bulk, leaving voids. The rate of evolution and the amount of these species produced during pyrolysis largely determines pore structure. Open pores are formed when these gases escape efficiently from the bulk, exposing these spaces between aromatic layers to larger channels, known as mesopores. If the porosity is sufficiently open, adsorbates can enter micropores where dispersion forces are strongest, and remain for a longer period of time than molecules adsorbed on macropore surfaces. If volatiles are not able to exit the bulk material during pyrolysis, they can clog pathways out of the structure, resulting in “closed porosity”.

Activation processes are designed to prevent or remove closed porosity in activated carbon and increase surface area available to adsorbates, but in biochar some level of closed porosity is expected to exist [27]. Surface area measurements in biochars can vary dramatically for this reason. While activation with KOH is often used to open pores in commercial activated carbons, and has been observed to have the same effect in biochars when added to demineralized biomass feedstock, naturally-occurring potassium has not shown the same effect [27,56]. This may indicate naturally occurring potassium does not have high enough catalytic activity to increase the rate of or quantity of volatiles production and thus outweigh other feedstock effects on pore formation. Others have observed higher volatiles production during pyrolysis for demineralized biomass from woody and herbaceous sources [49,53,88]. It is noteworthy that volatiles content for all biochars only differed by 0.06 wt.%, therefore, pore clogging by volatiles is not likely to be the root cause of the low S_{BET} for the untreated biochars. More likely that volatiles were trapped in the char structure during pyrolysis (thus not leaving by common channels associated with the formation of mesoporosity and interconnected pores) and underwent secondary reactions with the primary char structure. This would result in mostly closed porosity within the structure. The higher char yield for untreated biochars may also be indicative of this behavior.

Lignin S/G effects on S_{BET} are also apparent. In comparing S_{BET} for the two demineralized biochars, BC-BL40 shows an 11% higher S_{BET} compared to BC-CL40. This has not been reported by others previously. According to the fundamental description of pore formation, above, this result can be attributed to enhanced quantity and rate of formation of gaseous products and volatiles. Relating this directly to lignin S/G, the higher S_{BET} char formed from lower S/G biomass. Since the activity of lignin monomers in pyrolysis has been directly linked to methoxy groups, by extension lower methoxy content produces higher volatiles and gas products yield. Asmadi *et al.* concluded O-CH_3 bond homolysis was the rate determining step in pyrolysis of syringol and guaiacol (alcohol derivatives of S and G, respectively) [95]. Guaiacol was observed to form more tar-based intermediates and OCH_3 rearrangement products compared to syringol. While those studies were performed with isolated substances and in closed ampule reactors, the findings indicate significant differences in tar and volatiles production at intermediate pyrolysis temperatures which could explain the findings in this present study. Additional studies to identify pyrolysis intermediates are planned to help explain this behavior.

2.4. Conclusions

The results of this study indicate that lignin S/G and naturally occurring potassium are both linked to the formation of textural and chemical properties of biochars. Because temperature also plays a strong deterministic role in biochar structure and chemistry, the following conclusions may only apply for biochars pyrolyzed at approximately 700°C, and at especially at higher temperatures these trends may not hold. High lignin S/G has been definitively demonstrated to reduce biochar yield, increase the total hydrogen- and oxygen-content. Results also indicate high S/G results in enhanced cross-linking in sp^3 phases and reduced size of aromatic ring clusters. The impacts of potassium content largely followed the expected trends observed by others, and in some cases appeared to have synergistic impacts with S/G. High naturally-occurring potassium content increased biochar yield, reduced oxygen-content, increased the order within sp^2 phases, and reduced the specific surface area and N_2-accessible pore volume of biochars definitively. Increased content of naturally-occurring potassium may also increase the size of clusters of aromatic rings and reduce cross-linking of sp^3 phases even in the presence of high lignin S/G. Lignin S/G and naturally-occurring potassium have synergistic impacts on biochar yield.

3. Breakthrough Behavior for Gas Phase Ammonia by Biochar[2]

3.1. Introduction

Global atmospheric ammonia emissions have been growing steadily for decades, with total emissions in 2015 reaching 49.1 megatons [8]. Animal waste in concentrated animal feeding operations and over-application of ammonia-based crop fertilizer are the largest contributors. Other primary sources are concrete and fertilizer manufacturing, vehicular emissions, and some natural sources like wildfires and volcanic activity [3,5,9,122]. Atmospheric ammonia increases particulate matter in the air and reduces air quality with associated negative implications for human and environmental health and climate [9,122,123]. In the environment, increased atmospheric ammonia influences the pH of precipitation, acidifies surface waters, and enhances eutrophication of both soil and aquatic systems with toxic effects on native flora and fauna leading to a reduction in biodiversity [9].

Recognition of NH_3 as an important factor in global health and climate change has prompted action to identify mitigation strategies, with biochar coming to the forefront as a carbon neutral and effective means of reducing agricultural ammonia emissions [28,29,32]. Biochar is the solid product of pyrolysis of lignocellulosic materials at moderate temperatures (250 – 900°C). When sourced from regionally available agricultural or forestry wastes, it represents a carbon sequestration mechanism with useful adsorbent properties [43,45]. Biochar application to manure-based compost can reduce ammonia emissions from those sources by >50%, with highly oxidized chars showing potential for long-term NH_3 sequestration due to strong chemisorption between organic acid groups and ammonia [28,32]. Ammonia emissions

---

[2] Muretta, J.E., LaDouceur, R., Kirtley, J.D., Prieto-Centurion, D. Breakthrough Behavior for Gas Phase Ammonia by Biochar. *Manuscript Submitted*

from process-based sources represent significant and largely underestimated quantities of gaseous ammonia emitted globally [5,124,125]. A recent survey of satellite ammonia emissions data agrees with the global average results for ammonia emissions by EDGAR, however those authors found that the impact of point source concrete and fertilizer manufacturing emissions were underrepresented by an order of magnitude [5,8]. The recent successes of biochar in mitigating ammonia from static sources suggest that biochar may perform well in removing ammonia from process streams as well. However, the results of static or quasi-static adsorption studies do not provide enough information on the performance of an adsorbent under dynamic conditions. For that, dynamic adsorption, or breakthrough testing, is needed. Results from ammonia breakthrough testing with biochar are absent from the literature, therefore this study represents a preliminary step toward building that knowledge base.

Biochar can contains acidic surface functional groups like carboxylic -COOH and phenolic -C-OH, as well as lactone and quinone -C=O, and epoxide and ether C-O groups that have been observed to function as hydrogen-bonding and chemisorption sites for ammonia molecules [24,28,73]. Huang, *et al.* investigated the role of surface acid groups on dynamic ammonia adsorption by using acid-treated activated carbons and found that the dynamic adsorption capacity scales with quantity of these acidic surface oxygen groups [24]. For optimal performance, it could be reasoned that a high surface area char with high levels of acid sites are most attractive. However, for biochars in dynamic ammonia adsorption, the respective roles of high surface area and acid-groups are not well-characterized, and may in fact prove to be conflicting. Domingo-Garcia, *et al.* demonstrated that for ammonia adsorption onto oxidized activated carbons, access to micropores, which represent a very high proportion of the surface area for activated carbons, diffusion into micropores can be hindered on short time scales relevant to dynamic adsorption by oxygenated functionalities at pore openings [73]. For biochars, the relative amounts of acid functional groups and their accessibility during dynamic adsorption is likely to depend on pyrolysis conditions, feedstock, and any additional treatments [28,46,66,107].

The specific aim of this present work was to build on the current state of understanding for biochar as an ammonia mitigation tool by investigating its potential in removing gaseous ammonia in a flowing gas stream using breakthrough experimentation. Primary focus was placed on correlating surface area and surface chemistry of the materials to their breakthrough behavior. To do this, breakthrough curves from four different wood-based biochars having different textural and chemical properties and a commercial activated carbon designed for general gas purification were measured. The secondary goal of this work was to investigate whether a common model for gas adsorption onto activated carbon, the Wheeler-Jonas model, was appropriate for dynamic ammonia adsorption onto biochar under the test conditions. Verhoeven and Lodewyckx have found the Wheeler-Jonas model appropriate for a dynamic adsorption study of air contaminated with ammonia on activated carbon [126].

3.1.1. Dynamic Adsorption Methodology

Dynamic adsorption, or breakthrough experimentation, is a common means of investigating adsorbent performance in water treatment, industrial separation and solvent recovery, catalysis, and respirator filtration [127–129]. It is conducted with the adsorbent in a packed bed configuration, with gas flow containing a constant concentration (C_0) of target contaminant, also called the “challenge concentration”, directed through the packed bed. Unlike static, or equilibrium, adsorption experiments, dynamic adsorption can reveal the useful lifetime of a material under a particular set of process conditions, as well as information about the total capacity and overall rate of uptake based on both the process variables and materials properties rather than purely on the material as is the case with static experiments.

The concentration profile in a breakthrough experiment has three primary regions, illustrated in Figure 10. As contaminant is introduced to the adsorbent bed, the adsorbent will have the capability to remove all of the contaminant before the flow front reaches the end of the bed. This is known as the unsaturated region because the adsorbent bed is largely unsaturated and effluent concentration equals zero. In the second region, the mass transfer zone (MTZ), adsorbent particles are actively taking up contaminant, however the rate of uptake is not high enough to remove all of the contaminant from the flow stream, and a spatial concentration gradient develops through the bed. The shape is reflective of the rate determining processes which are dominant at different concentrations. The final region, the plateau region, occurs where the adsorbent is largely saturated and effluent contaminant concentration is equal to, or nearly equal to, the inlet concentration. The MTZ shape is reflected in the shape of the breakthrough curve, and has a characteristic sigmoidal shape with varying degrees of symmetry about the inflection point. In industrial processes, it is desirable for the slope of the concentration curve in the MTZ to be very steep, because this implies rapid, uniform adsorption throughout the bed, and optimizes the useful lifetime of the adsorbent.

Once a toxin is introduced to the adsorbent bed in a dynamic flow experiment, the length of time it takes for a predetermined concentration of contaminant, usually <10% of C_0, to be reached at the effluent side of the bed is called the breakthrough time. This time includes the unsaturated portion of the concentration curve and the onset portion of the MTZ (Figure 10). Breakthrough time is a function of process variables like flow rate and C_0, as well as particle size, bed weight, bed density, and the microstructure and surface chemistry of the adsorbent. For a given set of process conditions, the breakthrough time is governed largely by the uptake capacity of the material, with the rate coefficient refining the shape of the low C/C_0 portion of the curve.

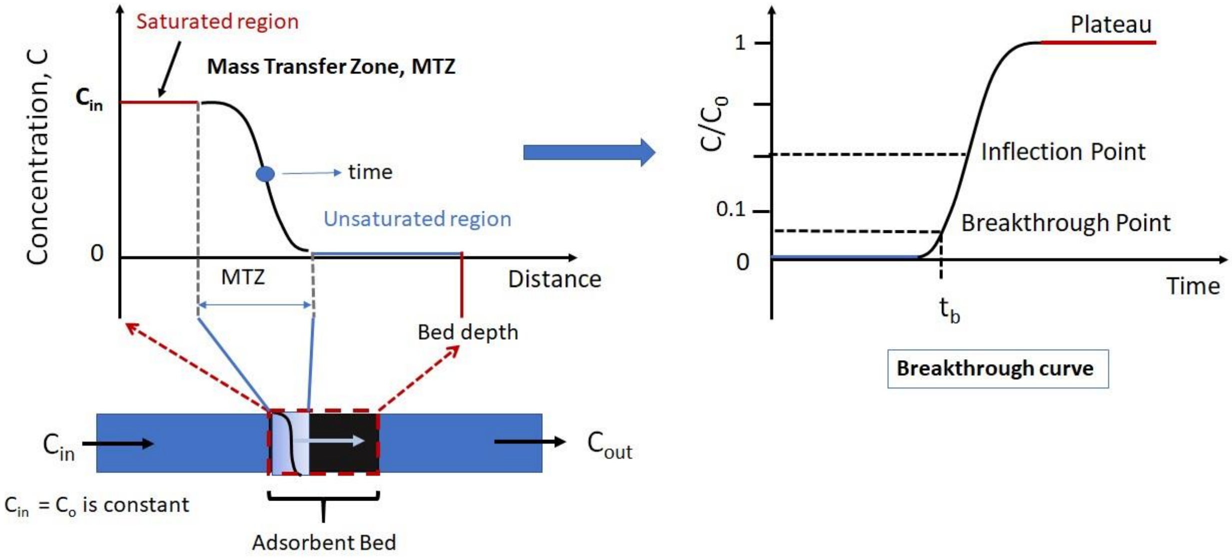

Figure 10: (left) Schematic of the packed bed and concentration gradient and (right) breakthrough curve for a typical breakthrough experiment. In the diagram at lower left, the superimposed MTZ does not imply any radial dependence of the concentration gradient, it is just shown to help the reader understand the axial dependence. In fact, the assumption of no radial dependence is made for breakthrough experiments. The shape of the breakthrough curve (right) reflects the shape of the MTZ moving though the bed over time.

3.1.2. Wheeler-Jonas Model

The independent process variables and material properties impact both the length of time associated with the unsaturated region and the slope of this onset portion of the mass transfer zone curve. These effects are often quantified using the Wheeler-Jonas equation. The Wheeler-Jonas equation is a semi-empirical predictive model developed by Wheeler to describe catalyst poisoning by H_2S in a fixed bed reactor based on conservation of mass within the column [128]. While the Wheeler-Jonas equation has been applied for activated carbon/contaminant systems by others, it was not known *a priori* whether ammonia/biochar system and flow conditions would result in appropriate use of this model for this present study [70,126,129,130]. Here, the Wheeler-Jonas equation was applied to two biochars and the activated carbon to extract the overall rate coefficient, maximum adsorption capacity, and critical bed depth needed to prevent breakthrough for these materials. Those materials were selected because they showed very different breakthrough times, thus allowing an assessment of the appropriate use of the Wheeler-Jonas equation for the biochar and ammonia system. The Wheeler-Jonas equation is:

Eq. 2

$$\boldsymbol{t_b = \frac{W_e}{C_0 Q}\left[W - \frac{\rho_B Q}{k_v} ln\left(\frac{C_0}{C_x}\right)\right]}$$

where t_b is breakthrough time, W_e, is the kinetic capacity or maximum adsorbent capacity, k_v, is overall rate coefficient for the process, Q is volumetric flow rate, C_0 is the constant inlet concentration, C_x, is the time-dependent concentration of the effluent, ρ_B is bed density, and W is the mass of the adsorbent bed. W_e is material-dependent, while k_v is dependent on the process conditions and particle size.

Yoon and Nelson made the following modification to account for reversible adsorption [129,131,132]:

Eq. 3

$$\boldsymbol{t_b = \frac{W_e}{C_0 Q}\left[W - \frac{\rho_B Q}{k_v} ln\left(\frac{C_0 - C_x}{C_x}\right)\right].}$$

Verhoeven and Lodewyckx found this form of the Wheeler-Jonas equation appropriate for ammonia adsorption onto activated carbon [126]. Dynamic ammonia adsorption on oxidized activated carbon was found to exhibit both reversible and irreversible components, however, making the use of Wheeler-Jonas uncertain for biochars where the degree of chemisorption compared to reversible physisorption is not known [73]. In the present work, processes associated with breakthrough, i.e. boundary layer diffusion and surface physisorption, which are reversible, were initially assumed to be dominant and Eq. (3) was used rather than Eq. (2). Discussion in Section 3.3.4 and 3.3.5 address the legitimacy of this assumption.

The Wheeler-Jonas model can be useful in predicting breakthrough time for a particular mass of adsorbent bed when all variables including W_e and k_v are known, which is the most common application. But for a new material with uncharacterized behavior it can also be used in the reverse form to estimate W_e and k_v [129]. According to this method, breakthrough curves are measured for at least two different masses of bed weight. A linear curve is fitted to the breakthrough times versus bed weight, W. The slope and y-intercept are then applied using Eq. (4) and (5), derived from Eq. (3), to calculate W_e, k_v:

Eq. 4
$$\boldsymbol{slope = \frac{W_e}{C_0 Q}}$$

Eq. 5
$$\boldsymbol{intercept = -\frac{1}{k_v}\left(\frac{W_e \rho_B}{C_0}\right) ln\left(\frac{C_0 - C_b}{C_b}\right)}$$

Eq. 6
$$\boldsymbol{W_c = \frac{\rho_B Q}{k_v} ln\left(\frac{C_0 - C_x}{C_x}\right)}$$

where C_b is the pre-selected concentration where breakthrough is measured. The critical bed weight, W_c, which is the mass of adsorbent needed to prevent immediate breakthrough, can be calculated from Eq. (6), which was derived from Eq. (3) by setting $t_b = 0$ once W_e and k_v are known. In the present work, this second application of the Wheeler-Jonas equation was used to 1) compare W_e, k_v and W_c for biochars vs. a commercial activated carbon, and 2) to determine the appropriateness of the Wheeler-Jonas model for ammonia adsorption onto biochar under dynamic conditions.

3.2. Materials and Methods

3.2.1. Materials Preparation

It was important in this study to select materials with different textural and chemical characteristics so that the breakthrough behaviors could be correlated to particular properties. For this reason, two low surface area biochars, two high surface area biochars, and one high surface area activated carbon were selected as comparative adsorbent materials. The biochars were prepared from two different genetic variants of *P. trichocarpa*, black cottonwood, which are compositionally very similar, but produced biochar with different chemical structure. This effect is particularly relevant upon demineralization of the feedstock biomass [49,86]. Norit RB3 was selected as a comparative, high-surface area activated carbon for its use in general gas adsorption.

As-received wood chips from the two *P. trichocarpa* variants were ground and sieved to ~1 – 2.5 mm. A portion of each was washed (demineralized) to remove alkali and alkali earth metals, a process which is known to increase surface area and oxygen content in the resulting biochars [49,52]. To demineralize the feedstock, ~10g of this sieved material were added to 1L of Type I water and soaked for 40 hours. These samples were drained and dried in flowing air at room temperature for at least 48 hours and then at 65°C for 24 hours.

Untreated and demineralized feedstock biomass were pyrolyzed in a tube furnace (MTI OFT-1200X) and heated under flowing argon (3.0 L/min.) at ~15°C/min. to 700°C, with a 5-minute dwell at this temperature to equilibrate the heating zone, then cooled in flowing argon to <50°C before removing from the tube furnace. Biochar was sieved to -80+100 mesh (~150 µm) for breakthrough experiments. Norit RB3 was received in pelletized form, and was ground and sieved to -80+100 mesh prior to use. All materials were stored at 75 °C for 48 hours prior to testing to reduce surface water content.

3.2.2. Materials Characterization

Raman measurements of undiluted, powdered samples were made on a Renishaw Raman Microscope using a 20x LWD objective and the 514 nm emission line from an argon ion laser at 3 mW power and 1 – 5 µm spot size. Scans were taken between 500 – 2300 cm^{-1} with 3-5 second accumulation time and 5 – 20 repetitions in order to achieve sufficient signal/noise. For each material, measurements were made from 3 – 5 locations to assess material homogeneity. The model proposed by Ferrari and Robertson for amorphous carbon was used to fit a Lorentzian and a Breit-Wigner-Fano (BWF) function to the D and G peaks, respectively an a linear background to account for photoluminescence [117]. Fits were conducted on cropped, raw data between 1000 – 2000 cm^{-1}. The reported peak parameters represent the mean and standard deviation of fitted parameters for at least three measurements.

Surface chemistry was characterized using diffuse reflectance Fourier transform infrared spectroscopy (DRIFTS). All data were taken on a Shimadzu IR Tracer100 with a Harrick Praying Mantis DRIFTS attachment and mercury-cadmium-telluride detector cooled with liquid N_2, with atmospheric correction applied to raw absorbance spectra. Samples were ground using mortar and pestle, diluted to ~7% wt. in KBr, and ground further with the KBr prior to taking measurements. Absorbance spectra were measured in the 4000 – 400 cm^{-1} range at 4 cm^{-1} resolution with 120 accumulations. At least three samples for each material were measured to evaluate material homogeneity. A representative spectrum for each material is shown in Figure 11.

Apparent surface area and pore volume were characterized using N_2 adsorption measurements between 10^{-4} and 100 kPa at 77K on a Micromeritics 3Flex automated volumetric adsorption instrument. The samples were degassed at 130°C under oil-free vacuum to 10^{-9} kPa for 4 hours prior to measurements. Specific surface area was calculated by the Brunauer-Emmett-Teller (S_{BET}) method between the lowest partial pressure and the maximum in the Rouquerol plot [63]. Total pore volume was calculated by the single-point method at $P/P_0 = 0.95$ [105].

The content of adsorbed atmospheric water, or surface water, onto each material was measured by TA Instruments Q500 thermal gravimetric analyzer (TGA) by heating approximately 8 mg of each material in dry argon to 120°C for 1 hour.

H/C ratio was approximated with a TGA-MS procedure through coupling of the TGA and Pfeiffer Thermostar electron impact mass spectrometer (MS) in which materials were combusted in excess O_2, heating at 2 °C/min. to 800 °C, and the resulting weight loss differential curve plus the MS H_2O and CO_2 signals were utilized to quantify mass of each species in the sample. Calibration of the MS H_2O and CO_2 signals was done by heating calcium oxalate monohydrate under the same conditions. By repeating the calibration TGA-MS with three different masses of calcium oxalate monohydrate, and using the O_2 curve as an internal standard, a calibration curve for integrated MS signal vs. mass of H_2O and CO_2 was constructed. This method is similar to that used previously by others [103,104]. Application of the calibration to the integrated areas of the ion current signals for H_2O and CO_2 gave the atomic H/C ratios for each material.

3.2.3. Breakthrough Experimental Setup

For breakthrough experiments, ~0.5 g of adsorbent was used in a 15mm diameter custom glass column (Allen Scientific Glass, Inc.) shown in Appendix B. Particle size for all materials was 150 µm. Each sample was purged for 2 hours in flowing UHP N_2 (90 ml/min) at room temperature prior to testing. Volumetric flow rate for each test was set at 100 ml/minute (90ml/min. N_2, 10ml/min. 90% He/10% NH_3). Challenge concentration was 1% ammonia by volume. Effluent NH_3 was measured by MS, tracking the m/z = 17 signal. Inlet concentration of ammonia was controlled using bottled gases and a Coriolis flow meter for ammonia/He and thermal mass flow meter for N_2. The flow of ammonia was shut off after approximately 60 seconds to reduce wear on the mass spectrometer, thus only the initial breakthrough was measured for these materials. System response time, including dead volume in the column, was accounted for by testing a blank column under the same process conditions, including the mass of glass wool and glass bead packing. Three breakthrough experiments were run for each material and the x and y components of these curves were averaged using Origin software. The time at $C/C_0 = 0.01$ and 0.10 in the system response curve was subtracted from the corresponding time measured from the averaged curves for each material. The resulting corrected curves are shown in Figure 13a,b. No correction for reduction of ammonia in the flow stream was made because of the low challenge concentration. Breakthrough time was reported for $C/C_0 = 0.01$ and 0.10.

3.3. Results and Discussion

3.3.1. Raman Characterization

Biochars and activated carbons can have varying degrees of aromaticity, which generally refers to the level of defects in and the size of aromatic rings within the bulk of the material. Because micropores, which are formed from stacking faults between layers of aromatic ring clusters in porous carbons, are responsible for high surface area in these materials, it is critical to characterize these phases formed of sp^2 hybridized carbons. Raman spectroscopy provides a simple, non-destructive means of achieving this due to the high Raman activity of sp^2 carbons. Processing largely controls aromaticity for both biochars and activated carbons, with activated carbons typically exhibiting much higher aromaticity than even high temperature biochars because they have undergone activation coupled with processing at much higher temperatures. Both materials, however, are considered non-graphitizing, which means that even after very high temperature heat treatment for long times, the basic crystallite structure will remain too defected to be considered graphitic [57].

The Raman spectra of Norit RB3 and all biochars are presented in Figure 11. All materials showed characteristic D (~1350 cm^{-1}) and G (~1600 cm^{-1}) peaks associated with amorphous carbon [121]. The G peak arises from in-plane C-C stretches of sp^2 hybridized carbons in both linear chains and aromatic rings. The D peak arises from breathing modes of aromatic rings, and is associated with in-plane disorder in clusters of aromatic rings. Raw spectra for each material were fit using the 2-peak model proposed by Ferrari and Robertson which accounts for the D and G peaks, as well as the characteristic high intensity of the valley region between the D and G peaks in amorphous carbons, a category which includes both activated carbon and biochar [117,121]. According to this model, the D band is fitted with a single Lorentzian function, and the G peak is fitted using a BWF function which accounts for the characteristic asymmetry of this peak as well as the intensity of the valley region [115]. Fitting two peaks and a linear background produces useful parameters by which materials can be compared. Results of fitting are reported in Table VIII. Note that laser power and excitation wavelength must be identical due to the energy-based dispersion of the D peak [115,121]. An example fitted curve is shown in Appendix B.

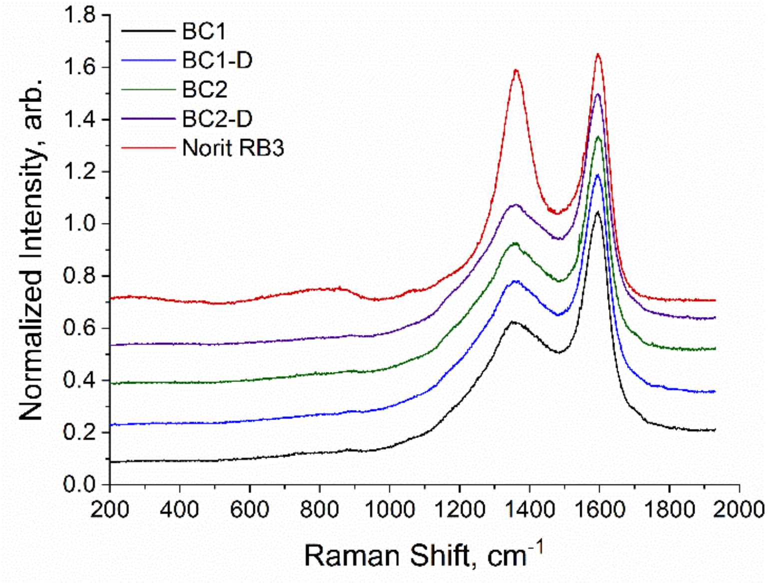

Figure 11: Raw, vertically offset Raman spectra for, from top down, Norit RB3, BC1, BC1-D, BC2, BC2-D. All show characteristic amorphous carbon peaks D and G, with a much more intense D-peak for Norit RB3 consistent with enhanced aromatic ring clustering.

Table VIII: Results of Lorentzian-BWF fitting of Raman spectra

	Pos (G), cm^{-1}	I(D)/I(G)	FWHM(G), cm^{-1}
BC1	1597 ± 1	0.54 ± 0.02	78.9 ± 2.5
BC1-D	1596 ± 1	0.55 ± 0.03	81.0 ± 1.5
BC2	1597 ± 2	0.53 ± 0.02	74.5 ± 2.5
BC2-D	1597 ± 1	0.53 ± 0.03	80.7 ± 1.5
Norit RB3	1602 ± 3	0.92 ± 0.07	77.4 ± 3.1

The results of peak fitting indicate differences in aromaticity between Norit RB3 and all four biochars. According to the Ferrari-Robertson model, the fitted parameters related to the position of the G band (Pos(G)), intensity ratio for the D and G peaks (I(D)/I(G)), and the full width at half the peak maximum for the G band (FWHM(G)) depend on the clustering of sp^2 phase, bond disorder, the presence of sp^2 rings vs. chains, and the content of sp^3 carbon within the amorphous carbon structure [117]. The high Pos(G) for all materials indicates low sp^3 content and the presence of some linear sp^2 chains. I(D)/I(G) was nearly twice as large for Norit

RB3 as for the biochars. I(D)/I(G) is related to the number of aromatic rings within the laser spot size, thus Norit RB3 has larger clusters of aromatic rings compared to the biochars. FWHM(G) increases monotonically with degree of disorder of sp^2 carbon phases in amorphous carbons [121]. According to FWHM(G) in Table VIII, all materials possess a similar degree of sp^2 disorder except BC2, for which the narrower G peak indicates slightly more ordering or all sp^2 components.

3.3.2. DRIFTS Characterization

In this work, DRIFTS spectra were used semi-quantitatively. Background-subtracted absorbance spectra for all materials are shown in Figure 12. From these spectra, all four biochars contained similar functional group chemistry. The spectrum of Norit RB3 had very low overall intensity attributed to the low hydrogen- and oxygen-content and to the presence of large clusters of aromatic rings possessing higher translational symmetry compared to the biochars [114]. Translational symmetry is also the basis for the low S/N observed in the Norit RB3 spectrum. Biochars and Norit RB3 exhibit the aromatic ring C=C stretch at 1585 cm^{-1} and associated C-C stretch at ∼1500 cm^{-1}. An intense band between 1350 – 1000 cm^{-1} is attributed to sp^3 C-C and C-N stretch modes, C-H bend modes, and C-O-C stretch modes, which are all characteristic of biochars [46,101]. All materials also show intensity at 960 – 980 cm^{-1} characteristic of the C=C bend of disubstituted alkenes [112]. This characteristic, intense peak is easily visible in the spectrum of Norit RB3, however appears as a weak shoulder in the biochar spectra.

All materials exhibit sp^2 C-H stretch modes at 3050 cm^{-1} and sp^3 C-H stretches at 2918 cm^{-1} and 2848 cm^{-1}, but Norit RB3 shows very low intensity associated with these modes compared to the biochars, consistent with the low hydrogen content of Norit RB3. The pair of intense peaks at 2918 cm^{-1} and 2848 cm^{-1} in all biochars are most likely to correspond to the CH_2

asymmetric and symmetric C-H stretches. The red-shifted frequencies are attributed to attachment to bulkier aromatic rings or hydrogen bonding with neighboring oxygen groups [112]. Weak shoulders at 2967 cm^{-1} and 2890 cm^{-1} are indicative of the C-H stretches of CH_3 and CH groups.

Aromatic ring out of plane C-H deformation modes are observed at varying intensity between 700 – 900 cm^{-1} for all materials. These modes are significant as they indicate patterns of substitutions on aromatic rings [112]. Norit RB3 exhibits a different characteristic substitution pattern compared to biochars, and low overall intensity for these peaks consistent with the low intensity of the sp^2 and sp^3 C-H stretches and more clustering of aromatic rings in that material. The primary peaks in this region for Norit RB3 are between 800 – 825 cm^{-1} indicative of di- and trisubstituted rings. The low intensity is consistent with the increased ring clustering. Biochars, on the other hand exhibit very intense bands in this region associated with one to four substitutions, consistent with a much lower degree of ring clustering compared to Norit RB3.

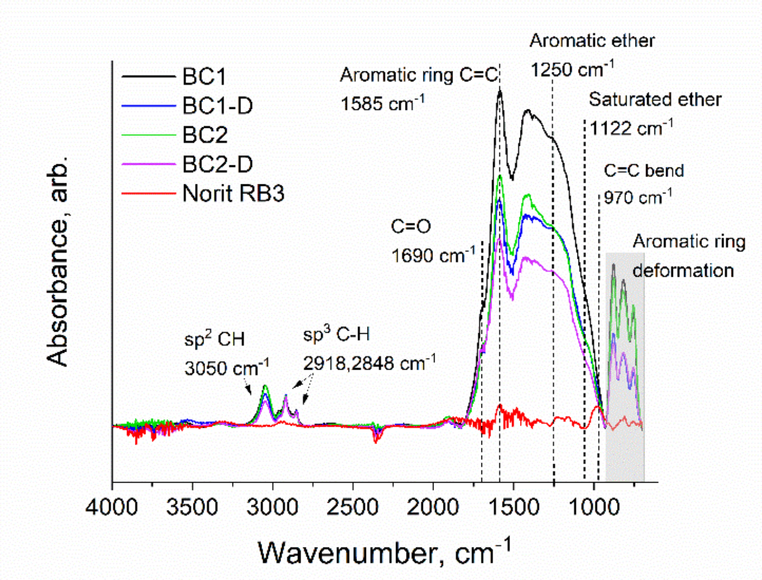

Figure 12: DRIFTS spectra of all materials. All biochars exhibited characteristic intensities due to H- and O-containing functional groups with some apparent differences in intensity of these modes, particularly between

700 – 1500 cm^{-1}. It is of note that the raw absorbance of Norit RB3 was much less intense than that of all biochar samples due to the low H- and O-content as well as the higher degree of clustering of aromatic phases [114]**.**

Intensity in bands associated with oxygenated groups was observed for all materials, and some are annotated in Figure 12. The spectra of biochars indicated the presence of quinone or lactone groups, ether groups, and some evidence for peroxide or epoxide groups. The presence of carboxylic anhydrides cannot be ruled out due to the width of the shoulder at 1690 cm^{-1} extending above 1750 cm^{-1} and the strong intensity in the C-O stretch region around 1050 – 1030 cm^{-1} [112]. For Norit RB3, only some ether and epoxide/peroxide groups appear to be present evidenced by intensity between 1300 – 1000 cm^{-1} [24]. All biochars exhibit a shoulder at 1690 cm^{-1} attributed to a conjugated C=O stretch, for instance quinone or lactone, with the low frequency ruling out the presence of carboxylic acid groups [24,107,112]. Biochars and Norit RB3 show some intensity at ∼1250 cm^{-1} which is attributed to C-O stretch of pyrone structures, and at 1033 cm^{-1} and 1120 cm^{-1}, indicating saturated ether functionalities are present.

Peak-fitting of the complex band between 1700 – 1000 cm^{-1} was not conducted simply due to the complexity of overlapping bands in this region. Some comparative statements can be made, however, based on Raman results and H/C as reported in Tables VIII and IX. First, BC1 and BC2 show lower intensity between 1400 – 1000 cm^{-1} compared to the 1585 cm^{-1} peak than the other biochars. While this is not conclusive, it may be indicative of lower oxygen content in untreated biochars, consistent with reports by others for wood-based biochars. Next, demineralized biochars appear to show lower normalized intensity associated with the C-H and substitution-dependent aromatic ring deformation modes between 900 – 700 cm^{-1}. The high intensity of these modes would indicate reduced clustering of aromatic rings in demineralized materials, however this finding is contrary to the comparative H/C for untreated and demineralized carbons. The basis for this behavior is not elucidated in the DRIFTS spectra due to the semi-quantitative nature of that technique. It is likely to be related to cluster size within these materials. Because the I(D)/I(G) for all biochars was not significantly different, it is proposed that clusters are very small in all biochars and that even a minor increase in cluster size, for instance one ring vs. four rings, may not be detected by the Raman fitting procedure, however could decrease the intensity of those ring deformation modes. Because DRIFTS is not a quantitative technique this question cannot be answered precisely with these data. It is recommended to investigate using transmission IR or other technique.

3.3.3. Textural and Compositional Characterization

Specific surface area calculated using the BET method (S_{BET}) for all materials is reported in Table IX. Norit RB3 has nearly three times the S_{BET} of the demineralized biochars, with similar differences in pore volume. Untreated biochars showed the lowest surface area, which has been observed previously for wood-based biochars [49,51]. Pore volume calculations could not be carried out for BC1 and BC2 due to their very low N_2 adsorption capacity. Their surface area is ascribed to the macroporosity of native plant cellular structure shown in Appendix B. As predicted, demineralization increased the surface area for both BC1 and BC2. BC1-D had ~10% higher S_{BET} than BC2-D.

Moisture and H-content are also reported in Table IX. H/C ratio has been identified as a metric for aromaticity in pyrolytic amorphous carbons [47]. H/C for Norit RB3 is approximately one-third to one-half that of the biochars, indicating much higher aromaticity. Moisture is reported because pre-adsorbed water vapor can impact breakthrough [133,134]. Note that all materials contained some adsorbed atmospheric water despite storing at 75°C for at least 48 hours prior to testing.

Table IX: Textural and compositional properties for biochars and Norit RB3

	Specific Surface Area m^2/g	Pore Volume mL/g	H/C atomic ratio	Moisture, wt%
Norit RB3	1121	0.49	0.12	0.76
BC1	1.0	-	0.40	0.89
BC1-D	427	0.14	0.41	0.77
BC2	1.0	-	0.37	0.92
BC2-D	382	0.16	0.47	0.71

3.3.4. Breakthrough Results and Discussion

Averaged breakthrough curves (after system response subtraction) for three repetitions of each material (~0.5 g of adsorbent per repetition) are shown in Figure 13a,b with ± one standard deviation. Mean breakthrough times with one standard deviation for $C/C_0 = 0.1$ and $C/C_0 = 0.01$ for all materials are reported in Table X. Breakthrough is primarily associated with the onset portion of the curve, so a zoomed in figure showing only the onset region of the curves is shown in Figure 13b. Discussion of trends associated with the inflection point and plateau region presented at the end of this section.

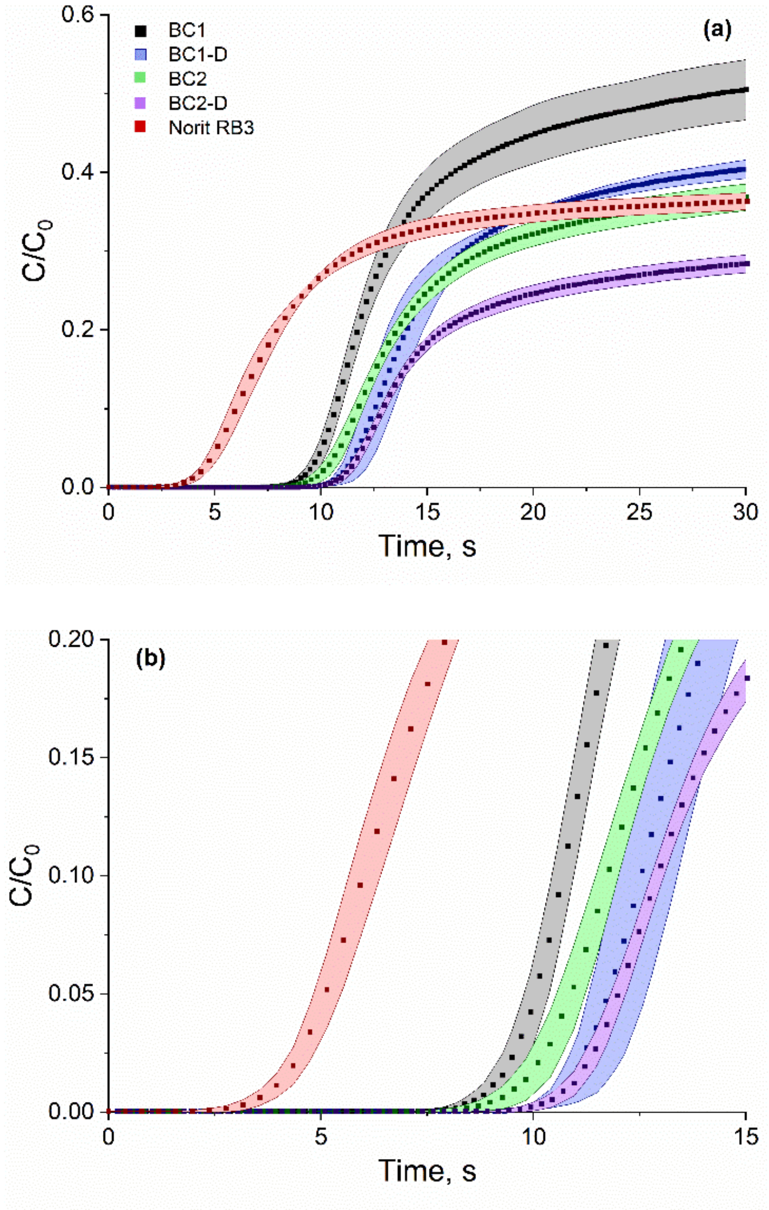

Figure 13: (a) Averaged breakthrough curves with error bands (± σ_s) for all materials. The behavior associated with the plateau region was unaccounted for in this present study, however is likely a combination of system response and role of oxygenated groups and micropore structure [135] **(b) Close-up of the region relevant to breakthrough showing similarity between breakthrough times for all biochars, which are approximately twice that for Norit RB3.**

Table X: Average breakthrough times ± one standard deviation

	Mean Breakthrough Time, s	
	$C/C_0 = 0.10$	$C/C_0 = 0.01$
BC1	10.7 ± 0.3	9.0 ± 0.4
BC1-D	12.6 ± 0.8	11.1 ± 0.6
BC2	11.8 ± 0.3	9.6 ± 0.5
BC2-D	12.9 ± 0.2	10.8 ± 0.3
Norit RB3	6.0 ± 0.4	3.9 ± 0.4

Breakthrough time did not correlate well with S_{BET} when all materials were considered collectively ($R^2 = 0.5345$ and 0.5460 for $C/C_0 = 0.01$ and 0.10, respectively). This relationship is shown graphically in Figure 14a. For instance, S_{BET} of Norit RB3 is approximately 10^3 times that of BC2, but the breakthrough time for Norit RB3 was approximately half that of BC2 at $C/C_0 = 0.10$. However, when only the biochars were considered, breakthrough time showed a very weak positive correlation with S_{BET} at both $C/C_0 = 0.01$ and 0.10 ($R^2 = 0.7540$ and 0.6676, respectively). This relationship is shown in Figure 14b. Because the high surface areas for Norit RB3, BC1-D, and BC2-D are related to microporosity (See isotherms in Appendix B) the weak correlation between S_{BET} and breakthrough time indicates that microporosity associated with high sp^2 carbon content is not responsible for adsorption up to breakthrough time. The more likely scenario is that breakthrough times are governed by diffusion on the outer particle surfaces and in macropores to adsorption sites. In other words, primarily the outer surfaces of the particles contribute to adsorption up to breakthrough times. The very slight increase in breakthrough time for demineralized biochars compared to untreated biochars in Figure 14b supports this scenario.

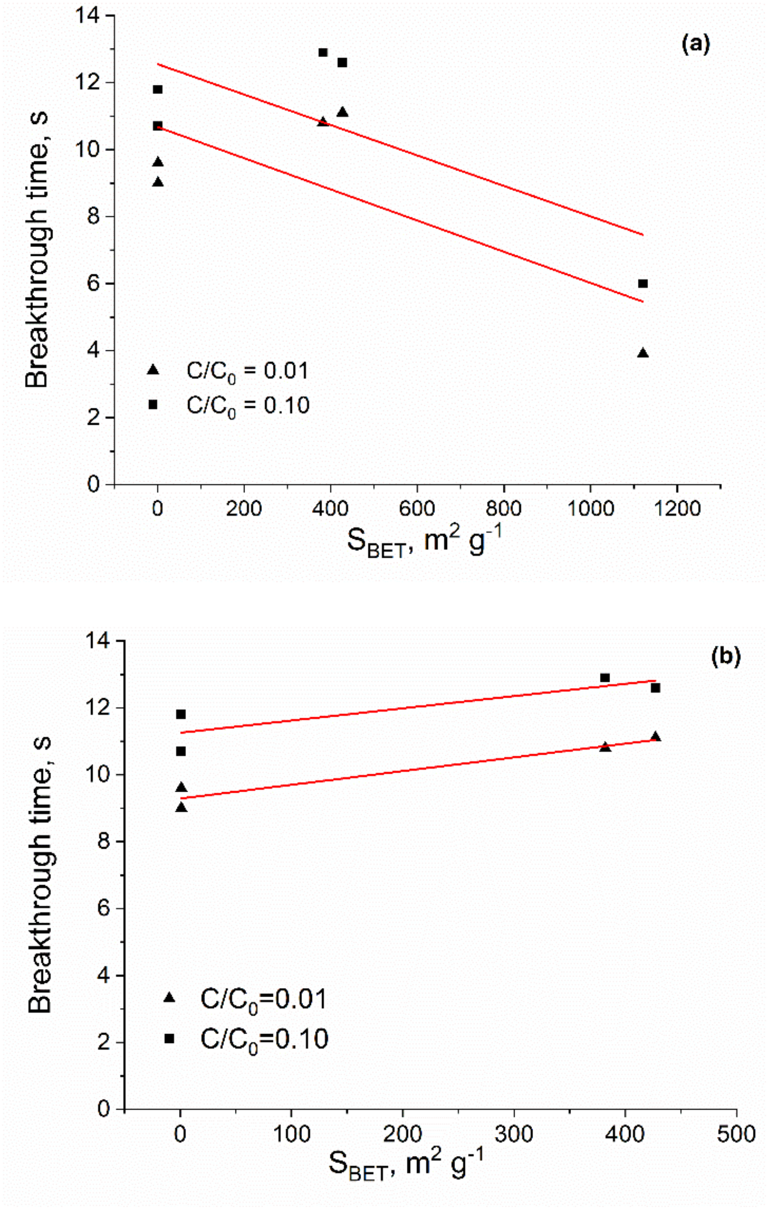

Figure 14: (a) Breakthrough time vs. S_{BET} for all materials at C/C0 = 0.01 and 0.10 (R^2 = 0.5345 and 0.5460 for C/C_0 = 0.01 and 0.10, respectively); (b) Breakthrough time vs. S_{BET} for biochars only (R^2 = 0.7540 and 0.6676 for C/C0 = 0.01 and 0.10, respectively)

The poor correlation with surface area indicates that surface chemistry may be the determining factor for breakthrough behavior, more specifically, the chemistry of outer surfaces and macropores. Lodewyckx and Wood noted that for chemisorption, micropore volume may be less important than chemical interactions between the contaminant and active sites in activated carbons [130]. Additionally, Huang, *et al.* and Domingo-Garcia, *et al.* found that surface area, particularly that associated with micropores, was not the governing factor in determining breakthrough behavior of ammonia on oxidized activated carbons due to the prevalence of acidic oxygen-containing groups at the entrances to micropores [24,73].

Evidence of the presence of surface acid sites is present in the DRIFTS band between 1750 – 1650 cm^{-1} for all biochars, however that band is absent for Norit RB3, indicating carboxylic anhydrides, pyrone, quinone or lactone species on the surface of biochar particles may be involved in adsorption up to breakthrough. These species are likely to be located in sp^3 phases and at the edges of sp^2 clusters, where they are likely to chemisorb ammonia by nucleophilic substitution reactions. In sp^3 phases, they may slow surface diffusion for further ammonia uptake, and at the edges to micropores, they would readily take up ammonia during the initial stages of the dynamic adsorption process, but restrict further access to micropore surface area. Domingo-Garcia, *et al.* observed this latter phenomenon for oxidized activated carbons [73]. For oxygenated species located within pores, access would be limited on short time scales associated with breakthrough.

The competing effects of physisorption and chemisorption may also play a role. Lodewyckx and Wood noted that in the case of chemisorption, W_e and k_v were likely to differ from those same parameters for physisorption [130]. In that same work, they also noted that in comparing values of W_e and k_v for physisorption vs. chemisorption, W_e is the most sensitivity to the type of adsorption, and is also known to have a greater effect on determining breakthrough time than k_v [130,133,134]. In the case of pure physisorption, W_e is dependent on the pore structure and surface area of the adsorbent material, however if physisorption was the governing behavior, breakthrough time should scale with surface area, which was not the case for the materials in this present study [63].

For a typical breakthrough experimentation, the plateau is reached as C/C_0 nears 1. The low C/C_0 associated with the plateau in these experiments is likely to be related to a combination of the following: dead volume response, system response to ammonia adsorption on silica components, the formation of multi-layers of ammonia on surfaces, and slow diffusion kinetics of ammonia in adsorbent particles at long times. Additionally, reaching $C/C_0 = 1$, even with an empty column, took a very long time, possibly related to multi-layer formation of ammonia on the column packing. Only the system response and one biochar experiment were allowed to run beyond 60 seconds to prevent excessive corrosive action by ammonia on the MS unit. Those two curves showed similar behavior at long times, with the plateau region extending approximately linearly to $C/C_0 = 1$. Raw MS ion current curves for a few biochars and Norit RB3 are shown in Appendix B to illustrate this point. Further study, including investigation strength of surface acid sites by titration, is needed to begin addressing those questions.

3.3.5. Application of the Wheeler-Jonas Equation

BC1, BC2-D, and Norit RB3 were used as comparative materials to test the application of the Wheeler-Jonas equation under the given process conditions. These materials were used because they represent the shortest and longest overall breakthrough times (Norit RB3 and BC2-D, respectively), and the shortest breakthrough time for a biochar (BC1), thus providing three comparative breakthrough behaviors by which to test the fit.

Appropriateness of the Wheeler-Jonas model for the breakthrough curves was determined according to the linearization procedure described in Section 3.1.2. Linear fits for breakthrough time vs. bed mass were obtained by regression using three different bed masses, according to Wood and Moyer [129]. For the mass points at 0.5g, the average breakthrough time at C/C_0 = 0.01 and 0.1 for three measurements was used, while for the lower and higher mass data points, ~0.25 g, and ~0.61 g or ~0.75 g, only one measurement was taken due to limitations in adsorbent quantities. C_0 was calculated as 5.8807 x 10^{-9} g/cm^3, the appropriate units for application of the Wheeler-Jonas equation. Bed density was calculated using the mass divided by volume of the bed. This gave 0.1415 g/cm^3 for BC1, 0.1876 g/cm^3 for BC2-D, and 0.2572 g/cm^3 for Norit RB3. Linear fit parameters and calculated W_e, k_v and W_c values according to Eq. (4), (5) and (6) are reported in Table XI. Linear fits for C/C_0 = 0.1 are shown in Figure 15.

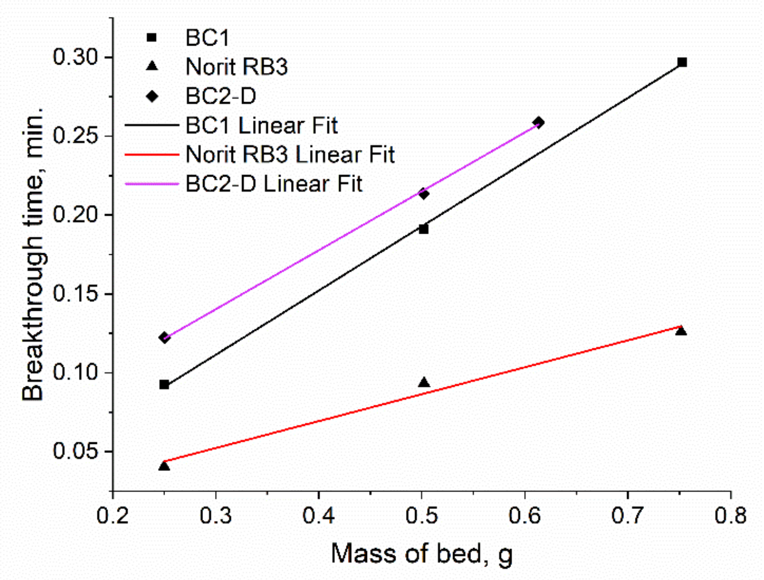

Figure 15: Plot of breakthrough time at C/C_0 = 0.1 vs. mass of adsorbent bed, with linear fits. The linear fit parameters were used to calculate W_e, k_v, and W_c for BC1, BC2-D and Norit RB3 using equations 4, 5, and 3, respectively.

Indicators that the Wheeler-Jonas model is appropriate under the given test conditions include good linear fit, a positive slope and negative y-intercept to give physically meaningful values for W_e and k_v according to Eq. (4) and Eq. (5) [130]. The negative y-intercept produces a positive k_v because, according to the mass-balance for contaminant uptake by the particle, the kinetic term must subtract from the capacity term in Eq. (3) [70,130,136]. For BC1, breakthrough time at $C/C_0 = 0.1$ and $C/C_0 = 0.01$ gave identical values for W_e and k_v within the standard error of the linear fit. The results of this calculation for $C/C_0 = 0.1$ are listed in Table XI. For RB3, the same procedure at $C/C_0 = 0.1$ gave physically meaningful values for W_e and k_v within the standard error of the fit. Physically meaningful values were not achieved for $C/C_0 = 0.01$, as the positive value for y-intercept associated with $C/C_0 = 0.01$ gave a physically meaningless negative value for k_v. A similar result was obtained for BC2-D at both $C/C_0 = 0.1$ and $C/C_0 = 0.01$.

Table XI: Results of linear fit of breakthrough time vs. mass, with calculated W-J parameters for $C/C_0 = 0.10$

	BC1	**BC2-D**	**Norit RB3**
Slope	0.407 ± 0.005	0.374 ± 0.009	0.171 ± 0.022
y-intercept	-0.011 ± 0.009	0.028 ± 0.004	0.001 ± 0.012
R^2	0.9996	0.9994	0.9830
W_e (μg/g)	0.242 ± 0.005	0.220 ± 0.009	0.123 ± 0.022
k_v (min^{-1})	1150 ± 12	-	-
W_c (g)	0.027 ± 0.000	-	-

The reason for the limited application of the linearized Wheeler-Jonas model for extracting k_v for Norit RB3 and BC2-D may be related to the type of correction used to calculate the breakthrough time, to the skewness of the curves, or both. One assumption made in using the Wheeler-Jonas model is that the rate coefficient, k_v, is a first-order, overall rate which can account for all processes up to saturation [130]. For processes which may have significant diffusion limitations, skewness can result in the top portion of the curve having a different slope than the lower portion of the curve [70]. Skewness was observed in the present work and is reflected in the vertical position of the inflection point on the curves. The inflection point of the curve is known as the stoichiometric point because it reflects the second order kinetics in that regime based on equal concentration of contaminant and vacant adsorption sites [70]. The location of the inflection point is related to inlet flow rate and concentration and to the capacity of the adsorbent for ammonia at the temperature of testing. Deviation of this point from $C/C_0 = 0.5$ is common for activated carbons, which can exhibit skewed curves that are steeper at the onset than at the top of the curve due to the slow kinetics of diffusion into micropores [137]. With these factors in mind, the very low C/C_0 for the inflection point for Norit RB3 and BC2-D compared to BC1 would seem to be indicative of very slow kinetics of the dominant processes for C/C_0 above the inflection point. Additionally, all curves exhibit inflection points at similarly low C/C_0 except BC1. It may be theorized that this material does not have the same kinetic restrictions as the other samples. The reason for this is not apparent at this point, however this may be the determining factor in the Wheeler-Jonas model appropriately fitting the breakthrough curve for BC1.

To test the appropriateness of the Wheeler-Jonas model outside of error due to system response correction (discussed in Section 3.3.4), values for slope and y-intercept were chosen to force the fit for BC2-D and Norit RB3. A slope slightly steeper than that for BC1 was selected to account for the longer breakthrough time and lower inflection point, for instance 0.47 min. g^{-1}. Then, a value for k_v which reflected the shape of the curve up to the breakthrough point was selected. For BC2-D, this procedure resulted in $W_e = 0.276$ µg/g, and k_v of approximately 750 min^{-1}. This curve is labelled in Figure 16 as the Test Fit. For Norit RB3, the values from Table XI for W_e was used and k_v was calculated within standard error of the y-intercept measurement.

This gave k_v = 1630 min^{-1}. The curve created using these values is labelled as Linearization Fit in Figure 16. That fit did not capture the shape of the onset curve and over-estimated the breakthrough times at C/C_0 = 0.10 and 0.01. When a slower rate coefficient was used with this same capacity term, for instance 500 min^{-1}, the fit was more representative of the onset of the Norit RB3 breakthrough curve and is labelled as the Test Fit in Figure 16. The fit for BC1 resulting from the linearization procedure summarized in Table XI is also shown in Figure 16 and is labelled as the Linearization Fit. These results indicate that for Norit RB3 the linearized calculation of W_e and k_v overestimated breakthrough time for C/C_0 = 0.01 and 0.10. It is proposed that more appropriate values for W_e and k_v, hence W_c would give a better fit. For BC1 the fit was within experimental error to C/C_0 = 0.06, but underestimated breakthrough time for C/C_0 = 0.10, indicating the model may only be appropriate for C/C < 0.06.

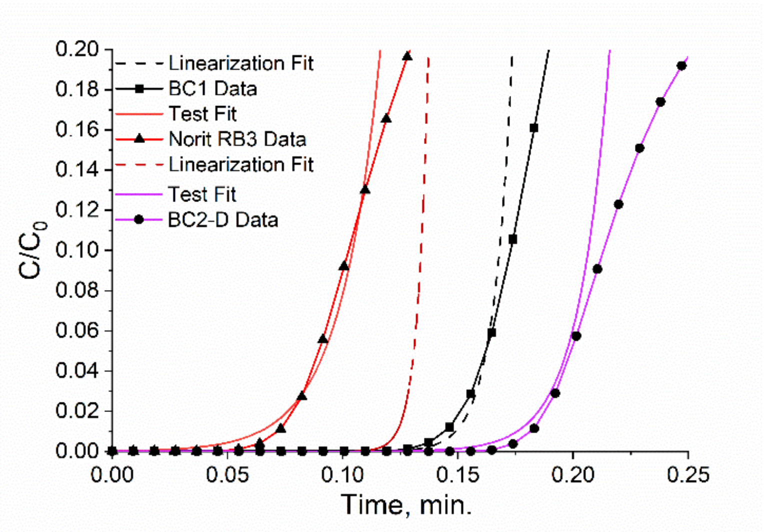

Figure 16: Averaged breakthrough curves (line + symbol) for BC1, BC2-D and Norit RB3 with Wheeler-Jonas model curves calculated using W_e and k_v from Table XI (dashed lines) and test fits according to the discussion in Section 3.3.5 (solid lines) illustrating that the Wheeler-Jonas model had variable success in predicting the shape of the breakthrough curves. A linearization fit was not available for BC2-D, so only the test fit is shown.

3.3.6. Experimental Sources of Error

The primary source of experimental error was attributed to very small particle size enhancing variation in density of the adsorbent bed due to settling. For small particles, increased bed density can significantly reduce the void space in the bed, increasing the local flow rate around the particles, thus resulting in an apparent higher Q in Eq. (2-6), with the greatest effect being an underestimation of W_e. All experiments were run at ambient temperature, which is known to fluctuate in that location by ±2.5°C throughout the day. The impact of this fluctuation is likely to be minimal. In terms of moisture effects, Lodewyckx noted that even for dynamic adsorption of organic molecules on activated carbon, the validity of the Wheeler-Jonas equation is limited to dry conditions, and that humidity strongly affects both k_v and W_e [133,134]. The impacts of pre-adsorbed water and humidity in the flow stream were minimized by drying the materials ahead of time and using ultra high purity bottled gases. Moisture content in Table IX did not correlate with breakthrough times for any of the materials. Slight inconsistencies in mass of column packing material was determined to be an additional source of error resulting in variation in breakthrough time among repetitions for each material type. Correlation between breakthrough time and mass of column packing is shown in Appendix B. Error in fitting the Wheeler-Jonas model to experimental data was not quantified, but may have some roots in the correction used. Further testing is recommended for the biochar/ammonia system to find an appropriate correction and minimize this source of error.

3.4. Conclusions

The primary goal of this work was to investigate how surface area and oxygen content of biochars impact the dynamic adsorption behavior for ammonia. The biochars used in this study demonstrated varying textural and chemical properties, and all showed longer breakthrough times than the commercial activated carbon, which had nearly four times higher apparent surface area measured as S_{BET}. Correlation between breakthrough time and oxygenated functional groups was inconclusive. From these results it is concluded that the outer surfaces of particles including macropores are responsible for ammonia adsorption up to C/C_0 relevant to breakthrough times. Finally, we propose that the further testing is needed to determine the appropriateness of the Wheeler-Jonas equation for biochar and activated carbon under test conditions similar to those used in this study, including reasonably high challenge concentration and low flow rate. $C/C_0 = 0.06$ appears to represent the upper concentration limit for its use under the process conditions used in this study. Further testing with larger particles and different process conditions, i.e. flow rate and C_0 are recommended to determine the impacts of these variables on the breakthrough time and the shape of the breakthrough curve, particularly the degree of skewness.

4. Unique Chemistry and Structure of Pyrolyzed Bovine Bone for Enhanced Aqueous Metals Adsorption[3]

4.1. Introduction

Beginning in the early 19th century, bone char, made of pyrolyzed animal bone waste, was valued for its unique capacity in simultaneously removing colorants and ash from sugar liquor, with performance in this application attributed solely to the mineral phase - a biogenic, highly defected, carbonated apatite [1–3]. Shipping restrictions during World War II resulted in a shortage of foreign-supplied raw bone feedstock to supply the booming U.S. sugar industry, fueling a search for promising replacement materials [1]. Synthetic calcium phosphate hydroxyapatite, $Ca_{10}(PO_4)_6(OH)_2$, is structurally and chemically similar to bone mineral, and was investigated as a high performing, affordable replacement. In this early research, direct comparative studies showed that bone char removed more ash and colorants when normalized for surface area and imparted a slightly higher pH to liquors than synthetic hydroxyapatite indicating differences in surface chemistry and reactivity between the two [1].

The adsorptive properties of bone char have been tested in a range of other, primarily aqueous, contaminant removal applications, including municipal water treatment – although in this case the taste imparted into the water was unpalatable resulting in bone char being abandoned in favor of other methods [4]. More recently, bone char has demonstrated high potential as an inexpensive, effective adsorbent for treating mine, industrial and municipal waste water laden with heavy metals or fluoride [5–8]. Structurally and chemically similar synthetic hydroxyapatite has also been applied in toxic metals and fluoride remediation, but comparative

---

[3] Muretta, J.E., Prieto-Centurion, D., LaDouceur, R., Kirtley, J.D. Waste and Biomass Valorization. 2022. *Manuscript Under Revision*

studies of the relative performance of bone mineral and hydroxyapatite in these applications are largely absent from recent literature [9–14].

One exception is a study by Hashimoto, *et al.* in which the effects of crystallinity on lead adsorption were investigated [11]. In that study, poorly crystalline, gypsum-derived hydroxyapatite and poultry bone mineral were more effective in removing lead from water than highly crystalline hydroxyapatite over a wide pH range. These findings support the early results of Barrett, Joyner, and Halenda regarding the superior performance of bone char in sugar purification and seem to indicate that the inherent disorder in natural bone mineral is beneficial for aqueous metals remediation applications [1,2,15]. In another notable study supporting similar conclusions, Betts, *et al.* briefly discuss carbonate content in bone apatite as a source of disorder which enhances dissolution of bone mineral in Zn^{2+} solution, resulting in high Zn^{2+} removal by precipitation of less soluble zinc phosphate [5].

These past studies as well as in-house investigations into Cu^{2+} uptake from $Cu(NO_3)_2$ aqueous solution raised questions regarding 1) the impacts of the chemistry and nanostructure of pyrolyzed bone mineral compared to those of synthetic carbonated hydroxyapatite, and 2) the role of the residual nitrogen-rich carbonaceous phase on Cu^{2+} removal [16]. It is clear that a more detailed understanding of bone char and comparative carbonated hydroxyapatite used in aqueous metals removal applications is needed in order to optimize their performance for toxic metals remediation. The specific aims of this present study were to identify features unique to bone char which could be related to metals removal processes like cation exchange, coprecipitation, and dissolution/precipitation. Particular attention was paid to factors which are known to play a strong role in disorder and enhanced surface activity of the mineral phase like polyanion substitutional type and level (particularly carbonate substitutions), the formation of non-apatite phases, and functional groups of the carbonaceous phase which are known to have a particularly high affinity for Cu^{2+}.

4.2. Materials and Methods

4.2.1. Sample Preparation

Samples used in this present study are summarized in Table XII. The preparation of pyrolyzed bone was reported elsewhere, but briefly, bovine femurs were boiled to remove residual soft matter and fats, broken into 1-inch pieces, granulated, dried at 90°C for >48 hours before further grinding into powder containing heterogeneous size fractions [16]. This sample is hereafter referred to as RGB. The as-prepared RGB was heated at ~15°C/min. to 750°C (30 min. dwell) in a tube furnace (MTI, OTF-1200X) with 60 mm x 60 cm quartz tube under flowing argon (3.0 L/min.). This pyrolyzed sample is hereafter referred to as BC750. Synthetic carbonated hydroxyapatite (Sigma Aldrich), hereafter called CHAp, was used as a comparative material for the mineral phase of BC750. It was used as-received without further processing.

Three additional samples were prepared to provide insight into the substitutional polyanion environments and the effects of pyrolysis on the mineral and organic components of bone. First, a small amount of CHAp was pyrolyzed according to the same method described above for BC750. This sample is labelled CHAp750. To isolate the carbonaceous component of BC750, a small amount was demineralized in 5M HCl, followed by copious rinsing with deionized (DI) water and drying at 75°C for 12 hours. A slight tint to the filtrate suggested that some soluble carbon was lost during the leaching process. However, since this carbon represented a trace amount of the total mass of solids, the remaining powder was assumed to represent the carbonaceous phase for the intended purpose. This sample is labelled D-BC750. The third sample is a wood-based biochar prepared from ground black cottonwood pyrolyzed in argon to 700°C. This sample is referred to as biochar. The highest treatment temperature (HTT) difference (700 °C vs. 750°C) was considered negligible compared to the effects of feedstock differences between bone char and biochar. This biochar was used to compare general functional group chemistries and carbon hybridization states between bone char and biochar. Comparison between pyrolyzed and un-pyrolyzed samples is denoted in this work as X → Y, with the arrow indicating pyrolysis.

Table XII: Sample information and specific surface area measured by N_2 adsorption

Sample	Description	Preparation	Properties
RGB	Raw, ground bovine femur, powdered	soft matter removed, boiled, dried, ground	
BC750	Pyrolyzed RGB	Pyrolysis in flowing Ar: 3L/min flow rate, 15°C/min to 750°C, 30 min dwell	S_{BET} = 112 m^2/g, mesoporous
CHAp	Synthetic carbonated hydroxyapatite	As-received; Sigma Aldrich, 10 µm, ≥100 m^2/g	S_{BET} = 113 m^2/g, mesoporous
CHAp750	Pyrolyzed CHAp	Pyrolysis in flowing Ar: 3L/min flow rate, 15°C/min to 750°C, 30 min dwell	
D-BC750	Demineralized BC750	Leaching in 5M HCl followed by filtration and copious rinsing with DI water	
Biochar	Wood-based biochar	Pyrolysis in flowing Ar: 3L/min flow rate, 15°C/min to 700°C, 5 min dwell	

4.2.2. Characterization Methods

Secondary electron micrographs of all samples were taken on a Mira 3 Tescan field emission scanning electron microscope.

Powder x-ray diffraction was performed for mineralogical phase determination and to investigate the effects of heating on lattice parameters and crystallinity. Measurements were made for powdered samples without further preparation on a Rigaku Ultima IV X-ray

Diffractometer using Cu k-alpha 1 radiation (1.54059 Å) at -40kV and 40mA with a Ni k-beta filter. Scans were taken in Bragg-Brentano geometry between 5° – 70° 2θ with step size of 0.02°.

Specific surface area (SSA) and pore size distribution (PSD) analysis were outsourced to Dynalene Laboratory Services. SSA and PSD were extracted from N_2 adsorption-desorption isotherms collected at 77K using a Micromeritics ASAP 2020 apparatus. SSA for each sample were calculated from the adsorption branch using the Brunauer-Emmett-Teller (BET) equation and pore size distribution from the desorption branch using Density Function Theory (DFT) methods [17]. Prior to measurement, all samples were degassed at 0.667 Pa and 200°C for at least 8 hours.

Diffuse Reflectance Fourier Transform Infrared spectra (DRIFTS) were collected to characterize mineral and carbonaceous phases. All data were taken on a Shimadzu IR Tracer100 (Shimadzu Corp.) with Praying Mantis DRIFTS attachment (Harrick, Inc.) and DLTAGS detector under ambient conditions with atmospheric correction applied. Samples were prepared for DRIFTS by grinding individual powdered samples (~7% wt./wt.) in KBr powder using a mortar and pestle. References collected from pure KBr were used to remove backgrounds from all sample spectra. Spectra were collected in the 4000 – 400 cm^{-1} range at 2 cm^{-1} resolution with 120 accumulations. At least three samples from each material were tested. Second derivatives of each raw spectrum were mathematically calculated using Origin Pro (OriginLab, Corp.), and were used to identify peak locations and therefore guide peak fitting with the appropriate number of Gaussian curves in the $v2$ CO_3^{2-} band between 820 – 920 cm^{-1}. Spectra were cropped between 820 – 920 cm^{-1}, and a linear background was applied and subtracted prior to fitting. Statistical analysis was conducted for all fit results for three different spectra (n = 3) each of unpyrolyzed and pyrolyzed material using single-tailed paired t-tests on the difference of the means at the $p < 0.05$ level.

Raman measurements of undiluted, powdered samples were made on a Renishaw Spectrometer using a 20x LWD objective. Because strong photoluminescence of the mineral phase was observed with longer wavelengths, the 457 nm emission line from an argon ion laser was chosen with a power of 30 μW power and 1 – 5 µm spot size. Scans were taken between 500 – 2300 cm^{-1} with 3-5 second accumulation time and 5 – 20 repetitions in order to achieve sufficient signal/noise. Low power density is often necessary to prevent thermal damage to opaque samples such as amorphous carbon. For each sample, 3 – 5 randomly chosen spots were analyzed to ensure uniformity. Reported fit parameters are the arithmetic mean for these scans with reported standard error. Paired t-test and standard t-test were used to determine statistical significance at the $p < 0.05$ level on the differences in mean peak parameters for BC750 and D-BC750 and for D-BC750 and biochar, respectively.

Thermal analysis of all materials was accomplished using thermal gravimetry coupled with mass spectrometry (TGA-MS) for semi-quantitative assessment of the composition and thermal decomposition products for each material. As-prepared samples were heated in ultra-high purity argon or oxygen in the evolved gas analysis furnace (EGA) furnace on a TA Instruments Q500 thermal analyzer (TA Instruments, Inc.). Ion current for m/z of particular ionized species were measured using a Pfeiffer ThermoStar electron impact quadrupole mass spectrometer (Pfeiffer Vacuum GmbH). For these measurements, the MS probe was coupled with the EGA furnace via special attachment (TA Instruments, Inc.) so that the quartz capillary sampled evolved gases directly above the Pt sample pan inside the TGA furnace. For this set of measurements, all samples were initially heated to 35°C and held at that temperature for 1 hour to stabilize the ion current signal, and then heated at 2°C/min from 35°C to 1000°C. Water, hydrogen, carbon dioxide and a characteristic polymer fragment were tracked from all materials, as applicable. All materials were heated in dry argon to measure water content and thermal decomposition. Ash content (mineral phase relative composition) was determined as the residual mass at 600°C in 90% O_2 (bal. Ar). Integration of the smoothed differential weight loss curves was used to calculate water (weight loss between 35 - 150°C), thermal decomposition (weight loss between 150 - 800°C) and residual carbon or ash, which was characterized as the remaining mass at 800°C for runs in argon (D-BC750) and 600°C for runs in oxygen, respectively.

4.3. Results and Discussion

4.3.1. Characterization of Whole Particles

4.3.1.1. Scanning Electron Microscopy

The morphology of BC750 and CHAp particles were investigated using field emission scanning electron microscopy (FE-SEM). Micrographs of BC750 and CHAp at different magnification are shown in Figure 17a-d. Both were found to consist of polydisperse particle size fractions. CHAp particles were spherical in general with larger particles present as hollow spheres, consistent with synthetic hydroxyapatites prepared by aerosol spray method [18]. BC750 particles are oblong and have a heterogeneous size distribution, with the largest typically being <1 mm in the longest dimension. In BC750, mineral platelets are observed in fractured particles (Figure 17).

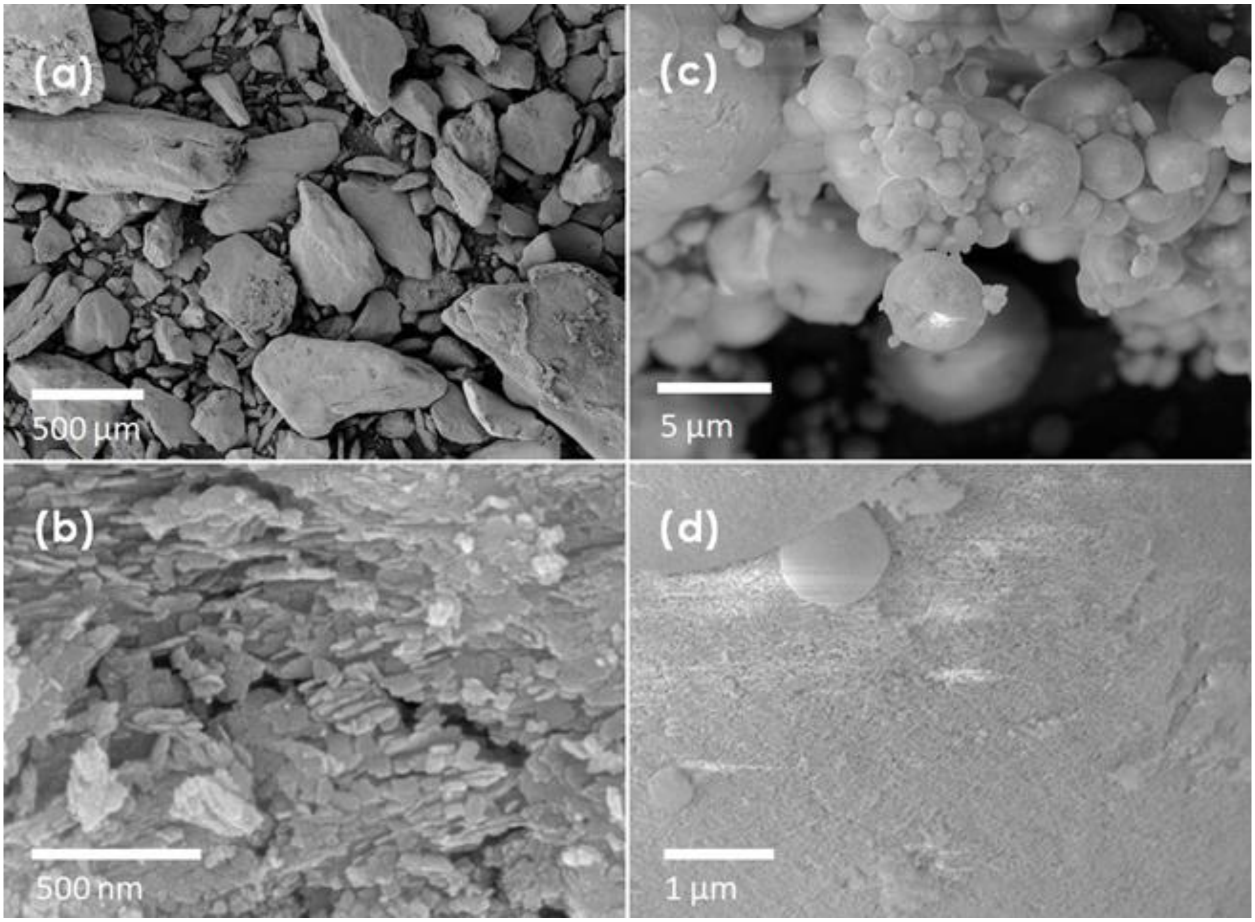

Figure 17: FE-SEM micrographs of (a) BC750 particles have elongated, irregular shape and heterogeneous size distribution; (b) Broken BC750 particle reveals the interior consisting of carbonaceous residue and plate-like mineral components; (c) CHAp particles are polycrystalline spherical or hollow spheres as is typical for aerosol-formed synthetic hydroxyapatite (Vallet-Regi, 2004), and have overall a smaller average size than BC750 particles; (d) CHAp surface showing fine grained, mesoporous structure; it is difficult to determine whether CHAp crystals have columnar or plate-like growth habit.

4.3.1.2. Nitrogen Adsorption

BC750 and CHAp showed similar surface areas calculated using the BET method – CHAp: 113 m2/g, BC750: 112 m2/g. Graphical results are summarized in Appendix C. Both CHAp and BC750 were found to be primarily mesoporous, exhibiting IUPAC Type IV N_2 adsorption/desorption isotherms with H1 hysteresis (Appendix C) [17]. The incremental surface areas for CHAp and BC750 are also presented in Appendix C. CHAp has greater surface area associated with pores larger than 100 Å in diameter, while BC750 has a greater amount of surface area associated with pores between 20 – 100 Å. Microporosity in these two materials was also observed to have different size distributions. CHAp has microporosity of ~7 Å, while BC750 microporosity is slightly larger at ~15 Å.

4.3.1.3. Thermal Analysis and Mass Spectrometry

Thermal degradation products correlated to a particular temperature or range of temperatures can provide clues about composition and bonding in complex materials like bone char. Using TGA-MS, thermally-induced chemical changes can then be correlated to the temperature range over which they occurred and related to the weight lost over that range. In this current work, TGA-MS was used to investigate bulk compositional components like surface adsorbed water and relative amounts of carbonaceous and mineral phases. Mass spectra also provided some sample-specific information, particularly giving insight into bonding in the amorphous carbon of bone char and demineralized bone char as well as the high-temperature decomposition behavior of CHAp. Evolution of water, carbon dioxide, hydrogen, and a characteristic polymer fragment, C_3H_6, associated with volatilization of light hydrocarbons, were tracked to investigate the products of thermal decomposition (argon) and combustion (90% O_2/bal. argon). TGA and DTB curves for BC750, CHAp, and D-BC750 are presented in Appendix C. All samples showed between 2 – 5% by weight physisorbed water loss between 80 – 150°C with residual water and CO_2 evolving at varying quantities up to ~450°C, especially for CHAp.

Using combustion analysis (in 90% O_2/bal. argon), BC750 was found to consist of 2.5% water, 86% ash (mineral phase), and 11.5% carbonaceous phase by weight. In argon, D-BC750 consisted of 1.4% surface adsorbed water, <0.5% ash, and 81% thermally stable carbon while 17% mass loss occurred to thermal decomposition between 80 - 150°C.

For all samples in Ar, water and carbon dioxide generated between 80 - 250°C are attributed to surface adsorbed species [19]. Between 250 - 450°C evolution of these species is attributed to those more strongly adsorbed in pores (i.e. in CHAp). For BC750 and C-BC750, evolution of CO_2 beginning at ~200°C for BC750 and ~400°C in D-BC750 may be indicative of the catalytic action of the mineral phase, present in BC750, lowering the activation energy for CO_2-forming reactions. Above 650°C significant effusion of water and CO_2 was observed for CHAp (Figure 18, top), indicative of the onset of thermal degradation of some carbonate and hydroxyl species, as observed by others [19,20]. High temperature decomposition of bone mineral was not directly observed in this study because effusion of CO_2 and water associated with pyrolysis of the carbonaceous phase obscured the onset of bone mineral decomposition. Thermal decomposition (in Ar) of amorphous carbon in D-BC750 (Figure 18, bottom) resulted in effusion of water, CO_2, and C_3H_6 between 150 - 400°C attributed to volatile, surface adsorbed species, while formation of CO_2 and polymeric fragments between 450 - 800°C are attributed to thermal decomposition of the carbonaceous phase. CO_2 effusion above 450°C is attributed to decomposition of carboxylic anhydride, lactone, and pyrone groups [21]. Water effusion above 600°C is attributed to result from break-down of phenolic alcohols [21]. Hydrogen effusion begins at approximately 600°C, behavior which was previously observed in acetylene-based amorphous carbon films [22]. Hydrogen evolution above 900°C is attributed to carbonization-induced hydrogen release.

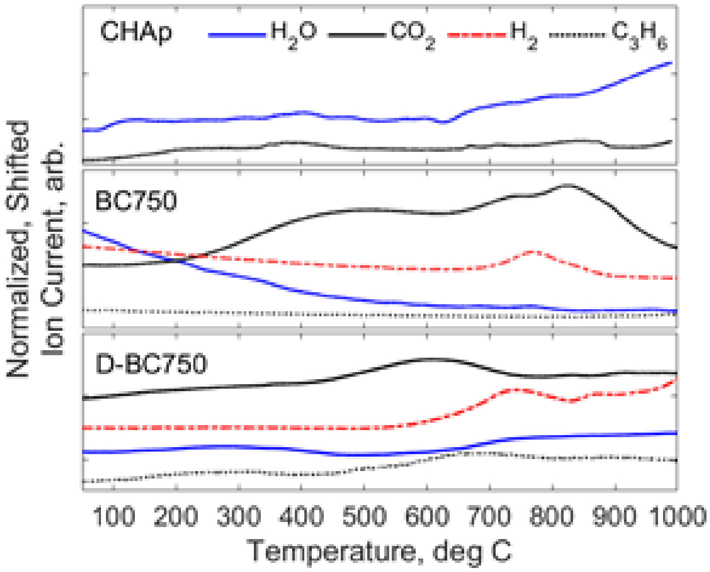

Figure 18: Effusing gases from CHAp (top), BC750 (middle), and D-BC750 (bottom). All signals were normalized to the argon signal and by their respective min-max., H_2 and H_2O curves for BC750 and D-BC750 were multiplied by 5 to improve visibility, and all were vertically offset. The intense background at the start of the H_2O curve for BC750 is attributed to the effects of normalization.

It is worth noting that the temperature profiles for evolved gases from D-BC750 decomposition are consistent with those observed by others [22,23]. Hydrogen evolution has been reported as an indicator of sp^3 structure in amorphous carbon, with H_2 effusion resulting from carbonization processes [22]. Hydrogen, water, and polymer fragment effusion during annealing of amorphous carbon films was studied by Conway, *et al.* [22], with differences in the onset of H_2 effusion attributed to the formation of different hydrogen environments within the amorphous carbon having either methane or acetylene precursors. Conway, *et al.* found that effusion of H_2 at high temperatures was indicative of a dense carbon skeleton of mostly tetrahedrally coordinated sp^3 carbon having a lower overall hydrogen content compared to polymeric amorphous carbon. Fragmentation of polymeric structures was observed to occur just before hydrogen effusion for acetylene-based carbon films, and at the same time as hydrogen effusion from methane-based films. The latter was observed in D-BC750, providing some evidence for the presence of dense, mechanically robust and chemically inert tetrahedrally coordinated sp^3 carbon which may not have sufficient porosity for adsorption of hydrated metal cations, but which give hardness and mechanical stability to the carbonaceous phase. Further study is needed to validate this observation, and to determine whether it is inhibitive to metals removal.

4.3.2. Characterization of Mineral Phases

For the remainder of this current work, results and discussion pertaining exclusively to the carbonaceous and mineral phases of each material is presented separately, with characterization of bone mineral and CHAp presented first and characterization of the carbonaceous phase and biochar last.

4.3.2.1. Review of the Chemistry and Structure of Bone Mineral

The inorganic phase in bone is structurally similar to calcium phosphate hydroxyapatite ($Ca_{10}(PO_4)_6(OH)_2$) sharing the same hexagonal unit cell, with $P6\,3/m$ space group symmetry, lattice parameters a and b being coplanar and c being normal to this plane [24]. In bone mineral, plate-like nanocrystallinity (~50 nm x 25 nm x 4-6 nm) of primary crystallites implies, geometrically, a very high percentage of ionic species are on the surface. In general, surface species are less likely to be charge compensated, and therefore are more likely to be chemically active in processes of metals removal. In addition to surface effects, the presence of substitutional defects in the bulk of bone mineral is likely to extend this solubility behavior in aqueous environments to the whole crystallite [18,25].

Primary crystallites in bone exist as part of a larger mineral macrostructure rather than as isolated crystallites in a bulk collagen matrix. Within this larger macrostructure, individual nanocrystalline apatite platelets are joined by hydrated, interfacial surface structures consisting of amorphous phases of Ca^{2+}, HPO_4^{2-}, HCO_3^-, Mg^{2+}, water, and organic polyanions such as citrate [26,27]. Water in these layers is believed to take on a structural role, orienting the organic polyanions into a distinct, non-apatite phase [28]. The presence of structural water in these phases is also linked to the arrangement of bone crystallites in an oriented, stacked configuration [28]. The close proximity between layers of ordered and amorphous phases implies some interaction may occur during thermal treatment, for instance precipitation of amorphous phases on the surface of primary crystallites or possible incorporation of interlaminar species into primary crystallites. The fate of interlaminar species during pyrolysis has not been well-characterized, but it can be reasoned that these regions are particularly affected by pyrolytic processes including dehydration and thermally-driven, secondary reactions between constituent species. Phase transformation within interlaminar layers is thus possible during heat treatment, with nucleation of new apatite or non-apatite species - probably on the surface of existing primary crystallites.

While often referred to as “hydroxyapatite”, bone mineral is known to be chemically quite different from pure hydroxyapatite [25,29]. First, bone mineral has very little hydroxyl ion content, with so-called structural water occupying most of the hydroxyl sites and some other lattice positions via substitution, and OH^- being found extensively only in mature crystallites [25,30]. Low hydroxyl content in bone mineral has been linked to high susceptibility for dissolution and low acid-buffering capability which enables resorption by osteoclasts *in vivo* [29]. Other differences include ionic substitution and vacancies. Important cation substitutions occur in bone mineral in which primarily Mg^{2+} and Na^+ replace Ca^{2+}. Na^+ substitutions are known to be extensive in biogenic apatite and to occur in conjunction with CO_3^{2-} substitutions in the OH^- position in bone mineral [32].

One important substitutional species, carbonate (CO_3^{2-}), is typically present in bone mineral at about 4-8% wt., and is critical for biocompatibility in synthetic hydroxyapatites for bone implants [29,33]. Carbonate can be present in different forms in both synthetic and biogenic apatite, and within the hydroxyapatite lattice can occupy two primary positions: the OH^- site (also called the channel site; the channel is oriented parallel to the c-axis), which is known as A-type substitution, and the PO_4^{3-} site, known as B-type substitution [31,34]. In A-type substitutions the planar carbonate ion orients normal to the channel axis, having the effect of contracting the c-lattice parameter. In B-type substitutions, the planar CO_3^{2-} ion is believed to primarily occupy the position of one of the faces of the PO_4^{3-} tetrahedra roughly parallel to the c-axis, and has the general effect of contracting the a-axis [33]. Bone mineral is AB-type, containing both types of substitutions, with the degree of A-type substitution observed to depend on the age and species of the bone tissue [34]. Increased CO_3^{2-} content in bone apatite has been linked to reduction in crystallinity and to the plate-like habit and nanometer-scale of primary crystallites, which impart high biological activity, including ease of resorption *in vivo* [25,29,35,36]. Importantly for the current work, A-type substitutions have been observed to reduce the crystallinity of apatite more than B-type [33]. Both bone mineral and hydroxyapatite can also contain a labile (L-type) carbonate species and HCO_3^-, which are typically present in amorphous phases and on the surface of crystallites [32]. Rey, *et al*. indicated that this species may be associated with early stages of apatite crystal formation and with disordered domains [34]. Fleet, *et al.* also referred to L-type CO_3^{2-} as “stuffed channel” CO_3^{2-}, suspecting that it occupies a different orientation within the channel compared to A-type carbonate [37]. Those authors found that in Na-bearing apatite such as bone mineral, L-type carbonate largely disappears with heat treatment above 600°C.

Acid phosphate is another polyanion impurity which is frequently found in both biogenic apatite and synthetic hydroxyapatite. Most HPO_4^{2-} in bone mineral is found within the interlaminar domains, outside the primary crystallites [38]. However, HPO_4^{2-} has been observed within the primary crystal lattice in the phosphate position in smaller amounts and its presence there is believed to relate to charge neutrality. This species is present in synthetic hydroxyapatite as a result of incomplete reaction synthesis. Alternate phases found in thermally treated bone and hydroxyapatite can also contain HPO_4^{2-}, especially octacalcium phosphate (OCP) and brushite [19,39,40].

4.3.2.2. Diffuse Reflectance Fourier Transform Infrared Spectroscopy

Collagen, amorphous carbon, bone mineral and hydroxyapatite all have components with strong IR absorbance, making infrared spectroscopy a powerful and well-used tool for characterizing bone, bone char and hydroxyapatite. In this present work DRIFTS was utilized because of the ease of sample preparation and sensitivity to surface species. The assignment of IR vibrational modes for biological and synthetic apatite have been reviewed extensively elsewhere, and many are labelled in Figure 19a,b [32–34,37,41–43]

The vibrational modes of phosphate, carbonate, and hydroxyl ions are highly sensitive to the local environment, including protonation, making small changes in lattice position or bonding easily detectable with IR spectroscopy. In the present work, OH^- stretch (4000 – 2700 cm^{-1}), $v2$ CO_3^{2-} (~875 cm^{-1}) and $v3$ PO_4^{3-} (1200 – 900 cm^{-1}) modes were used to track differences in anion content which may be relevant to aqueous metals removal application. Representative spectra from each material are presented in Figure 19 a,b.

In materials such as bone mineral, which can contain multiple substitutional species like CO_3^{2-}, HPO_4^{2-}, and so-called structural water, the challenges associated with identifying structural effects due to a single species are non-trivial. IR spectroscopy can provide clues about the fate of substitutional species by probing the degree of protonation, substitutional position, and the formation of alternate phases. It is worth noting that the quantitative capability afforded by the Beer-Lambert law, used for interpretation of transmission IR spectra, does not directly apply to DRIFTS spectra because the optical path and processes involving multiple reflections through the sample are difficult to reproduce. For this reason, DRIFTS results were interpreted qualitatively.

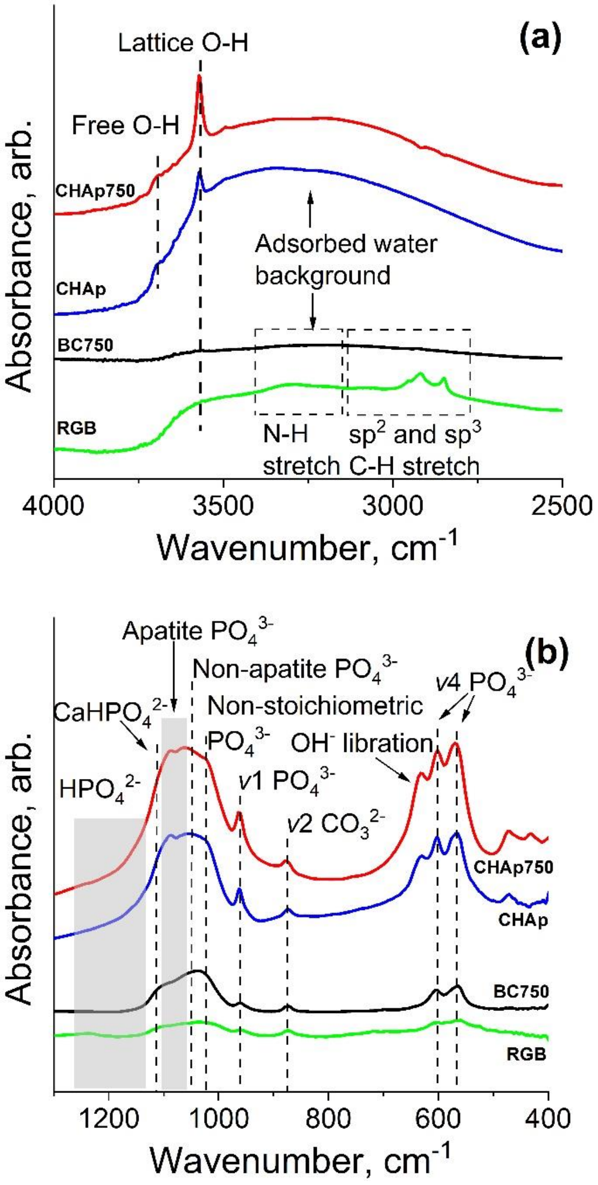

Figure 19: Raw, vertically offset DRIFTS spectra for RGB, BC750, CHAp, and CHAp750. (a) OH, NH, and CH stretch region; (b) *v*1,*v*3 PO_4^{3-}, *v*2 CO_3^{2-} and *v*4 PO_4^{3-} regions with OH^- libration mode. Important vibrational modes are annotated. Overall intensity for mineral peaks in synthetic CHAp and CHAp750 was higher than for RGB and BC750, which may be due to the impact of carbonaceous char and collagen on reflectance and is not a direct function of concentration. All species were mixed with KBr at ~7% wt.

4.3.2.2.1. OH^- and Water Bands

Key differences in OH^- - and water-related bands are visible in the O-H stretch region between 2700 – 4000 cm^{-1} (Figure 19a) and in the O-H libration mode at 630 cm^{-1} (Figure 19b).

The libration mode is associated with lattice species and not metal hydroxides or water. CHAp and CHAp750 have an intense lattice O-H stretch peak at 3570 cm^{-1} and libration mode peak at 630 cm^{-1}, while RGB and BC750 do not show a libration mode and very low to no intensity for the lattice OH$^-$ stretch. This result agrees with the very low lattice OH$^-$ content in biogenic apatite. With pyrolysis, lattice OH$^-$ modes do not appear for BC750, indicating very little to no lattice OH$^-$ is created during pyrolytic processes. A broad, intense band associated with surface adsorption of atmospheric water is observed for all materials, however heated samples show lower intensity for this band compared to un-heated precursors. Lower intensity of the water background is attributed to the effects of pyrolysis where 1) at least partial coating of bone mineral by the more hydrophobic carbonaceous product of collagen pyrolysis was formed, 2) excess surface water was lost, and 3) enhanced crystallinity (including loss of specific surface area), which has been observed in bone mineral to inhibit atmospheric water binding [28].

4.3.2.2.2. Carbonate *v*2 Band

There are two primary carbonate bands which show up in the IR spectra of bone mineral and hydroxyapatite: the *v2* out of plane bend (Figure 20) and the *v*3 asymmetric stretch modes [32]. The *v*3 CO_3^{2-} mode (1500 – 1400 cm^{-1}) is often used to characterize CO_3^{2-} in carbonated hydroxyapatite, but in BC750 this band overlaps with intense bands which are associated with the carbonaceous phase (see Appendix C), so was not used in analysis [33,34]. The *v*2 CO_3^{2-} mode at approximately 875 cm^{-1}, on the other hand, is largely unobscured by amorphous carbon bands of bone char because the carbonaceous phase of bone char does not show the intense peaks associated with aromatic ring C-H out-of-plane wag modes (see Figure 24 and Appendix C). Like the *v*3 mode, the carbonate *v*2 mode is highly sensitive to substitutional position, protonation and local environment. The frequency for A-type substitutions is observed at ~880

cm^{-1}. B-type substitutions are observed over the range 871 – 875 cm^{-1} with the exact frequency depending on local environment and coupling with A-type carbonate modes [31]. The effect of structural water in channel sites on the frequency of B-type CO_3^{2-} has not been well characterized, but some effect is possible. Other forms of CO_3^{2-} found in biogenic and synthetic hydroxyapatite also have vibrational modes nearby: labile carbonate (L-type) at ~866 cm^{-1} and HCO_3^- at ~843 cm^{-1} [34,37]. There may also be some weak contribution from P-(OH) or H_2CO_3 modes at ~890 - 900 cm^{-1} [34,44,45].

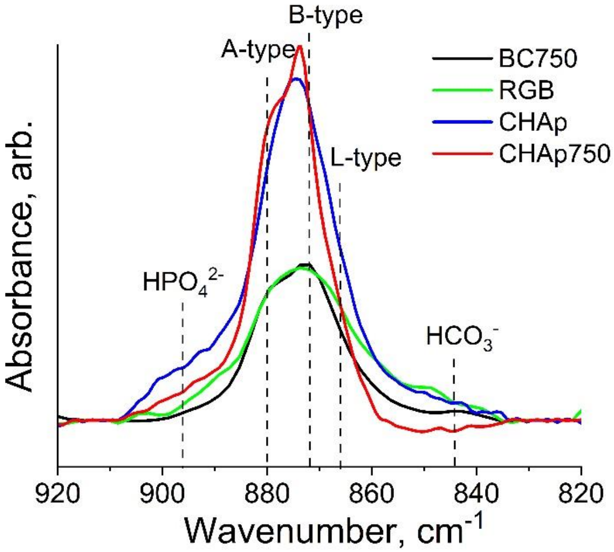

Figure 20: The *v*2 CO_3^{2-} band of representative spectra for each material. With heating, the total peak area for CHAp→CHAp750 and RGB→BC750 remaining constant with heating which indicates little to no total CO_3^{2-} was lost during heating. The discrepancy between peak intensities for bone-based vs. synthetic materials does not necessarily indicate that CHAp and CHAp750 contain more CO_3^{2-} than RGB and BC750.

According to the method of Rey, *et al.* comparison of the area of peaks within the *v*2 CO_3^{2-} band is indicative of the relative content of each substitutional species [32–34]. In this current work relative change of each type due to pyrolysis was the primary focus. In addition, using this method enabled investigation into the effects of pyrolysis on CO_3^{2-} substitutions in synthetic vs. biogenic materials, and provided insight into thermal recalcitrance of defects in bone mineral which are not observed in synthetic carbonated hydroxyapatite.

The HPO_4^{2-} peak area was subtracted prior to calculation of percent areas so that relative differences in CO_3^{2-} band areas only were considered. It is of note that with heating, the HPO_4^{2-} peak area for biogenic and synthetic materials showed a significant decrease. Results of peak fitting for all four materials in this present study (Table XIII) revealed significant differences in the material response to pyrolysis for synthetic hydroxyapatite compared to bone mineral. Additionally, differences in the relative contributions of all four carbonate types to the total band area were observed for BC750 and CHAp which are likely to impact solubility, acid/base buffering capacity, and mechanisms of aqueous metals removal.

Table XIII: Mean (±σ_s) percent of the total area for individual peaks in *v*2 CO_3^{2-} band after HPO_4^{2-} peak subtraction

	RGB (%)	BC750 (%)	CHAp (%)	CHAp750 (%)
A-type	19.7 (± 3.1)	34.8 (± 0.9)	6.2 (± 3.8)	45.8 (± 1.2)
B-type	24.7 (± 2.2)	33.8 (± 3.3)	47.4 (± 8.2)	27.5 (± 0.5)
L-type	43.9 (± 1.9)	27.8 (± 1.9)	35.6 (± 0.8)	25.1 (± 1.5)
HCO_3^-	11.8 (± 1.3)	3.6 (± 0.6)	8.9 (± 1.7)	0.7 (± 0.6)

With heating to 750°C, no significant change in total *v*2 CO_3^{2-} band area was observed for either CHAp→CHAp750 or RGB→BC750 (Figure 21a,b). Statistical comparison of pyrolyzed and unpyrolyzed materials was made at the $p < 0.05$ level using paired t-tests on the mean of three samples ($n = 3$). Both synthetic hydroxyapatite and bone mineral showed a decrease in L-type and HCO_3^- with heating, in agreement with trends observed by others [31,34]. The percentage of L-type lost with heating was greater for RGB than for CHAp. An increase in B-type CO_3^{2-} was observed for RGB→BC750, however for CHAp→CHAp750 a decrease was observed. A-type CO_3^{2-} increased with heating for both bone mineral and synthetic apatite.

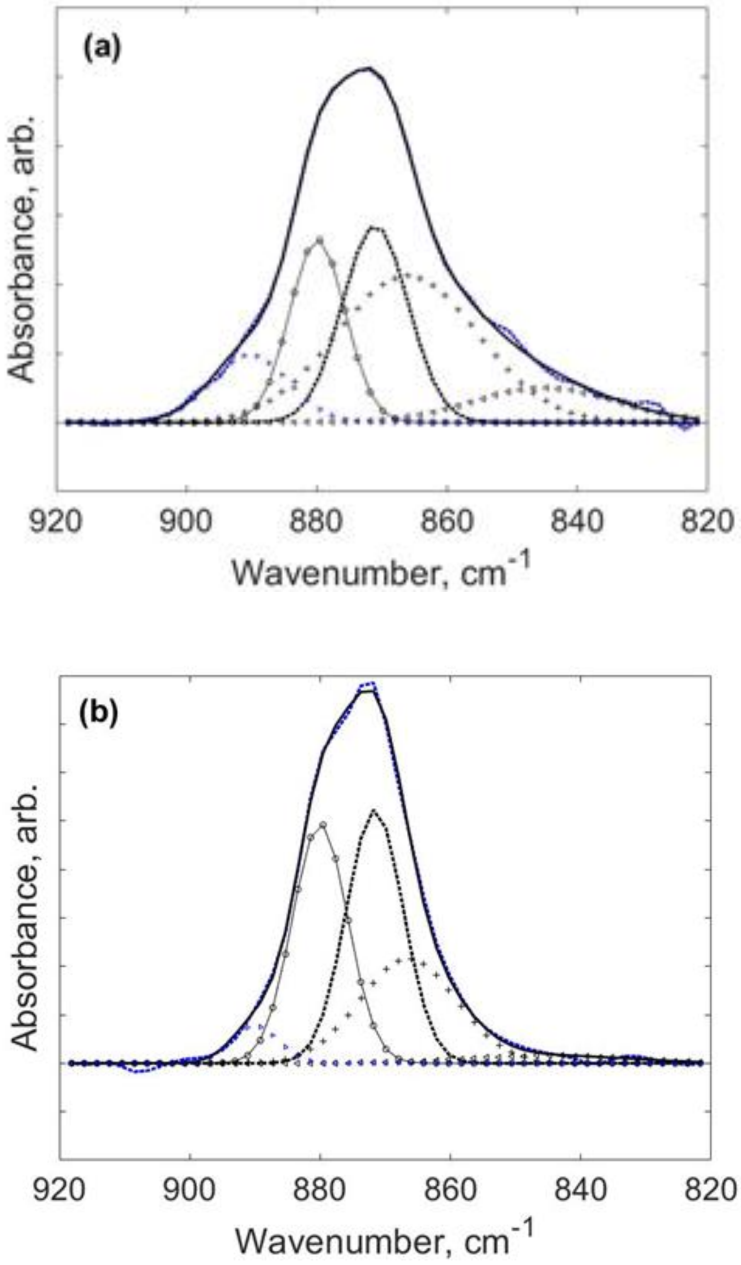

Figure 21: Carbonate v2 band for (a) RGB and (b) BC750; with raw spectrum (dashed blue), fitted total band (solid black), and subpeaks from left to right: HPO_4^{2-} peak (blue right-hand triangles), A-type CO_3^{2-} (open circles), B-type CO_3^{2-} (dashed), L-type CO_3^{2-} (black +), and HCO_3^- peak (black left-hand triangles).

CHAp contained primarily B- and L-type CO_3^{2-} substitutions with minor contributions from HCO_3^- and A-type. Following pyrolysis, CHAp750 lost nearly all HCO_3^-, and saw approximately 42% and 29.5% reduction in B- and L-type CO_3^{2-}, respectively. More than six-fold increase in A-type CO_3^{2-} contribution was observed following pyrolysis. While this may initially seem exceptional, it is likely explained by conversion of other forms of CO_3^{2-}, particularly L-type and B-type, into A-type as has been proposed by others, this conversion being enabled by the loss of channel OH^- at temperatures above 600°C [33,34,46]. Conversion of B-type to A-type typically been attributed to migration of CO_3^{2-} from the phosphate position into the neighboring channel as OH^- vacancies are created by thermal effusion of this species (and subsequent water and oxygen formation) during heating or reaction with other protonated species [33]. De-hydroxylation has been observed in hydroxyapatite having high initial OH^- content [20]. Significant water effusion (Figure 18, top) observed above 600°C for CHAp supports this mechanism.

RGB contained comparable levels of A- and B-type CO_3^{2-}, typical for bone mineral, with nearly half the total CO_3^{2-} present as L-type. With pyrolysis, the relative contributions from L-type and HCO_3^- decreased significantly. The HCO_3^- contribution reduced by more than half and L-type contribution reduced by approximately a third. B-type CO_3^{2-} increased by 37% with heating, in contrast to the behavior of this species in CHAp→CHAp750, while A-type CO_3^{2-} increased with pyrolysis by 77%. Effects of pyrolytic processes such as dehydration of primary bone mineral and interlaminar regions, secondary reactions between water and HPO_4^{2-}, HCO_3^- and OH^-, and effects of gaseous products (i.e. CO_2 and water) from collagen pyrolysis on carbonate substitutions are likely during bone char formation and have not been well-characterized previously. From *v*2 CO_3^{2-} analysis, formation of A-type and B-type CO_3^{2-} from L-type and HCO_3^{2-} appears likely and is possibly driven by the loss of excess water, presence of CO_2 in evolving pyrolysis products, or reactions at elevated temperature involving water and

HPO_4^{2-}, HCO_3^- and OH^-. These phenomena would explain the observed reduction of HPO_4^{2-} and HCO_3^- with heating [25,33,38].

4.3.2.2.3. Phosphate *v*3 Band

The phosphate *v*3 mode, between 1200 – 900 cm^{-1} is another region rich with structural information, made up of multiple component peaks which are related to the tetrahedral modes of PO_4^{3-}. For an isolated PO_4^{3-} tetrahedra, the P-O stretch is triply degenerate. However, inclusion in the apatite lattice, on the surface, or in a non-apatite phases result in distortion of the tetrahedra, observed in the IR spectrum as splitting of these vibrational frequencies. Multiple P-O modes are often observed in bone and hydroxyapatite between 1100 – 900 cm^{-1}, and this has been well-known and exploited in bone research [19,39,47,48]. In addition to tetrahedral PO_4^{3-}, HPO_4^{3-} is known to exist within the primary crystallites (believed to persist due to charge balance requirements) and especially in amorphous or non-apatite species in both bone mineral and hydroxyapatite, with more than half found in the hydrated interlaminar regions of bone mineral [38]. Monohydrogen phosphate, or acid phosphate (HPO_4^{2-}), has (OH)P=O stretch modes between 1300 – 1100 cm^{-1}, with a PO-H bend mode at 989 cm^{-1}, and possible other modes (discussed in Section 4.3.2.2.2) related to resonance with the OH^- stretch [38,41,45,49]. The *v*1 PO_4^{3-} mode is visible at 960 cm^{-1}, shown in Figure 19b [39].

Second derivative spectroscopy has been used extensively by bone researchers to track the structural relevance of peaks in the broad, overlapping *v*3 PO_4^{3-} band of bone and hydroxyapatite spectra [39,48,50]. Through comparison of peak positions in the spectra of a range of calcium phosphates, including OCP, brushite, monetite, amorphous calcium phosphate, and synthetic hydroxyapatites with carefully synthesized crystallinity and substitutional content, some characteristic phosphate modes in bone mineral have been determined [39,47,48]. In the present work, the complexity of the *v*3 PO_4^{3-} band (Figure 19b) in all four materials confounded the identification of specific bands in the zero-order absorbance spectra, so second derivative analysis was used instead to identify new peaks and those which showed the most change with pyrolysis. These observed changes point to differences in phosphate environments for BC750 compared to CHAp, and indicate that the phosphate environments in synthetic hydroxyapatite are more thermally stable than for bone mineral under the pyrolysis conditions in this study.

In the zero-order absorption spectrum of BC750, regions with strong intensity are observed which are either not observed directly in RGB or CHAp or are much weaker in those spectra. These regions appear to be PO_4^{3-} modes associated with hydroxyapatite, poorly-crystalline freshly-deposited apatite, and non-apatite phases for BC750. The primary sub-peaks in the *v*3 PO_4^{3-} band for CHAp were found to be related to PO_4^{3-} in mature hydroxyapatite, with some contributions from mature, poorly crystalline hydroxyapatite containing HPO_4^{2-} [39]. No significant change is observed in this band structure with heating, as evidenced by the similarity between second derivative spectra of CHAp and CHAp750 in Figure 22.

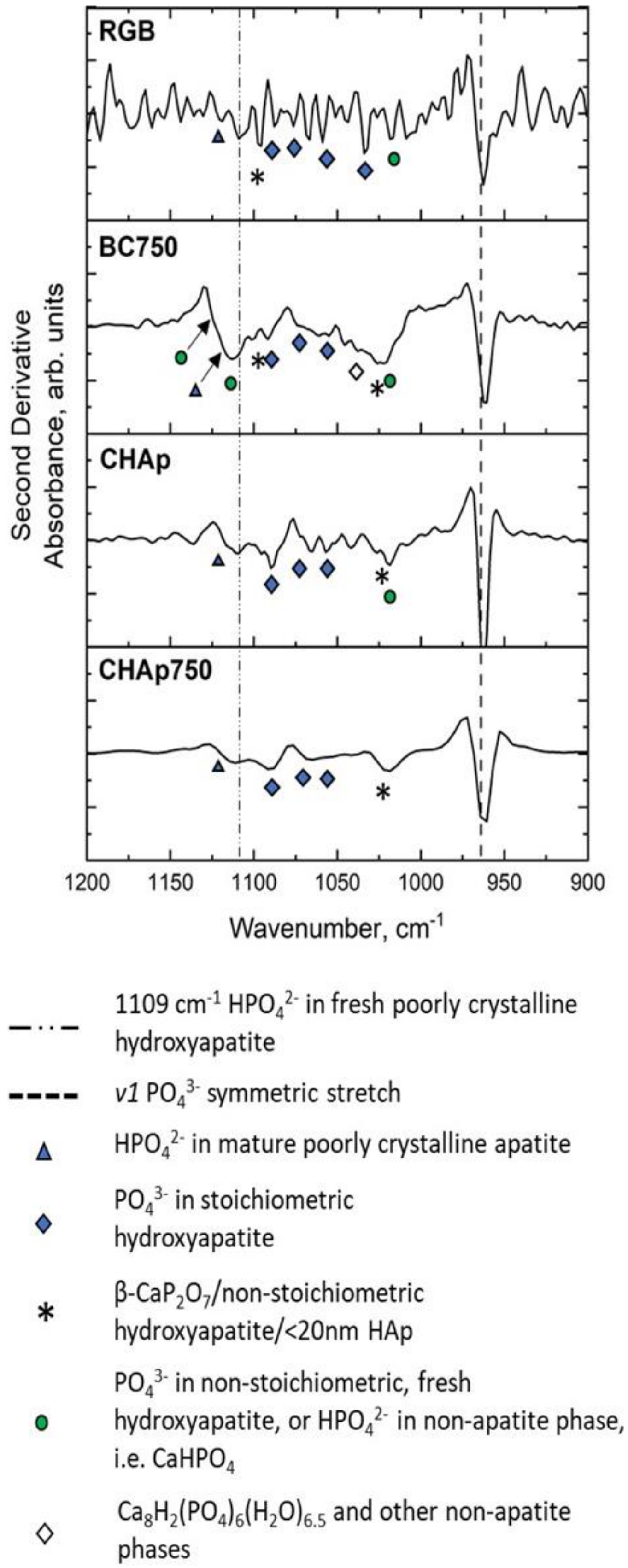
RGB
BC750
CHAp
CHAp750
Second Derivative Absorbance, arb. units
1200
1150
1100
1050
1000
950
900
Wavenumber, cm^{-1}
—··— $1109\ cm^{-1}\ HPO_4^{2-}$ in fresh poorly crystalline hydroxyapatite
- - - - *v1* PO_4^{3-} symmetric stretch
▲ HPO_4^{2-} in mature poorly crystalline apatite
◆ PO_4^{3-} in stoichiometric hydroxyapatite
* β-CaP_2O_7/non-stoichiometric hydroxyapatite/<20nm HAp
● PO_4^{3-} in non-stoichiometric, fresh hydroxyapatite, or HPO_4^{2-} in non-apatite phase, i.e. $CaHPO_4$
◇ $Ca_8H_2(PO_4)_6(H_2O)_{6.5}$ and other non-apatite phases

Figure 22: Second derivative IR spectra of v1,v3 PO_4^{3-} band were used to identify peaks which showed enhanced intensity in the spectrum of BC750 compared to RGB and CHAp. Important frequencies are denoted by symbols. CHAp750 did not show significant change compared to CHAp, indicating phosphate environments are largely thermally stable.

Increased intensity of second derivative minima at 1033 cm^{-1}, 1055 cm^{-1}, and 1074 cm^{-1} was observed in BC750. These peaks have previously been associated with stoichiometric hydroxyapatite [39]. Enhancement of these bands in BC750 compared to RGB can therefore be deemed as further evidence of an increase in ordering within existing primary crystallites, also evidenced by narrowing of XRD peaks discussed in Section 4.3.2.3.

By tracking changes in the HPO_4^{2-} vibrational modes for RGB → BC750 at 1112 cm^{-1}, 1109 cm^{-1} and 1127 cm^{-1}, it is hypothesized that some HPO_4^{2-} was integrated into newly formed apatite and some was present in non-apatite phases. The 1020 cm^{-1}, 1038 cm^{-1}, 1112 cm^{-1}, and 1127 cm^{-1} (here 1124 cm^{-1}) have been previously assigned to non-apatite PO_4^{3-} and/or acid phosphate in poorly crystallized hydroxyapatite [39,49]. A peak at 1116 cm^{-1} observed in BC750 and CHAp but not in RGB has previously been associated with HPO_4^{3-} in mature, poorly crystalline hydroxyapatite, which can be attributed to HPO_4^{2-} remaining in existing primary crystallites [39]. An enhanced minimum at 1112 cm^{-1}, not present in RGB and difficult to determine in CHAp, is observed for BC750. A peak at this frequency has previously been attributed to HPO_4^{2-} in newly formed, poorly crystalline apatite, and which we propose can probably be attributed here to apatite precipitated from HPO_4^{2-} originally in the interlaminar regions on the surfaces of existing crystallites. Peaks at 1026 cm^{-1} and 1100 cm^{-1} have been assigned to calcium pyrophosphate (β-CaP_2O_7), at 1038 cm^{-1} to non-apatite phases and OCP ($Ca_8H_2(PO_4)_6(H_2O)_{6.5}$), and at 1060 cm^{-1} and 1124 cm^{-1} to brushite ($CaHPO_4(H_2O)_2$) [19,39,49,51].

While only hydroxyapatite peaks were detected by x-ray diffraction (Section 4.3.2.3), second derivative analysis of the *v*3 PO_4^{3-} band provides evidence for non-apatite environments of PO_4^{3-} and HPO_4^{3-} which have been previously associated with other phases. It has been well-established that bone mineral phosphate is primarily present as PO_4^{3-} but can also take the acid form (HPO_4^{2-}) to compensate charge, for instance in calcium deficient local environments or at surfaces [29,39,49,51]. In raw bone, primary crystallites are surrounded by a hydrated interlaminar phase containing, among other species, HCO_3^- and HPO_4^{2-} [26,52]. Previously identified as having an amorphous structure, the fate of this amorphous surface layer with heat treatment is, to the best of the present authors' knowledge, not characterized [28,38]. When water is driven rapidly from these surface layers during heating, nucleation of amorphous or non-apatite phases would be likely, as would secondary reactions between constituent species. Fowler, *et al*. noted that acid calcium phosphates (specifically OCP), in the presence of hydroxyapatite, form pyrophosphates and brushite plus apatite and water with heat treatment [19]. Young, *et al.* observed the formation of pyrophosphate with heating to 500°C as a very weak peak at 730 cm^{-1} for non-carbonated hydroxyapatite and sheep bone. Those authors attributed this to thermally-driven reaction between HPO_4^{2-} groups, releasing water and forming pyrophosphate in solid solution with biological apatite [38]. While significant water effusion was observed for CHAp heated above 650°C, no peaks at 730 cm^{-1} were observed for BC750 or CHAp750, indicating the formation of pyrophosphate was inhibited during pyrolysis. It is not known whether the 730 cm^{-1} peak or the peaks at 1026 cm^{-1} and 1100 cm^{-1} are most indicative of pyrophosphate formation. Since D-BC750 does have some intensity associated with N-H wag in the area of 730 cm^{-1} (Figure 24) it is possible that in BC750 these modes obscure this weak pyrophosphate mode.

4.3.2.3. X-ray Diffraction of Bone Mineral and Hydroxyapatite

X-ray diffraction was used to investigate mineral phases present in all samples, but not for characterization of carbonaceous phases. Normalized, cropped, vertically offset diffraction patterns for CHAp, CHAp750, BC750, and RGB are shown in Figure 23 with some primary reflections annotated. Complete patterns for all materials are found in Appendix C. All materials were found to have a hydroxyapatite crystal structure [53]. While it could be assumed that this means only hydroxyapatite is present, it is possible for other phases have formed in precipitates which are too small or too disordered for Bragg diffraction.

Peak fitting of the (002) and (300) reflections was used to find hexagonal unit cell parameters for hydroxyapatite and bone mineral, reported in Table XIV with standard error and percent change and propagated error associated with pyrolysis. Raw data was fit with an appropriate number of Lorentzian curves plus a linear background for the (002) and (300) peaks. Calculations and graphical representations of fitted curves are summarized in Supplementary material Appendix C, Section 1.

Table XIV: Unit cell parameters calculated from results of peak fitting of (002) and (300) Bragg reflections ± standard error

	Lattice Parameter, Å		**Percent change with heating**	
	a	**c**	**Δa, %**	**Δc, %**
RGB	9.4236±0.0022	6.8872±0.0002		
BC750	9.4297±0.0003	6.8723±0.0001	0.6 ± 0.2	-1.5 ± 0.02
CHAp	9.4133±0.0004	6.8788±0.0002		
CHAp750	9.4003±0.0002	6.8697±0.0001	-0.1 ± 0.04	-0.9 ± 0.02

*negative percent change implies contraction of the axis; positive percent change implies expansion

The effects of pyrolysis on unit cell parameters of bone mineral and hydroxyapatite in the present study can be approximated by comparing RGB/CHAp (no heating) to BC750/CHAp750 (rapid heating to 750°C). In the present study, for CHAp → CHAp750, the a-lattice parameter decreased by 0.1 ± 0.04% and the c-lattice parameter decreased by 0.9 ± 0.02%. For RGB→BC750 a increased by 0.6 ± 0.2% and c decreased by 1.5 ± 0.02%. Changes in lattice parameters of primary crystallites of bone mineral and hydroxyapatite for RGB → BC750 and CHAp → CHAp750 can result from pyrolytic processes which enhance ordering within the crystallites, including dehydration, potential reactions between species, and changes in substitutional type and content. Additionally, at higher temperature, increased mobility of species may also impact ordering within primary crystallites. Enhanced ordering within primary crystallites, as well as growth of crystallites in the a- and c-directions, impacts lattice parameters in that local lattice strain at defects and surfaces becomes less impactful on the average. Changes observed here are considered as the cumulative effects of all phenomena.

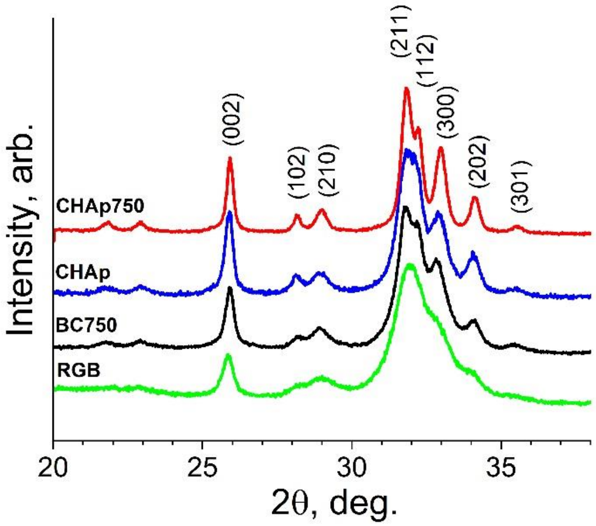

Figure 23: XRD patterns for CHAp750 (top), CHAp (second from top), BC750 (second from bottom), and RGB (bottom). The indices associated with the lattice planes for some reflections are included (Jeong, 2019). All materials exhibit peaks consistent with hydroxyapatite crystal structure with varying degrees of crystallinity.

The effect of carbonate ion substitutions on hydroxyapatite unit cell parameters compared to pure hydroxyapatite have been well-studied and reported by others [33]. In perfect hydroxyapatite, when CO_3^{2-} substitutes for OH^- in the channel site (or A-site), the planar ion orients perpendicular to the c-axis and for charge neutrality, one CO_3^{2-} ion substitutes for two OH^- ions. The result is an overall contraction of the c-axis [18,33]. In the B-site, one CO_3^{2-} substitutes for one PO_4^{3-} with charge neutrality being accounted for by vacancies or water substitution [24,32,46]. CO_3^{2-} in purely B-type hydroxyapatite is believed to occupy the face of the PO_4^{3-} tetrahedra roughly normal to the a-axis, hence contraction in the a-direction and expansion in the c-direction are typically observed for B-type substitutions [18,33].

For materials which already contain one or more carbonate species as well as other impurities, the changes in lattice parameter may not follow expected trends. In this case, changes relative to the starting carbonate content must be considered. Bone mineral is known to be AB-type, and both RGB and BC750 were found to be of this type in the present study [32,33,46]. The changes in lattice parameters for RGB → BC750, it seems, could be accounted for by the increase in both A-type and B-type CO_3^{2-}, with the dramatic effects of increased A-type dampened by the effects of increase in B-type. Etok and Rogers, *et al.* observed the same trend with bone mineral derived from combusted meat and bone meal [54]. For CHAp → CHAp750, one may consider the case of starting with a purely B-type CO_3^{2-} and transitioning to AB-type. In this case, the work of Madupalli, *et al.* implies that an increase in a and no change in c should be observed. For CHAp → CHAp750, the decrease in c is consistent with an increase in A-type CO_3^{2-}, however the decrease in a is not consistent with either reduction in B-type or increase in A-type.

Others have observed strong effects on the temperature response of lattice parameters due to CO_3^{2-} content at lower temperatures than used in this present study, but this effect at elevated temperatures is not well-known [55,56]. Young, *et al.* observed a decrease in a with heating of carbonated hydroxyapatite with heating to 400°C [57]. Those authors propose a reaction between atmospheric CO_2 and channel OH^-, producing channel carbonate and water vapor. This mechanism seems unlikely with pyrolysis in Ar, however reaction between B-type CO_3^{2-} and water, or between OH^- and residual HCO_3^-, coupled with integration of labile species into the A-type channel configuration may be responsible. DRIFTS results support this hypothesis, where with pyrolysis, HCO_3^- and L-type content decreased significantly for both CHAp→CHAp750 and RGB→BC750. The effect of these species on lattice parameters is not well-characterized, but it is possible they have a measurable impact in addition to that caused by B-type and A-type substitutions. Other secondary reactions could occur, including conversion of HPO_4^{2-} to PO_4^{3-} with the loss of OH^- observed by TGA-MS. Young and Holcomb observed that for hydroxyapatite heated to 500°C HPO_4^{2-} was converted to pyrophosphate, resulting in an overall increase in a [38]. Pyrophosphate was not observed in CHAp750, however was observed in BC750 using second derivative DRIFTS, consistent with the findings of Young and Holcomb.

Peak broadening, measured by the full width at half the peak maximum (FWHM), is associated with nanometer-scale crystallinity and disorder-induced microstrain and was observed for all materials compared to a perfect hydroxyapatite crystal [18,29,58]. FWHM for the (002) and (300) peaks is summarized in Appendix 1. For BC750 and CHAp750 heating resulted in narrower peaks compared to RGB and CHAp, respectively, consistent with enhanced crystallinity. All materials showed more change in FWHM of (002) than for (300), indicating more ordering in the c-axis direction with pyrolysis, consistent with the findings of others [59].

Rogers presented evidence that microstrain is the dominant mechanism of peak broadening in native bone mineral with the collagen matrix intact [59]. Complete structural refinement according to the Rietveld method would be necessary to separate effects of microstrain and size broadening, and this capability was not available for the present study [33,58,59]. Evidence for enhanced ordering in the primary crystallites of BC750 due to pyrolysis was found by DRIFTS second derivative analysis, however, in agreement with the general trends observed in the FWHM of the (002) and (300) peaks and with the findings of Rogers, *et al*.

4.3.3. Characterization of the Carbonaceous Phase

The impacts of the carbonaceous phase of bone char on heavy metals removal has not been well-characterized and further study is certainly warranted to determine the maximum capacity and associated mechanisms by which it adsorbs particularly Cu^{2+}. Insight into the surface chemistry of this phase can help guide any future work. Aromatic carbon, amide, amine, and hydroxyl groups have strong IR intensity associated with characteristic vibrational modes, but these often overlap with vibrational modes associated with the mineral phase of bone and bone char. Therefore, in the present work, functional groups in the carbonaceous phase of BC750 were characterized using demineralized BC750 (D-BC750).

The presence of collagen chains and carbohydrates in raw bone tissue indicates that Maillard-type reactions are likely to occur in the early stages of pyrolysis. Maillard reaction products from glycine/glucose reaction up to 300°C were observed by others to include nitrogen heterocycles with amine, carbonyl, and methyl functional groups [60]. The carbonaceous phase of pyrolyzed bone has been investigated for electrochemical applications because of properties endowed by the presence of nitrogen-doped aromatic clusters [61,62]. Nitrogen in amine or amide groups (from collagen) and in aromatic compounds both have important implications for

Cu^{2+} adsorption. For instance, Huang, *et al.* synthesized novel amine-functionalized Fe_3O_4 nanoparticles to remove Cu^{2+} from aqueous solution [63]. More recently, similar synergistic effects were observed where pyrolyzed bone was found to adsorb complexes of tetracycline and Cu^{2+} from aqueous solution [64]. In addition to amine and amide groups, aromatic nitrogen could also be involved in Cu^{2+} adsorption as indicated by the strong performance of 1,10-phenanthroline in Cu-binding applications [64–67]. High nitrogen content is known to favor increased clustering of aromatic rings, which promote the formation of a porous, thermally stable macrostructure [68,69].

4.3.3.1. DRIFTS Characterization of the Carbonaceous Phase

The DRIFTS spectra of RBG, BC750, and D-BC750 are shown in Figure 24. The spectrum of RGB is dominated by the amide 1° and 2° bands and biological apatite peaks with some potential amide 3° character around 1220 cm^{-1}. Contribution from the acid phosphate P=O stretch is also likely in that same region [45,70]. Collagen amide components are apparent in the N-H stretch region between 3300 – 3000 cm^{-1} and the fingerprint region, with prominent peaks there due to -C=O stretch at ~1730 cm^{-1}, and 1°, 2°, and 3° amide -C-N- stretches centered at ~1640 cm^{-1}, ~1550 cm^{-1}, and ~1220 cm^{-1}, respectively. Raw bones were initially boiled to remove soft tissue, so these combined C-N and N-H modes correlate with observed positions for thermally denatured type I collagen [70].

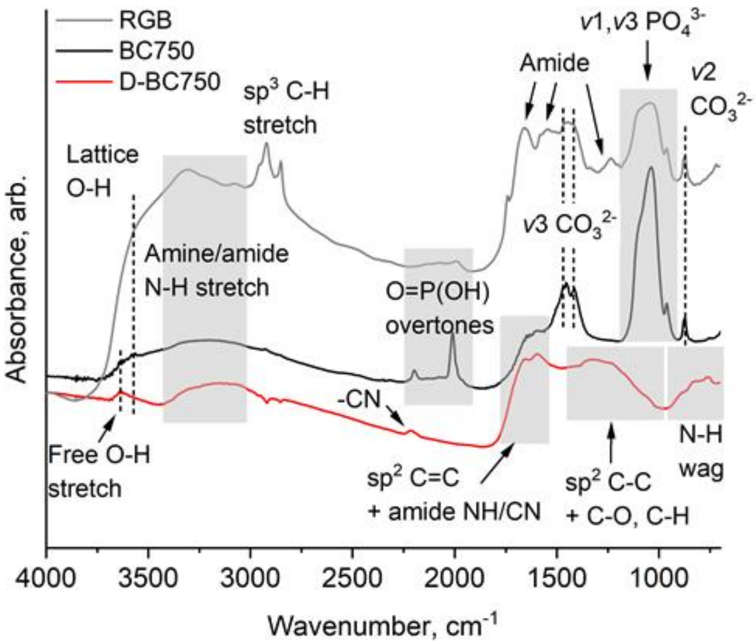

Figure 24: DRIFTS spectra for RGB, BC750, and D-BC750. Despite pyrolysis, some amide and/or amine character of bone collagen is retained, most apparent in D-BC750. This could have strong implications for Cu^{2+} removal.

Despite high temperature pyrolysis and acid leaching, some collagen amide character is still visible in the spectra of BC750 and D-BC750, respectively, apparent in the N-H stretch modes between 3400 – 2700 cm^{-1} and amide band at 1700 – 1500 cm^{-1}. For BC750 the intensity of the broad water band between 3500 – 2700 cm^{-1} is significantly lower than in RGB indicating limited adsorption of atmospheric H_2O. For D-B750 this band is practically absent indicating hydrophobicity. A prominent shoulder is visible for BC750 at 3630 cm^{-1} which is also apparent in D-BC750. In D-BC750, this band is asymmetric with the maximum at ~3625 cm^{-1} and residual intensity toward lower wavenumbers. The position above 3600 cm^{-1} is indicative of a free O-H stretch. The phenolic free O-H stretch, absent of hydrogen bonding or confinement effects, is observed at ~3670 cm^{-1}, so decreased frequency signifies this group is involved in hydrogen bonding [45,71]. Intensity in the 3400 – 2700 cm^{-1} region is primarily attributed to N-H stretches, with broadening attributed to heterogeneity in the chemical environment of these groups. The presence of nitrogen heterocycles containing amine functionalities, particularly 5-membered rings which have been observed in Maillard reactions of amino acids, would extend this band well into the 2800 cm^{-1} region, which is observed in Figure 24 for D-BC750 [45,60].

A small peak at ~2200 cm^{-1} in the spectra for BC750 may contain components of $v3$ PO_4^{3-} peak overtones. Because this band persisted following demineralization with a slight change in shape and position, we attribute some intensity here to $v3$ PO_4^{3-} band overtone, and some intensity to -C≡N groups in the carbonaceous phase [72].

The fingerprint region of BC750 contains overlapping bands associated with mineral and carbonaceous phases as well, so D-BC750 is used in the following discussion for that region. Some residual amide character is apparent between 1700 – 1600 cm^{-1} contributions from the C=O stretch at 1650 cm^{-1} and NH_2 scissor modes at around 1620 cm^{-1}. Contributions to intensity from aromatic carbon are apparent in a major peak at ~1580 cm^{-1} and between 1500 – 1000 cm^{-1}. At least some contribution to the intensity between 1500 – 1000 cm^{-1} is attributed to epoxide or ether groups as well, common in lignocellulose-based biochar. Similarity between the spectra of D-BC750 and wood-based biochar in this region indicate similar structures may be present (Appendix C, Figure 5). Intensity in the 1500 – 1000 cm^{-1} range from sp^2 and sp^3 C-H bend modes are also present at ~1400 cm^{-1} and ~1020 cm^{-1}, respectively [45,69].

The spectrum for D-BC750 is compared to that of a wood-based biochar in Appendix C, to highlight the unique functional group chemistry on the bone char related to feedstock. BC750 contains -OH and amine and/or amide functional groups, whereas biochar contains primarily carbonyl and ether groups in addition to C-H attached to aromatic and sp^3 carbons.

4.3.3.2. Raman Spectroscopy of the Carbonaceous Phase

In the case of B750, the mineral phase contains many Raman active modes, but these were obscured by strong scattering from carbonaceous phases at the low laser power necessitated by the need to avoid thermally damaging the sample. Therefore, Raman spectroscopy was only used in this study for characterization of the carbonaceous phase.

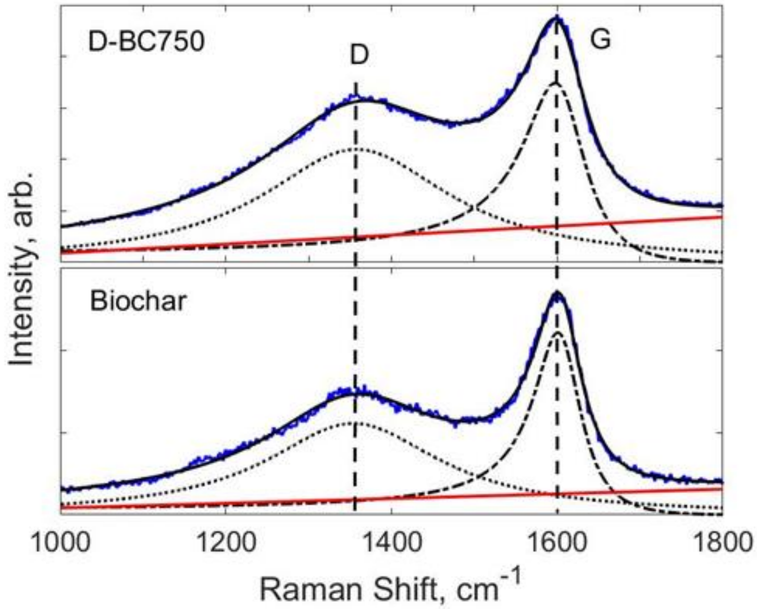

Figure 25: Raman fits for D-BC750 and a comparative wood-based biochar using the two-peak model according to Ferrari and Robertson (Ferrari and Robertson, 2000) which implements a Lorentzian line shape for the D peak and BWF line shape for the G peak. The benefit of the Ferrari-Robertson model is a reasonable fit, including the high-intensity valley between the D and G peaks, with minimized risk of "over-fitting".

The Raman spectrum for BC750 and D-BC750 exhibit the characteristic shape for amorphous carbons containing defected sp^2 and sp^3 hybridized carbon. Two characteristic peaks are present in D-BC750: G and D. The so-called G peak originates from the E_{2g} Raman allowed optical phonon mode at the Brillouin zone center. The G peak is present in all polyconjugated carbons and is related to the bond stretching of sp^2 hybridized carbon pairs. The D peak, only observed for aromatic clusters. The D peak is due to ring-breathing mode of the A_{1g} optical phonon at **K**, which is activated by relaxation of the fundamental selection rule associated with the presence of defected clusters of aromatic rings [73]. Different types of defects can activate the D peak, for instance edges of ordered sp^2 clusters, sp^3 hybridized species, or heteroatoms [73]. Ferrari and Robertson, *et al.* proposed a model by which to characterize amorphous carbon films which is appropriate for amorphous pyrolysis chars because it accounts for the well-known non-graphitizing thermal behavior, fine size distribution of sp^2 and sp^3 domains, the presence of 5-, 6-, 7- membered aromatic rings, linear conjugated chains, hydrogen and heteroatom content of biochars [75–80]. According to this model, two peaks can satisfactorily fit the first order region, between 1100 – 1700 cm^{-1}, and the parameters for these fitted peaks are related to the average degree of order and aromaticity in the material. In the following discussion, the biochar from Section 4.3.3.1 was included to highlight the enhanced aromatic ring clustering in bone char, possibly catalyzed by the mineral phase.

The two-peak model includes a Breit-Wigner-Fano (BWF) function (Appendix C) for the G peak, a single Lorentzian function for the D peak and a linear background. The BWF function is appropriate for amorphous carbon because the asymmetric shape allows for a better fit of the "valley" region between the D and G peaks without the inclusion of additional peaks [22,72]. There is evidence that this line-shape has a physical origin as well [81]. Further description of the BWF function is found in Appendix C.

Raw data for the Raman spectra of D-BC750 is shown in Figure 25, plotted together with the fitted curve, D and G bands, and the linear background. The results of fitting for BC750, D-BC750 and biochar (for comparison) are summarized in Table XV, where reported values represent the arithmetic mean value for at least three measurements taken at different points on the sample, with standard error reported. Raman fit for BC750 is shown in Appendix C. No statistically significant difference in mean values of ID/IG, G position, or FWHM(G) was observed between D-BC750 and BC750 using a paired one-tail t-test for $n = 3$ at the $p < 0.05$ level.

Table XV: Results of Raman peak fitting (±SE)

	ID/IG	**G position**	**FWHM(G)**
BC750	0.726 ±.0053	1604.9 ±0.93	89 ±0.66
D-BC750	0.660±0.045	1604.3 ±2.33	88 ±3.01
Biochar	0.483±0.031	1601.3 ±2.89	68 ±1.90

The general picture of the carbonaceous phase of bone char from the Ferrari-Robertson model is a highly defected, amorphous carbon consisting of small ordered clusters of aromatic rings and the presence of conjugated linear chains, evidenced by a G position >1600 cm^{-1} [82]. I(D)/I(G) lies between 0.73 and 0.66, which indicates clustering of aromatic rings on the order of 1 – 2 nm, and the FWHM(G) lies at approximately 89 cm^{-1}, indicating relatively low ordering within all sp^2 phases [83].

The Raman spectrum of biochar, in comparison, has a lower I(D)/I(G) at 0.48, slightly lower G peak position at 1601 cm^{-1}, and smaller FWHM(G) at 68 cm^{-1}. Comparing the results of the Raman fits for D-BC750 and biochar, it is apparent from I(D)/I(G) that D-BC750 contains larger clusters of aromatic rings but the distance between defects in these rings is shorter, possibly due to higher nitrogen heteroatom content of aromatic rings in bone char [69].

4.4. Conclusions

The results of this study point to several fundamental differences in chemistry and structure between bone char and carbonated hydroxyapatite which are likely to account for higher maximum removal capacity of aqueous metals, and particularly Cu^{2+} by bone char. Despite both materials having the same hydroxyapatite crystalline structure, bone mineral and synthetic carbonated apatite have different levels of substitutional species, including structural water and carbonate, known to influence crystallinity, solubility, and acid-buffering capacity. The presence of high quantities of A-type carbonate in addition to B-type and L-type, coupled with a distinct lack of structural OH^- in bone char, is indicative of persistent lattice disorder largely unaffected by heat treatment. These results indicate AB-type carbonated apatite with low OH^- is desirable for metals removal applications.

While primary crystallites of bone mineral became more crystalline with heating, non-stoichiometric apatite and non-apatite phases were observed after pyrolysis, including calcium pyrophosphate (CaP_2O_7) and brushite ($CaHPO_4^{2-}$). The small size of these alternate phases indicates very localized effects, and potentially a lower degree of charge compensation with higher reactivity. In contrast, there is no indication of pyrophosphate or other secondary phase in CHAp, even after pyrolysis. The overall complexity of bone mineral ionic environments presents characterization challenges despite being the most likely basis for high aqueous metal removal power.

The carbonaceous phase of pyrolyzed bone can be considered “amorphous carbon”, which consists of distinct clusters of sp^2 and sp^3 hybridized carbon, including aromatic rings, olefinic chains and dense tetrahedrally coordinated sp^3 carbon, as well as non-trivial quantities of volatiles and polymeric structures. The presence of amine, amide and oxygenated functional groups and heteroatom nitrogen indicates that the carbonaceous phase is likely to play a role in Cu^{2+} removal. We propose that further experimentation with aqueous Cu^{2+} adsorption by demineralized bone char would reveal more about the role of the carbonaceous phase in this application, and that there is potential synergy between carbonaceous and mineral phases of bone char driving enhanced metals removal.

5. Future Work

The outlook for biochar in applications such as dynamic ammonia adsorption and metals removal or recovery is strong, however much work is still needed. With the wide range of biomass feedstocks available, I propose that refined compositional studies like that presented in Chapter 2 are badly needed, particularly for hemp, grasses, and softwood biomasses. Acquisition of genetic variants with similar biopolymer and ash content for these biomass types may challenge this work, but I propose that it is necessary to capture the impacts of parameters like lignin S/G and potassium content on biochar structure and chemistry. Since sp^3 cross-linking and oxygenated groups appeared to vary among demineralized and untreated biochars, it is recommended that x-ray photoelectron spectroscopy or other quantitative surface analysis technique should be implemented to understand the extent of these chemical groups. Those techniques were not available for the present study, but should be conducted in the future. The final recommendation for biochar S/G and potassium is further study to probe the temperature range and heating regime which may lessen the closed porosity for untreated biochars.

While biochar showed strong potential in ammonia adsorption, repeat studies should be conducted with various particle sizes, flow rates, and C_0 to better understand the role of those parameters in determining breakthrough time. Additionally, those studies would lead to identification of the ideal conditions for optimization of breakthrough time. Since oxygen content may have been key in dynamic ammonia adsorption, it is recommended to repeat the study with biochars prepared at higher and lower temperature, which is a facile means of altering oxygen content. It is proposed that Boehm titration and acid site analysis with ammonia chemisorption would provide key quantification of surface oxygen groups to better understand the role they play in dynamic adsorption. The ammonia chemisorption instrumentation will be available for future studies, however was not available for this current work.

Finally, with respect to bone char in metals adsorption, this Ph.D. pointed out a number of key structural and chemical parameters which are likely to drive the strong performance of bone char in Cu^{2+} adsorption. Both static and dynamic adsorption studies are recommended to gain a firmer understanding of the dominant mechanisms of Cu^{2+} removal from acid mine waste, and the pH range associated for each. Lastly, further study is clearly needed to understand the effects of the nitrogen-rich carbonaceous phase on metals removal from water, not only for mine waste remediation, but to probe the functionality of bone char in electrochemical devices such as battery cathode materials.

6. Bibliography

[1] J. Rockström, W. Steffen, K. Noone, Å. Persson, F.S. Chapin, E.F. Lambin, T.M. Lenton, M. Scheffer, C. Folke, H.J. Schellnhuber, B. Nykvist, C.A. De Wit, T. Hughes, S. Van Der Leeuw, H. Rodhe, S. Sörlin, P.K. Snyder, R. Costanza, U. Svedin, M. Falkenmark, L. Karlberg, R.W. Corell, V.J. Fabry, J. Hansen, B. Walker, D. Liverman, K. Richardson, P. Crutzen, J.A. Foley, A safe operating space for humanity, Nat. 2009 4617263. 461 (2009) 472–475. https://doi.org/10.1038/461472a.

[2] M.J. Van Oosten, A. Maggio, Functional biology of halophytes in the phytoremediation of heavy metal contaminated soils, Environ. Exp. Bot. 111 (2015) 135–146. https://doi.org/10.1016/J.ENVEXPBOT.2014.11.010.

[3] O. Oenema, Nitrogen budgets and losses in livestock systems, Int. Congr. Ser. 1293 (2006) 262–271. https://doi.org/10.1016/J.ICS.2006.02.040.

[4] S. Stehle, S. Bub, R. Schulz, Compilation and analysis of global surface water concentrations for individual insecticide compounds, Sci. Total Environ. 639 (2018) 516–525. https://doi.org/10.1016/j.scitotenv.2018.05.158.

[5] M. Van Damme, L. Clarisse, S. Whitburn, J. Hadji-Lazaro, D. Hurtmans, C. Clerbaux, P.F. Coheur, Industrial and agricultural ammonia point sources exposed, Nat. 2018 5647734. 564 (2018) 99–103. https://doi.org/10.1038/s41586-018-0747-1.

[6] T. World Bank Group, The Global Health Cost of PM 2.5 Air Pollution A Case for Action Beyond 2021 INTERNATIONAL DEVELOPMENT IN FOCUS, (2022). https://doi.org/10.1596/978-1-4648-1816-5.

[7] C. Abbafati, *et al.*, Global burden of 87 risk factors in 204 countries and territories, 1990–2019: a systematic analysis for the Global Burden of Disease Study 2019, Lancet. 396

(2020) 1223–1249. https://doi.org/10.1016/S0140-6736(20)30752-2.

[8] Emissions Database for Global Atmospheric Research, (n.d.). https://edgar.jrc.ec.europa.eu/air_pollutants.

[9] S.N. Behera, M. Sharma, V.P. Aneja, R. Balasubramanian, Ammonia in the atmosphere: a review on emission sources, atmospheric chemistry and deposition on terrestrial bodies, Environ. Sci. Pollut. Res. 2013 2011. 20 (2013) 8092–8131. https://doi.org/10.1007/S11356-013-2051-9.

[10] X. Tan, S. Liu, Y. Liu, Y. Gu, G. Zeng, X. Hu, X. Wang, S. Liu, L. Jiang, Biochar as potential sustainable precursors for activated carbon production: Multiple applications in environmental protection and energy storage, Bioresour. Technol. 227 (2017) 359–372. https://doi.org/10.1016/j.biortech.2016.12.083.

[11] B. Han, C. Butterly, W. Zhang, J. zheng He, D. Chen, Adsorbent materials for ammonium and ammonia removal: A review, J. Clean. Prod. 283 (2021). https://doi.org/10.1016/J.JCLEPRO.2020.124611.

[12] M. Liu, X. Huang, Y. Song, J. Tang, J. Cao, X. Zhang, Q. Zhang, S. Wang, T. Xu, L. Kang, X. Cai, H. Zhang, F. Yang, H. Wang, J.Z. Yu, A.K.H. Lau, L. He, X. Huang, L. Duan, A. Ding, L. Xue, J. Gao, B. Liu, T. Zhu, Ammonia emission control in China would mitigate haze pollution and nitrogen deposition, but worsen acid rain, Proc. Natl. Acad. Sci. U. S. A. 116 (2019) 7760–7765. https://doi.org/10.1073/PNAS.1814880116/-/DCSUPPLEMENTAL.

[13] M. De Kwaadsteniet, P.H. Dobrowsky, A. Van Deventer, W. Khan, T.E. Cloete, Domestic Rainwater Harvesting: Microbial and Chemical Water Quality and Point-of-Use Treatment Systems, (n.d.). https://doi.org/10.1007/s11270-013-1629-7.

[14] C.F. Carolin, P.S. Kumar, A. Saravanan, G.J. Joshiba, M. Naushad, Efficient techniques for the removal of toxic heavy metals from aquatic environment: A review, J. Environ. Chem. Eng. 5 (2017) 2782–2799. https://doi.org/10.1016/J.JECE.2017.05.029.

[15] L. Joseph, B.M. Jun, J.R.V. Flora, C.M. Park, Y. Yoon, Removal of heavy metals from water sources in the developing world using low-cost materials: A review, Chemosphere. 229 (2019) 142–159. https://doi.org/10.1016/J.CHEMOSPHERE.2019.04.198.

[16] K. Islam, S. Murakami, Global-scale impact analysis of mine tailings dam failures: 1915–2020, Glob. Environ. Chang. 70 (2021) 102361. https://doi.org/10.1016/J.GLOENVCHA.2021.102361.

[17] M.J.K. Ahmed, M. Ahmaruzzaman, A review on potential usage of industrial waste materials for binding heavy metal ions from aqueous solutions, J. Water Process Eng. 10 (2016) 39–47. https://doi.org/10.1016/J.JWPE.2016.01.014.

[18] L. Lu, C. Chen, T. Ke, M. Wang, M. Sima, S. Huang, Long-term metal pollution shifts microbial functional profiles of nitrification and denitrification in agricultural soils, Sci. Total Environ. 830 (2022) 154732. https://doi.org/10.1016/J.SCITOTENV.2022.154732.

[19] I. Ashraf Badroo, H. Pradeep Nandurkar, A.H. Khanday, Toxicological impacts of herbicide paraquat dichloride on histological profile (gills, liver, and kidney) of freshwater fish Channa punctatus (Bloch), (n.d.). https://doi.org/10.1007/s11356-020-09931-6/Published.

[20] F. Xiao, J.J. Pignatello, Interactions of triazine herbicides with biochar: Steric and electronic effects, Water Res. 80 (2015) 179–188. https://doi.org/10.1016/j.watres.2015.04.040.

[21] M.K. Hailer, C.P. Peck, M.W. Calhoun, R.F. West, K.J. James, S.D. Siciliano, Assessing

human metal accumulations in an urban superfund site, Environ. Toxicol. Pharmacol. 54 (2017) 112–119. https://doi.org/10.1016/J.ETAP.2017.06.001.

[22] A.M. Morse, BASIN WILDRYE METAL CONTENTS IN RESTORED AND UNRESTORED AREAS ALONG SILVER BOW CREEK AND THE UPPER CLARK FORK RIVER, (n.d.).

[23] R.E. De La Hoz, D.P. Schlueter, W.N. Rom, Chronic Lung Disease Secondary to Ammonia Inhalation Injury: A Report on Three Cases, (n.d.). https://doi.org/10.1002/(SICI)1097-0274(199602)29:2.

[24] C.C. Huang, H.S. Li, C.H. Chen, Effect of surface acidic oxides of activated carbon on adsorption of ammonia, J. Hazard. Mater. 159 (2008) 523–527. https://doi.org/10.1016/J.JHAZMAT.2008.02.051.

[25] C.C. Rodrigues, D.B. De Moraes, S.W. Da Nó Brega, M.G. Barboza, Ammonia adsorption in a fixed bed of activated carbon, (2006). https://doi.org/10.1016/j.biortech.2006.03.024.

[26] A.J. Rieth, A.M. Wright, M. Dincă, Kinetic stability of metal–organic frameworks for corrosive and coordinating gas capture, Nat. Rev. Mater. 2019 411. 4 (2019) 708–725. https://doi.org/10.1038/s41578-019-0140-1.

[27] H. Marsh, F. Rodríguez-Reinoso, Activated Carbon, Elsevier Ltd, 2006. https://doi.org/10.1016/B978-0-08-044463-5.X5013-4.

[28] R. Hestrin, A. Enders, J. Lehmann, Ammonia volatilization from composting with oxidized biochar, J. Environ. Qual. 49 (2020) 1690–1702. https://doi.org/10.1002/JEQ2.20154.

[29] B. Wang, J. Lehmann, K. Hanley, R. Hestrin, A. Enders, Adsorption and desorption of

ammonium by maple wood biochar as a function of oxidation and pH, Chemosphere. 138 (2015) 120–126. https://doi.org/10.1016/J.CHEMOSPHERE.2015.05.062.

[30] Q. Yu, D. Xia, H. Li, L. Ke, Y. Wang, H. Wang, Y. Zheng, Q. Li, Effectiveness and mechanisms of ammonium adsorption on biochars derived from biogas residues, RSC Adv. 6 (2016) 88373–88381. https://doi.org/10.1039/C6RA16913A.

[31] X. Zheng, Z. Yang, X. Xu, M. Dai, R. Guo, Characterization and ammonia adsorption of biochar prepared from distillers' grains anaerobic digestion residue with different pyrolysis temperatures, J. Chem. Technol. Biotechnol. 93 (2018) 198–206. https://doi.org/10.1002/JCTB.5340.

[32] E. Agyarko-Mintah, A. Cowie, L. Van Zwieten, B.P. Singh, R. Smillie, S. Harden, F. Fornasier, Biochar lowers ammonia emission and improves nitrogen retention in poultry litter composting, Waste Manag. 61 (2017) 129–137. https://doi.org/10.1016/J.WASMAN.2016.12.009.

[33] Z. Ahmad, A. Mosa, L. Zhan, B. Gao, Biochar modulates mineral nitrogen dynamics in soil and terrestrial ecosystems: A critical review, Chemosphere. 278 (2021) 130378. https://doi.org/10.1016/J.CHEMOSPHERE.2021.130378.

[34] Renu, M. Agarwal, K. Singh, Heavy metal removal from wastewater using various adsorbents: a review, J. Water Reuse Desalin. 7 (2017) 387–419. https://doi.org/10.2166/WRD.2016.104.

[35] A.R. Betts, N. Chen, J.G. Hamilton, D. Peak, Rates and Mechanisms of Zn 2+ Adsorption on a Meat and Bonemeal Biochar, (2013). https://doi.org/10.1021/es4032198.

[36] M. Azeem, S.M. Shaheen, A. Ali, P.G.S.A. Jeyasundar, A. Latif, H. Abdelrahman, R. Li, M. Almazroui, N.K. Niazi, A.K. Sarmah, G. Li, J. Rinklebe, Y.G. Zhu, Z. Zhang,

Removal of potentially toxic elements from contaminated soil and water using bone char compared to plant- and bone-derived biochars: A review, J. Hazard. Mater. 427 (2022). https://doi.org/10.1016/J.JHAZMAT.2021.128131.

[37] E.P. Barrett, Trends in the Development of Granular Adsorbents for Sugar Refining, Adv. Carbohydr. Chem. 6 (1951) 205–230. https://doi.org/10.1016/S0096-5332(08)60068-5.

[38] E.P. Barrett, L.G. Joyner, P.P. Halenda, Granular Adsorbents for Sugar Refining. Some Factors Affecting Porosity and Activity in Service., Ind. Eng. Chem. 44 (2002) 1827–1833. https://doi.org/10.1021/IE50512A034.

[39] E.P. BARRETT Baugh, S. Co, M. Institute, P.J. M Brown, S.M. Oleck, Some Granular Carbonaceous Adsorbents for Sugar Refining A Study of Bone Char Replacements Based on Hydroxyapatite, 17 (2021) 5. https://pubs.acs.org/sharingguidelines (accessed September 17, 2021).

[40] K. Bosch, A. Freebourn, K. Parker, M. Scherman, K.R. Zodrow, D. Hutchins, Biochar for Enhanced Surface Water Quality, 2021 Waste-Management Educ. Res. Conf. (2021) 1–9. https://doi.org/10.1109/WERC52047.2021.9477543.

[41] Biochar for environmental management: an introduction, Biochar Environ. Manag. (2015) 33–46. https://doi.org/10.4324/9780203762264-8.

[42] K.A. Spokas, K.B. Cantrell, J.M. Novak, D.W. Archer, J.A. Ippolito, H.P. Collins, A.A. Boateng, I.M. Lima, M.C. Lamb, A.J. McAloon, R.D. Lentz, K.A. Nichols, Biochar: A Synthesis of Its Agronomic Impact beyond Carbon Sequestration, J. Environ. Qual. 41 (2012) 973–989. https://doi.org/10.2134/jeq2011.0069.

[43] J. Lehmann, J. Gaunt, M. Rondon, Bio-char Sequestration in Terrestrial Ecosystems – A Review, Mitig. Adapt. Strateg. Glob. Chang. 11 (2006) 403–427.

https://doi.org/10.1007/s11027-005-9006-5.

[44] W.-J. Liu, H. Jiang, H.-Q. Yu, Development of Biochar-Based Functional Materials: Toward a Sustainable Platform Carbon Material, Chem. Rev. 115 (2015) 12251–12285. https://doi.org/10.1021/acs.chemrev.5b00195.

[45] D. Woolf, J.E. Amonette, F.A. Street-Perrott, J. Lehmann, S. Joseph, Sustainable biochar to mitigate global climate change, Nat. Commun. 2010 11. 1 (2010) 1–9. https://doi.org/10.1038/ncomms1053.

[46] M. Keiluweit, P.S. Nico, M.G. Johnson, M. Kleber, Dynamic Molecular Structure of Plant Biomass-Derived Black Carbon (Biochar), Environ. Sci. Technol. 44 (2010) 1247–1253. https://doi.org/10.1021/es9031419.

[47] X. Xiao, Z. Chen, B. Chen, H/C atomic ratio as a smart linkage between pyrolytic temperatures, aromatic clusters and sorption properties of biochars derived from diverse precursory materials, Sci. Rep. 6 (2016) 22644. https://doi.org/10.1038/srep22644.

[48] K. Raveendran, Pyrolysis characteristics of biomass and biomass components, Fuel. 75 (1996) 987–998. https://doi.org/10.1016/0016-2361(96)00030-0.

[49] K. Raveendran, A. Ganesh, K.C. Khilar, Influence of mineral matter on biomass pyrolysis characteristics, Fuel. 74 (1995) 1812–1822. https://doi.org/10.1016/0016-2361(95)80013-8.

[50] M.R. Gray, W.H. Corcoran, G.R. Gavalas, Pyrolysis of a wood-derived material. Effects of moisture and ash content, Ind. Eng. Chem. Process Des. Dev. 24 (1985) 646–651. https://doi.org/10.1021/i200030a020.

[51] I.-Y. Eom, J.-Y. Kim, T.-S. Kim, S.-M. Lee, D. Choi, I.-G. Choi, J.-W. Choi, Effect of essential inorganic metals on primary thermal degradation of lignocellulosic biomass,

Bioresour. Technol. 104 (2012) 687–694. https://doi.org/10.1016/j.biortech.2011.10.035.

[52] J. Bourke, M. Manley-Harris, C. Fushimi, K. Dowaki, T. Nunoura, M.J. Antal, Do all carbonized charcoals have the same chemical structure? 2. A model of the chemical structure of carbonized charcoal, Ind. Eng. Chem. Res. 46 (2007) 5954–5967. https://doi.org/10.1021/ie070415u.

[53] R. Fahmi, A. V. Bridgwater, L.I. Darvell, J.M. Jones, N. Yates, S. Thain, I.S. Donnison, The effect of alkali metals on combustion and pyrolysis of Lolium and Festuca grasses, switchgrass and willow, Fuel. 86 (2007) 1560–1569. https://doi.org/10.1016/J.FUEL.2006.11.030.

[54] M. Asmadi, H. Kawamoto, S. Saka, Pyrolysis reactions of Japanese cedar and Japanese beech woods in a closed ampoule reactor, J. Wood Sci. 56 (2010) 319–330. https://doi.org/10.1007/S10086-009-1097-2/METRICS.

[55] B.H. Davison, S.R. Drescher, G.A. Tuskan, M.F. Davis, N.P. Nghiem, Variation of S/G Ratio and Lignin Content in a *Populus* Family Influences the Release of Xylose by Dilute Acid Hydrolysis, Appl. Biochem. Biotechnol. 130 (2006) 427–435. https://doi.org/10.1385/ABAB:130:1:427.

[56] M.J. Bentley, J.P. Kearns, B.M. Murphy, R.S. Summers, M.J. Bentley, J.P. Kearns, B.M. Murphy, Pre-pyrolysis metal and base addition catalyzes pore development and improves organic micropollutant adsorption to pine biochar, (2021). https://doi.org/10.1016/j.chemosphere.2021.131949.

[57] R. Franklin, Crystallite growth in graphitizing and non-graphitizing carbons, Proc. R. Soc. London. Ser. A. Math. Phys. Sci. 209 (1951) 196–218. https://doi.org/10.1098/rspa.1951.0197.

[58] P.J.F. Harris, Z. Liu, K. Suenaga, Imaging the atomic structure of activated carbon, n.d.

[59] A. Oberlin, High-Resolution TEM Studies of Carbonization and Graphitization, Chem. Phys. Carbon. (1989) 1–143. https://doi.org/10.1201/9781003210122-1.

[60] † P.J.F.H., Fullerene-related structure of commercial glassy carbons, Https://Doi.Org/10.1080/14786430410001720363. 84 (2006) 3159–3167. https://doi.org/10.1080/14786430410001720363.

[61] P.J.F. Harris, Structure of non-graphitising carbons, Int. Mater. Rev. 42 (1997) 206–218. https://doi.org/10.1179/imr.1997.42.5.206.

[62] D.W. Rutherford, R.L. Wershaw, C.E. Rostad, C.N. Kelly, Effect of formation conditions on biochars: Compositional and structural properties of cellulose, lignin, and pine biochars, Biomass and Bioenergy. 46 (2012) 693–701. https://doi.org/10.1016/j.biombioe.2012.06.026.

[63] J. Rouquerol, F. Rouquerol, P. Llewellyn, G. Maurin, K.S.W. Sing, Adsorption by Powders and Porous Solids: Principles, Methodology and Applications: Second Edition, 2013. https://doi.org/10.1016/C2010-0-66232-8.

[64] X. Xiao, B. Chen, Z. Chen, L. Zhu, J.L. Schnoor, Insight into Multiple and Multilevel Structures of Biochars and Their Potential Environmental Applications: A Critical Review, Environ. Sci. Technol. 52 (2018) 5027–5047. https://doi.org/10.1021/acs.est.7b06487.

[65] F. Vallejos-Burgos, N. Díaz-Pérez, Á. Silva-Villalobos, R. Jiménez, X. García, L.R. Radovic, On the structural and reactivity differences between biomass- and coal-derived chars, Carbon N. Y. 109 (2016) 253–263. https://doi.org/10.1016/j.carbon.2016.08.012.

[66] M. Keiluweit, M. Kleber, M.A. Sparrow, B.R.T. Simoneit, F.G. Prahl, Solvent-Extractable

Polycyclic Aromatic Hydrocarbons in Biochar: Influence of Pyrolysis Temperature and Feedstock, Environ. Sci. Technol. 46 (2012) 9333–9341. https://doi.org/10.1021/es302125k.

[67] B. Chen, D. Zhou, L. Zhu, Transitional adsorption and partition of nonpolar and polar aromatic contaminants by biochars of pine needles with different pyrolytic temperatures, Environ. Sci. Technol. 42 (2008) 5137–5143. https://doi.org/10.1021/es8002684.

[68] D.W. Van Krevelen, Graphical-statistical method for the study of structure and reaction processes of coal, Fuel. 29 (1950) 269–284.

[69] J.A. Rehrmann, L.A. Jonas, Dependence of gas adsorption rates on carbon granule size and linear flow velocity, Carbon N. Y. 16 (1978) 47–51. https://doi.org/10.1016/0008-6223(78)90115-X.

[70] L. JONAS, The kinetics of adsorption of carbon tetrachloride and chloroform from air mixtures by activated carbon, J. Catal. 24 (1972) 446–459. https://doi.org/10.1016/0021-9517(72)90128-5.

[71] C. Valderrama, X. Gamisans, X. de las Heras, A. Farrán, J.L. Cortina, Sorption kinetics of polycyclic aromatic hydrocarbons removal using granular activated carbon: Intraparticle diffusion coefficients, J. Hazard. Mater. 157 (2008) 386–396. https://doi.org/10.1016/j.jhazmat.2007.12.119.

[72] T.W. Weber, R.K. Chakravorti, Pore and solid diffusion models for fixed-bed adsorbers, AIChE J. 20 (1974) 228–238. https://doi.org/10.1002/aic.690200204.

[73] M. Domingo-García, A.J. Groszek, F.J. López-Garzón, M. Pérez-Mendoza, Dynamic adsorption of ammonia on activated carbons measured by flow microcalorimetry, Appl. Catal. A Gen. 233 (2002) 141–150.

[74] J. Lehmann, A handful of carbon, Nature. 447 (2007) 143–144. https://doi.org/10.1038/447143a.

[75] R.S. Kookana, A.K. Sarmah, L. Van Zwieten, E. Krull, B. Singh, Biochar application to soil. agronomic and environmental benefits and unintended consequences, Adv. Agron. (2011). https://doi.org/10.1016/B978-0-12-385538-1.00003-2.

[76] Y. Chen, X. Zhang, W. Chen, H. Yang, H. Chen, The structure evolution of biochar from biomass pyrolysis and its correlation with gas pollutant adsorption performance, Bioresour. Technol. 246 (2017) 101–109. https://doi.org/10.1016/j.biortech.2017.08.138.

[77] M. Uchimiya, L.H. Wartelle, V.M. Boddu, Sorption of triazine and organophosphorus pesticides on soil and biochar, J. Agric. Food Chem. (2012). https://doi.org/10.1021/jf205110g.

[78] J.H. Park, G.K. Choppala, N.S. Bolan, J.W. Chung, T. Chuasavathi, Biochar reduces the bioavailability and phytotoxicity of heavy metals, Plant Soil. (2011). https://doi.org/10.1007/s11104-011-0948-y.

[79] N. Alozie, N. Heaney, C. Lin, Biochar immobilizes soil-borne arsenic but not cationic metals in the presence of low-molecular-weight organic acids, Sci. Total Environ. 630 (2018) 1188–1194. https://doi.org/10.1016/j.scitotenv.2018.02.319.

[80] L.R. Radovic, Chemistry & Physics of Carbon, CRC Press, 2007. https://doi.org/10.1201/9781420042993.

[81] A. Dumitrache, H. Akinosho, M. Rodriguez, X. Meng, C.G. Yoo, J. Natzke, N.L. Engle, R.W. Sykes, T.J. Tschaplinski, W. Muchero, A.J. Ragauskas, B.H. Davison, S.D. Brown, Consolidated bioprocessing of Populus using Clostridium (Ruminiclostridium) thermocellum: a case study on the impact of lignin composition and structure, Biotechnol.

Biofuels. 9 (2016) 31. https://doi.org/10.1186/s13068-016-0445-x.

[82] C.G. Yoo, A. Dumitrache, W. Muchero, J. Natzke, H. Akinosho, M. Li, R.W. Sykes, S.D. Brown, B. Davison, G.A. Tuskan, Y. Pu, A.J. Ragauskas, Significance of Lignin S/G Ratio in Biomass Recalcitrance of Populus trichocarpa Variants for Bioethanol Production, ACS Sustain. Chem. Eng. 6 (2018) 2162–2168. https://doi.org/10.1021/acssuschemeng.7b03586.

[83] E. Mészáros, E. Jakab, G. Várhegyi, J. Bourke, M. Manley-Harris, T. Nunoura, M.J. Antal, Do all carbonized charcoals have the same chemical structure? 1. Implications of thermogravimetry-mass spectrometry measurements, Ind. Eng. Chem. Res. 46 (2007) 5943–5953. https://doi.org/10.1021/ie0615842.

[84] S. Wang, K. Wang, Q. Liu, Y. Gu, Z. Luo, K. Cen, T. Fransson, Comparison of the pyrolysis behavior of lignins from different tree species, Biotechnol. Adv. 27 (2009) 562–567. https://doi.org/10.1016/j.biotechadv.2009.04.010.

[85] B. Cagnon, X. Py, A. Guillot, F. Stoeckli, G. Chambat, Contributions of hemicellulose, cellulose and lignin to the mass and the porous properties of chars and steam activated carbons from various lignocellulosic precursors, Bioresour. Technol. 100 (2009) 292–298. https://doi.org/10.1016/J.BIORTECH.2008.06.009.

[86] C.G. Yoo, Y. Yang, Y. Pu, X. Meng, W. Muchero, K.L. Yee, O.A. Thompson, M. Rodriguez, G. Bali, N.L. Engle, E. Lindquist, V. Singan, J. Schmutz, S.P. DiFazio, T.J. Tschaplinski, G.A. Tuskan, J.G. Chen, B. Davison, A.J. Ragauskas, Insights of biomass recalcitrance in natural Populus trichocarpa variants for biomass conversion, Green Chem. 19 (2017) 5467–5478. https://doi.org/10.1039/C7GC02219K.

[87] D.M. Mackay, P. V. Roberts, The dependence of char and carbon yield on lignocellulosic

precursor composition, Carbon N. Y. 20 (1982) 87–94. https://doi.org/10.1016/0008-6223(82)90412-2.

[88] F. Shafizadeh, R.H. Furneaux, T.G. Cochran, J.P. Scholl, Y. Sakai, Production of levoglucosan and glucose from pyrolysis of cellulosic materials, J. Appl. Polym. Sci. 23 (1979) 3525–3539. https://doi.org/10.1002/APP.1979.070231209.

[89] H. Nan, F. Yang, L. Zhao, O. Mašek, X. Cao, Z. Xiao, Interaction of Inherent Minerals with Carbon during Biomass Pyrolysis Weakens Biochar Carbon Sequestration Potential, ACS Sustain. Chem. Eng. 7 (2019) 1591–1599. https://doi.org/10.1021/acssuschemeng.8b05364.

[90] I.-Y.Y. Eom, K.-H.H. Kim, J.-Y.Y. Kim, S.-M.M. Lee, H.-M.M. Yeo, I.-G.G. Choi, J.-W.W. Choi, Characterization of primary thermal degradation features of lignocellulosic biomass after removal of inorganic metals by diverse solvents, Bioresour. Technol. 102 (2011) 3437–3444. https://doi.org/10.1016/j.biortech.2010.10.056.

[91] J. Mcdonald-Wharry, M. Manley-Harris, K. Pickering, Carbonisation of biomass-derived chars and the thermal reduction of a graphene oxide sample studied using Raman spectroscopy, (2013). https://doi.org/10.1016/j.carbon.2013.03.033.

[92] Y. Le Brech, T. Ghislain, S. Leclerc, M. Bouroukba, L. Delmotte, N. Brosse, C. Snape, P. Chaimbault, A. Dufour, Effect of Potassium on the Mechanisms of Biomass Pyrolysis Studied using Complementary Analytical Techniques, ChemSusChem. 9 (2016) 863–872. https://doi.org/10.1002/cssc.201501560.

[93] J. Cao, G. Xiao, X. Xu, D. Shen, B. Jin, Study on carbonization of lignin by TG-FTIR and high-temperature carbonization reactor, Fuel Process. Technol. 106 (2013) 41–47. https://doi.org/10.1016/j.fuproc.2012.06.016.

[94] H. Kawamoto, Lignin pyrolysis reactions, J. Wood Sci. 63 (2017) 117–132. https://doi.org/10.1007/s10086-016-1606-z.

[95] M. Asmadi, H. Kawamoto, S. Saka, Thermal reactions of guaiacol and syringol as lignin model aromatic nuclei, J. Anal. Appl. Pyrolysis. 92 (2011) 88–98. https://doi.org/10.1016/J.JAAP.2011.04.011.

[96] T. Hosoya, H. Kawamoto, S. Saka, Role of methoxyl group in char formation from lignin-related compounds, J. Anal. Appl. Pyrolysis. 84 (2009) 79–83. https://doi.org/10.1016/J.JAAP.2008.10.024.

[97] K. Li, H. Li, M. Sun, J. Zhang, H. Zhang, S. Ren, M. Barati, Atomic-Scale Understanding about Coke Carbon Structural Evolution by Experimental Characterization and ReaxFF Molecular Dynamics, (2019). https://doi.org/10.1021/acs.energyfuels.9b03154.

[98] J.A. Lacey, J.E. Aston, V.S. Thompson, Wear properties of ash minerals in biomass, Front. Energy Res. 6 (2018) 119. https://doi.org/10.3389/FENRG.2018.00119/BIBTEX.

[99] L. Jiang, S. Hu, L. shi Sun, S. Su, K. Xu, L. mo He, J. Xiang, Influence of different demineralization treatments on physicochemical structure and thermal degradation of biomass, Bioresour. Technol. 146 (2013) 254–260. https://doi.org/10.1016/J.BIORTECH.2013.07.063.

[100] K. Miura, M. Aimi, T. Naito, K. Hashimoto, Steam gasification of carbon: Effect of several metals on the rate of gasification and the rates of CO and CO2 formation, Fuel. 65 (1986) 407–411. https://doi.org/10.1016/0016-2361(86)90304-2.

[101] M. Uchimiya, A. Orlov, G. Ramakrishnan, K. Sistani, In situ and ex situ spectroscopic monitoring of biochar’s surface functional groups, J. Anal. Appl. Pyrolysis. 102 (2013) 53–59. https://doi.org/10.1016/J.JAAP.2013.03.014.

[102] P.J. Mitchell, T.S.L. Dalley, R.J. Helleur, Preliminary laboratory production and characterization of biochars from lignocellulosic municipal waste, J. Anal. Appl. Pyrolysis. 99 (2013) 71–78. https://doi.org/10.1016/j.jaap.2012.10.025.

[103] Y.F. Huang, W.H. Kuan, P.T. Chiueh, S.L. Lo, Pyrolysis of biomass by thermal analysis–mass spectrometry (TA–MS), Bioresour. Technol. 102 (2011) 3527–3534. https://doi.org/10.1016/J.BIORTECH.2010.11.049.

[104] H. Aso, K. Matsuoka, A. Tomita, Quantitative Analysis of Hydrogen in Carbonaceous Materials: Hydrogen in Anthracite, Energy and Fuels. 17 (2003) 1244–1250. https://doi.org/10.1021/EF020285W.

[105] S.. Gregg, K.S.W. Sing, Adsorption, Surface Area and Porosity, 2nd ed., Academic Press, London, 1982.

[106] M. Safar, B.-J. Lin, W.-H. Chen, D. Langauer, J.-S. Chang, H. Raclavska, A. Pétrissans, P. Rousset, M. Pétrissans, Catalytic effects of potassium on biomass pyrolysis, combustion and torrefaction, (2018). https://doi.org/10.1016/j.apenergy.2018.10.065.

[107] G.S. Szymański, Z. Karpiński, S. Biniak, A. Świątkowski, The effect of the gradual thermal decomposition of surface oxygen species on the chemical and catalytic properties of oxidized activated carbon, Carbon N. Y. 40 (2002) 2627–2639. https://doi.org/10.1016/S0008-6223(02)00188-4.

[108] G.S. Szymanski, Z. Karpinski, S. «aw Biniak, A.S. Swia¸tkowski, T he effect of the gradual thermal decomposition of surface oxygen species on the chemical and catalytic properties of oxidized activated carbon, Carbon N. Y. 40 (2002) 2627–2639.

[109] N.M.J.M.J. Conway, A.C.C. Ferrari, A.J.J. Flewitt, J. Robertson, W.I.I. Milne, A. Tagliaferro, W. Beyer, Defect and disorder reduction by annealing in hydrogenated

tetrahedral amorphous carbon, Diam. Relat. Mater. 9 (2000) 765–770. https://doi.org/10.1016/S0925-9635(99)00271-X.

[110] D. Yao, Q. Hu, D. Wang, H. Yang, C. Wu, X. Wang, H. Chen, Hydrogen production from biomass gasification using biochar as a catalyst/support, Bioresour. Technol. 216 (2016) 159–164. https://doi.org/10.1016/J.BIORTECH.2016.05.011.

[111] C.E. Brewer, K. Schmidt-Rohr, J.A. Satrio, R.C. Brown, Characterization of biochar from fast pyrolysis and gasification systems, Environ. Prog. Sustain. Energy. 28 (2009) 386–396. https://doi.org/10.1002/ep.10378.

[112] D. Lin-Vien, N.B. Colthup, W.G. Fateley, J.G. (Professor) Grasselli, The Handbook of infrared and raman characteristic frequencies of organic molecules, (1991) 503.

[113] A. Adrián Barroso-Bogeat, M. Alexandre-Franco, C. Fernándezfernández-Gonzaíez, V. Gómezgómez-Serrano, FT-IR Analysis of Pyrone and Chromene Structures in Activated Carbon, (2014). https://doi.org/10.1021/ef5004733.

[114] A.C. Ferrari, S.E. Rodil, J. Robertson, Interpretation of infrared and Raman spectra of amorphous carbon nitrides, Phys. Rev. B. 67 (2003) 155306. https://doi.org/10.1103/PhysRevB.67.155306.

[115] A.C. Ferrari, D.M. Basko, Raman spectroscopy as a versatile tool for studying the properties of graphene, Nature Publishing Group, 2013. https://doi.org/10.1038/nnano.2013.46.

[116] A.C. Ferrari, Raman spectroscopy of graphene and graphite: Disorder, electron–phonon coupling, doping and nonadiabatic effects, Solid State Commun. 143 (2007) 47–57. https://doi.org/10.1016/j.ssc.2007.03.052.

[117] A.C. Ferrari, J. Robertson, Interpretation of Raman spectra of disordered and amorphous

carbon, Phys. Rev. B. 61 (2000) 14095–14107. https://doi.org/10.1103/PhysRevB.61.14095.

[118] F. Tuinstra, J.L. Koenig, Raman Spectrum of Graphite, J. Chem. Phys. 53 (1970) 1126–1130. https://doi.org/10.1063/1.1674108.

[119] M.W. Smith, I. Dallmeyer, T.J. Johnson, C.S. Brauer, J.S. McEwen, J.F. Espinal, M. Garcia-Perez, Structural analysis of char by Raman spectroscopy: Improving band assignments through computational calculations from first principles, Carbon N. Y. 100 (2016) 678–692.

[120] C. Castiglioni, M. Tommasini, G. Zerbi, Raman spectroscopy of polyconjugated molecules and materials: confinement effect in one and two dimensions, Philos. Trans. R. Soc. London. Ser. A Math. Phys. Eng. Sci. 362 (2004) 2425–2459. https://doi.org/10.1098/RSTA.2004.1448.

[121] A.C. Ferrari, J. Robertson, Raman spectroscopy of amorphous, nanostructured, diamond–like carbon, and nanodiamond, Philos. Trans. R. Soc. London. Ser. A Math. Phys. Eng. Sci. 362 (2004) 2477–2512. https://doi.org/10.1098/rsta.2004.1452.

[122] D. Coskun, D.T. Britto, W. Shi, H.J. Kronzucker, Nitrogen transformations in modern agriculture and the role of biological nitrification inhibition, Nat. PLANTS. 3 (2017) 17074. https://doi.org/10.1038/nplants.2017.74.

[123] L. Zhang, S. Tang, Y. Guan, Excellent Adsorption-Desorption of Ammonium by a Poly(acrylic acid)-Grafted Chitosan and Biochar Composite for Sustainable Agricultural Development, ACS Sustain. Chem. Eng. 8 (2020) 16451–16462. https://doi.org/10.1021/ACSSUSCHEMENG.0C05070/ASSET/IMAGES/ACSSUSCHEMENG.0C05070.SOCIAL.JPEG_V03.

[124] Y. Guo, B. Mu, P. Liu, L. Luo, L. Hao, Y. Li, T. Zhu, Ammonia emission estimation for the cement industry in northern China, Atmos. Pollut. Res. 11 (2020) 1738–1742. https://doi.org/10.1016/J.APR.2020.07.006.

[125] J.L. Cheney, K.T. Knapp, A Study of Ammonia Source at a Portland Cement Production Plant, Http://Dx.Doi.Org/10.1080/08940630.1987.10466324. 37 (2012) 1298–1302. https://doi.org/10.1080/08940630.1987.10466324.

[126] L. Verhoeven, P. Lodewyckx, USING THE WHEELER-JONAS EQUATION TO DESCRIBE ADSORPTION OF INORGANIC MOLECULES: AMMONIA, (n.d.). https://www.researchgate.net/publication/268012563 (accessed November 5, 2021).

[127] J.C. Crittenden, R.R. Trussell, D.W. Hand, K.J. Howe, G. Tchobanoglous, MWH's Water Treatment: Principles and Design: Third Edition, 2012. https://doi.org/10.1002/9781118131473.

[128] A. Wheeler, A.J. Robell, Performance of fixed-bed catalytic reactors with poison in the feed, J. Catal. 13 (1969) 299–305. https://doi.org/10.1016/0021-9517(69)90404-7.

[129] G.O. Wood, E.S. Moyer, A Review of the Wheeler Equation and Comparison of Its Applications to Organic Vapor Respirator Cartridge Breakthrough Data, Am. Ind. Hyg. Assoc. J. 50 (1989) 400–407. https://doi.org/10.1080/15298668991374886.

[130] P. Lodewyckx, G.O. Wood, S.K. Ryu, The Wheeler–Jonas equation: a versatile tool for the prediction of carbon bed breakthrough times, Carbon N. Y. 42 (2004) 1351–1355. https://doi.org/10.1016/j.carbon.2004.01.016.

[131] Y.H. Yoon, J.H. Nelson, Application of Gas Adsorption Kinetics I. A Theoretical Model for Respirator Cartridge Service Life, Https://Doi.Org/10.1080/15298668491400197. 45 (2010) 509–516. https://doi.org/10.1080/15298668491400197.

[132] Y.H. Yoon, J.H. Nelson, Application of Gas Adsorption Kinetics — II. A Theoretical Model for Respirator Cartridge Service Life and Its Practical Applications, Https://Doi.Org/10.1080/15298668491400205. 45 (2010) 517–524. https://doi.org/10.1080/15298668491400205.

[133] P. Lodewyckx, E.F. Vansant, Influence of humidity on adsorption capacity from the Wheeler-Jonas model for prediction of breakthrough times of water immiscible organic vapors on activated carbon beds, Am. Ind. Hyg. Assoc. J. 60 (1999) 612–617. https://doi.org/10.1080/00028899908984480.

[134] P. Lodewyckx, E.F. Vansant, The Influence of Humidity on the Overall Mass Transfer Coefficient of the Wheeler-Jonas Equation, (2000). https://doi.org/10.1080/15298660008984556.

[135] N. Stiles Wilkins, A. Rajendran, S. Farooq, Dynamic column breakthrough experiments for measurement of adsorption equilibrium and kinetics, 27 (2021) 397–422. https://doi.org/10.1007/s10450-020-00269-6.

[136] A. Wheeler, A.J. Robell, Performance of fixed-bed catalytic reactors with poison in the feed, J. Catal. 13 (1969) 299–305. https://doi.org/10.1016/0021-9517(69)90404-7.

[137] G.O. Wood, Quantification and application of skew of breakthrough curves for gases and vapors eluting from activated carbon beds, Carbon N. Y. 40 (2002) 1883–1890. https://doi.org/10.1016/S0008-6223(02)00031-3.

7. Appendix A: Supplemental Information for Chapter 2

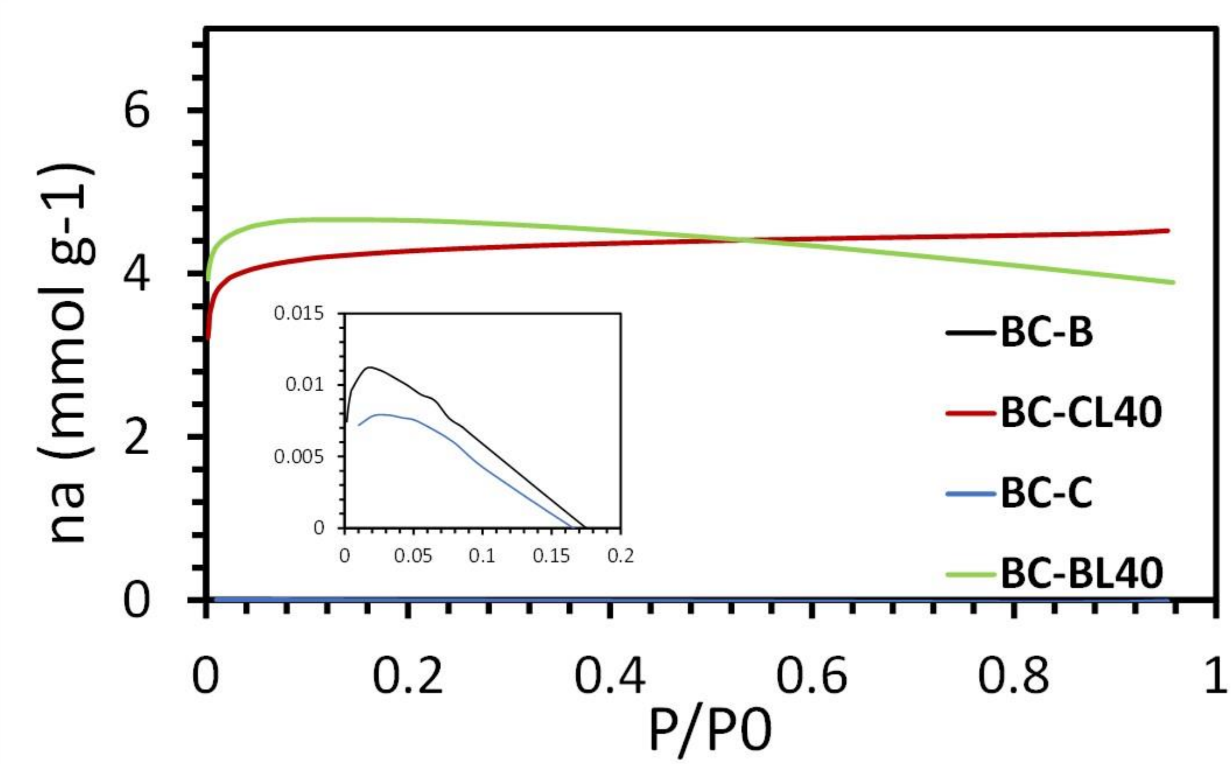

Figure 26: N₂ adsorption isotherms for untreated and demineralized biochars in Chapter 2. The isotherms for demineralized chars are shown in the primary graph, while those for untreated chars are shown in the inset. Note the very low N₂ adsorption for untreated chars, indicating largely non-porous particles.

8. Appendix B: Supplemental Information for Chapter 3

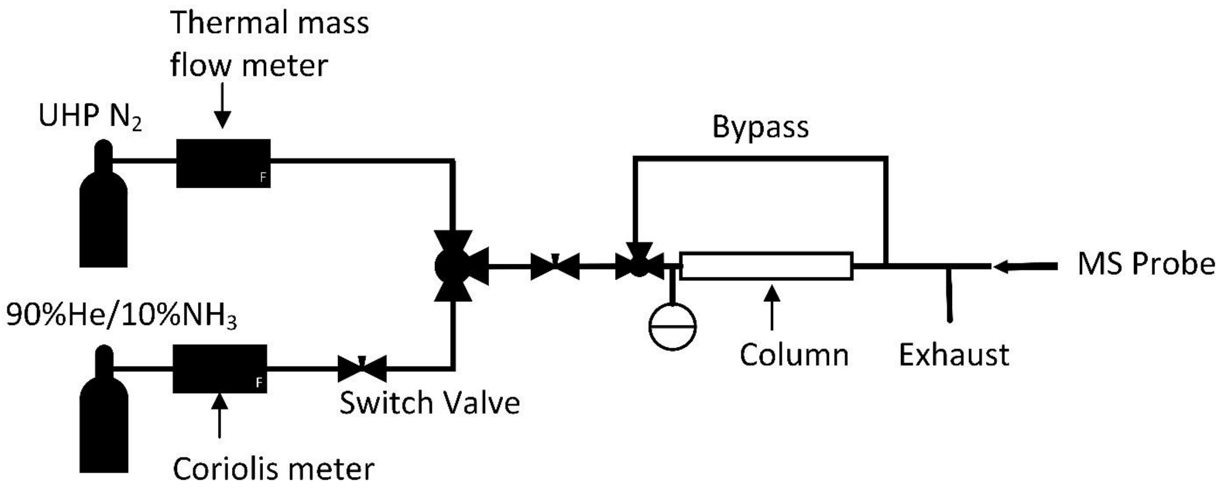

Figure 27: Schematic of experimental apparatus for NH_3 breakthrough experimentation

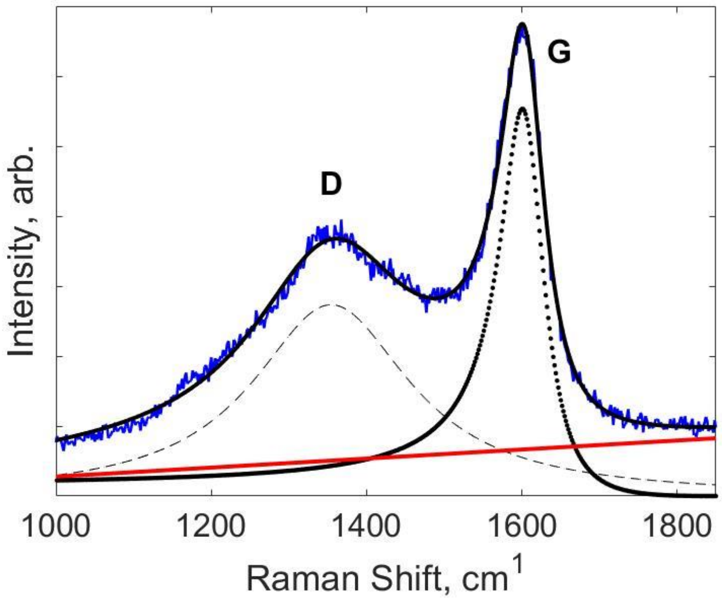

Figure 28: Sample Raman fit using a Lorentzian for the D band, Breit-Wigner-Fano function for the G band, and a linear background to account for photoluminescence.

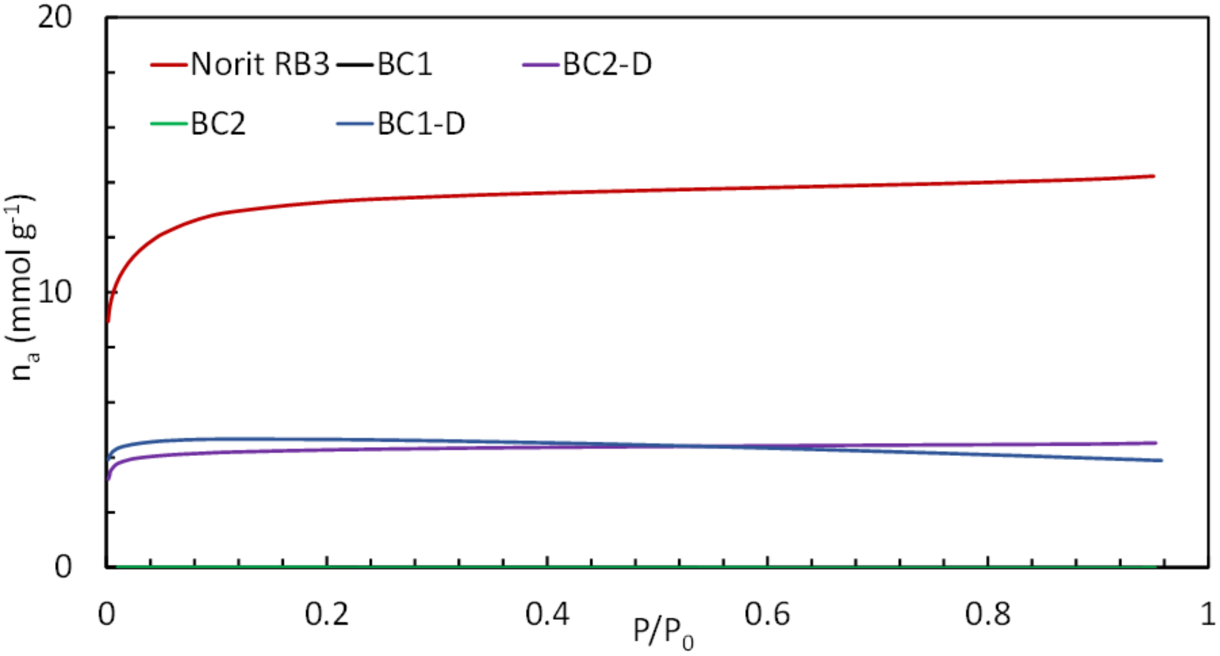

Figure 29: N$_2$ adsorption isotherms for all biochars and Norit RB3. The N$_2$ adsorption for BC1 and BC2 was extremely low, indicating a largely non-porous material.

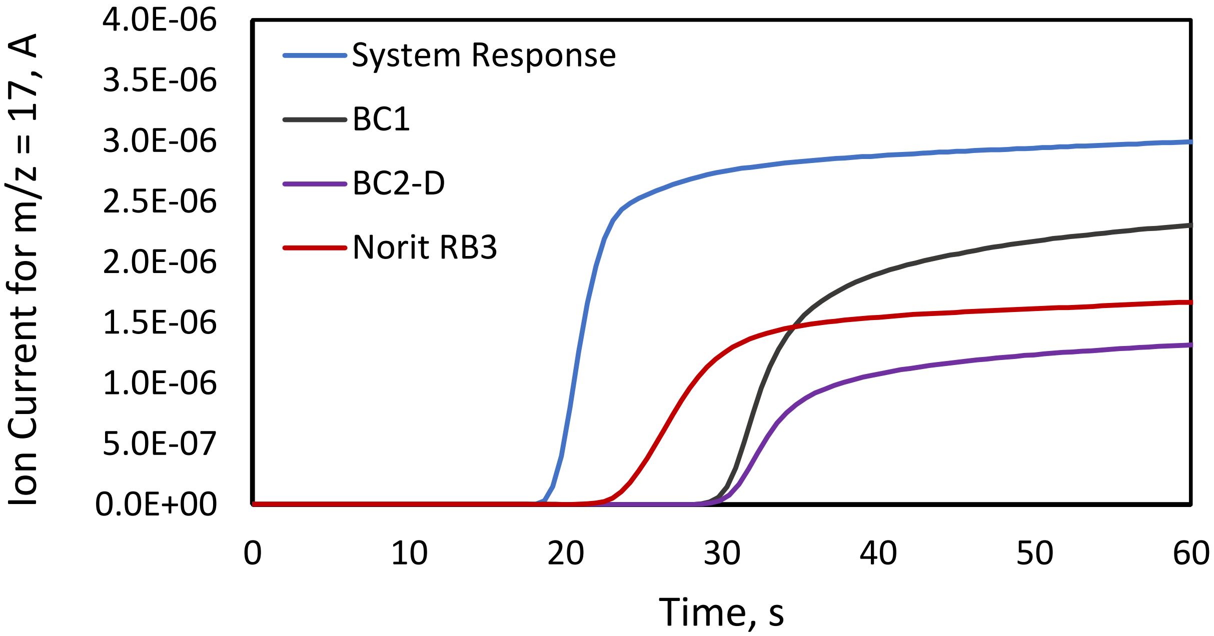

Figure 30: Raw MS ion current data showing system response compared to breakthrough curves for three representative materials.

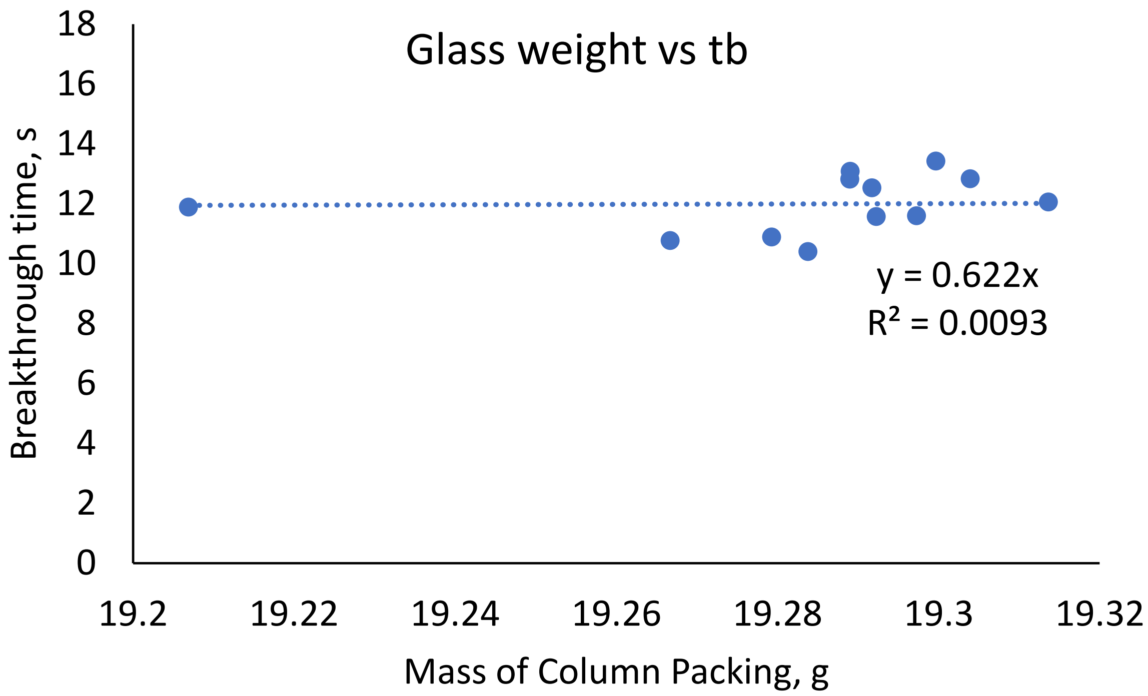

Figure 31: Breakthrough time vs. column packing with very weak correlation, indicating mass of packing material may not be a source of error.

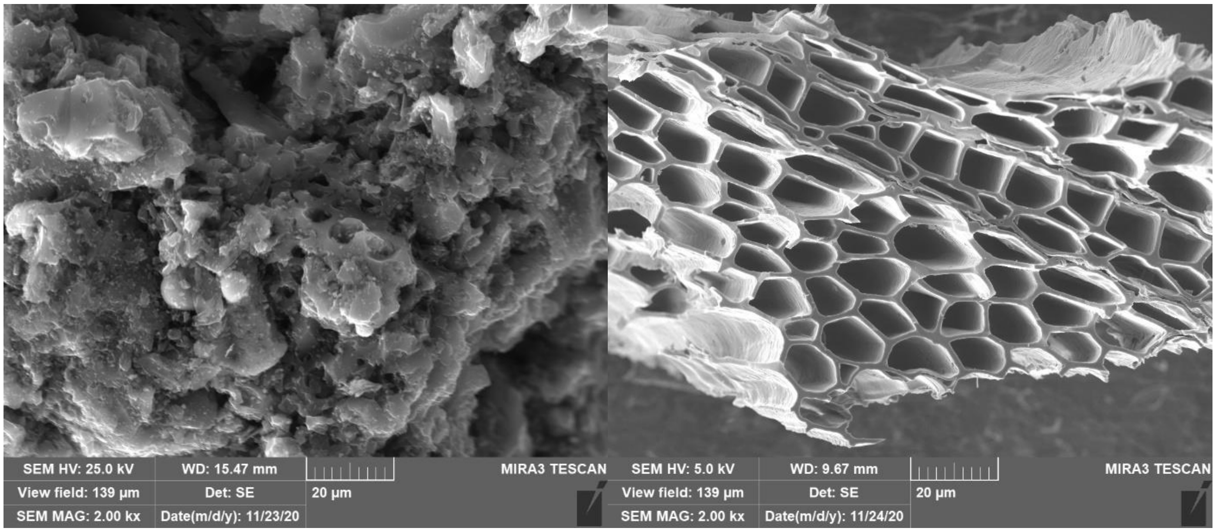

Figure 32: Scanning electron microscope micrographs of Norit RB3, left, and BC2, right, at 2kx magnification

9. Appendix C: Supplemental Information for Chapter 4

9.1. X-ray Diffraction – Peak Fitting Methods

Peak-fitting of X-ray diffraction patterns was done for the (002) and (300) reflections. Due to overlapping peaks, it was necessary to fit the entire band between 30 – 35 degrees 2θ. Peaks were fit using OriginPro, using non-linear regression by a built-in algorithm. Peak parameters plus standard error were found using a Levenberg-Marquardt algorithm which minimizes the χ^2 value. Each region was fit with the appropriate number of Lorentzian peaks plus a linear background to account for instrument background. A Lorentzian line shape, equation S1, was used because it gave a better fit than a Gaussian.

Eq. 7 $$\boldsymbol{I(2\theta) = \frac{2A}{\pi}\frac{\Gamma}{(4(x-x_0)^2+\Gamma^2)}}$$

where A is the peak area, x_0 is the peak position, and Γ is the full width at half the maximum intensity. Only peak position and FWHM were reported for each material.

The peak position relates to the spacing of lattice planes according to the Bragg condition by the Bragg equation:

Eq. 8 $$\boldsymbol{n\lambda = 2dsin\theta}$$

where n = 1, λ is the characteristic wavelength for Cu-K$_\alpha$ radiation – 1.5406 Å, d is the lattice spacing, and θ is one half the calculated peak position. The lattice spacing, d, is then applied to the formula for lattice parameter of a hexagonal unit cell using (h k l) = (002) for the c-axis parameter or (h k l) = (300) for the a-axis parameter:

Eq. 9 $$\boldsymbol{\frac{1}{d^2} = \frac{4(h^2+hk+k^2)}{3a^2} + \frac{l^2}{c^2}}$$

which give $a = 2\sqrt{3}d$ and $c = 2d$.

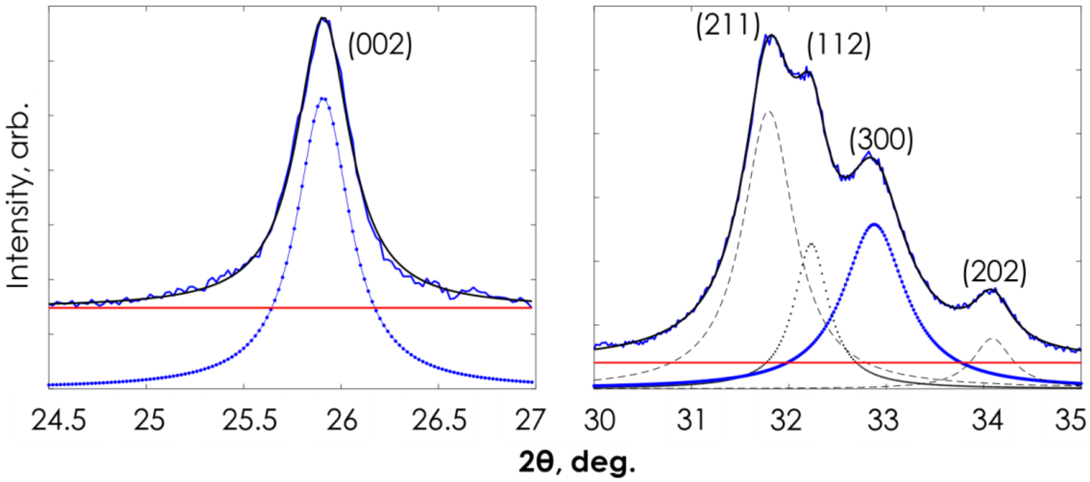

Figure 33: Sample result of XRD peak fitting for BC750. Lorentzian line shapes were found to give the best fit for all materials.

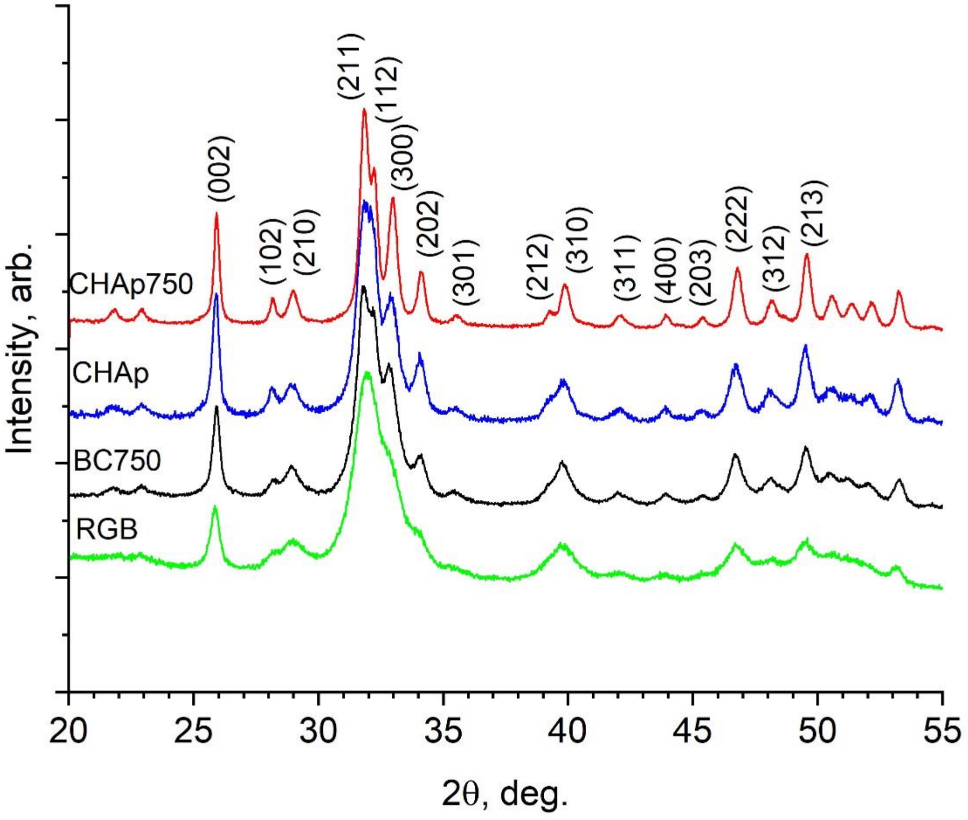

Figure 34: XRD patterns for all materials with some reflections annotated.

Table XVI: FWHM for fitted XRD peaks plus correlation coefficients

	Full Width at Half Peak Maximum, (degrees)		
Material	**(300)**	**(002)**	**R^2 for peak fit, (300)/(002)**
RGB	1.2089±0.0632	0.4218±0.0074	0.9986/0.9912
BC750	0.7798±0.0106	0.3298±0.0039	0.9992/0.9959
CHAp	0.6308±0.0146	0.3081±0.0050	
CHAp750	0.3768±0.0071	0.2436±0.0030	0.9964/0.9955

9.2. DRIFTS Spectroscopy

9.2.1. Carbonate *v*2 – Peak Fitting Results

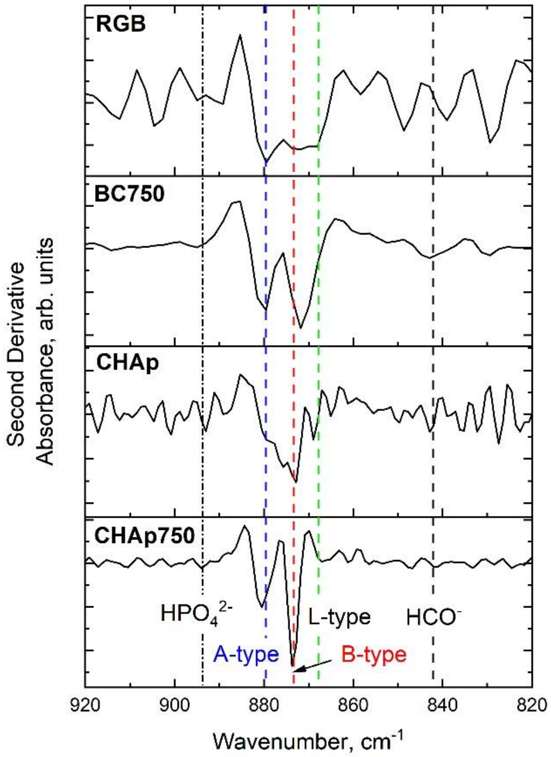

Figure 35: The second derivative of DRIFTS spectra in the v2 CO band were used to guide and streamline curve-fitting efforts. Five physically meaningful bands in this region were tracked, including a one possibly due to HPO_4^{2-}. A-type, B-type and labile carbonate (L-type) are present in all materials.

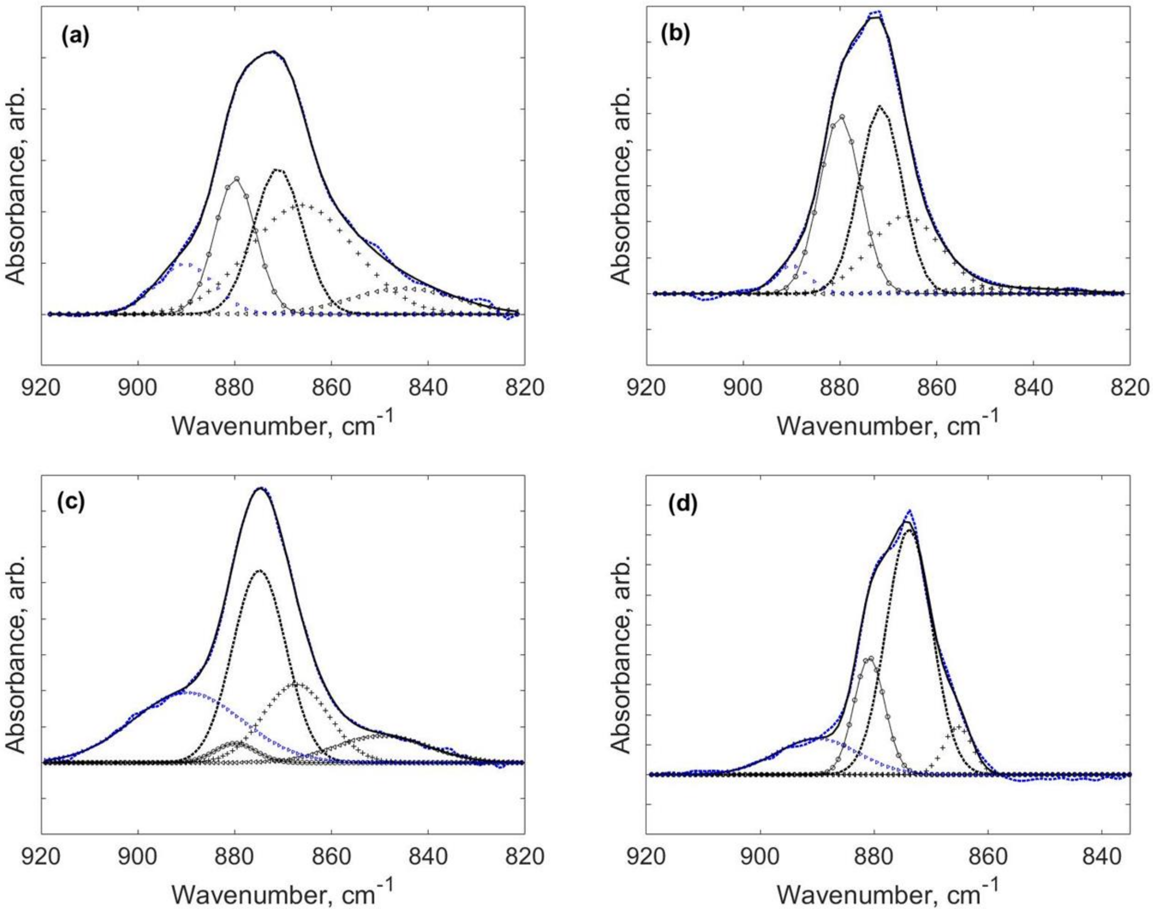

Figure 36: Graphical results of peak fitting for v2 CO_3^{2-} IR modes for all materials.

9.2.2. DRIFTS Spectra of D-BC750 and Wood-based biochar

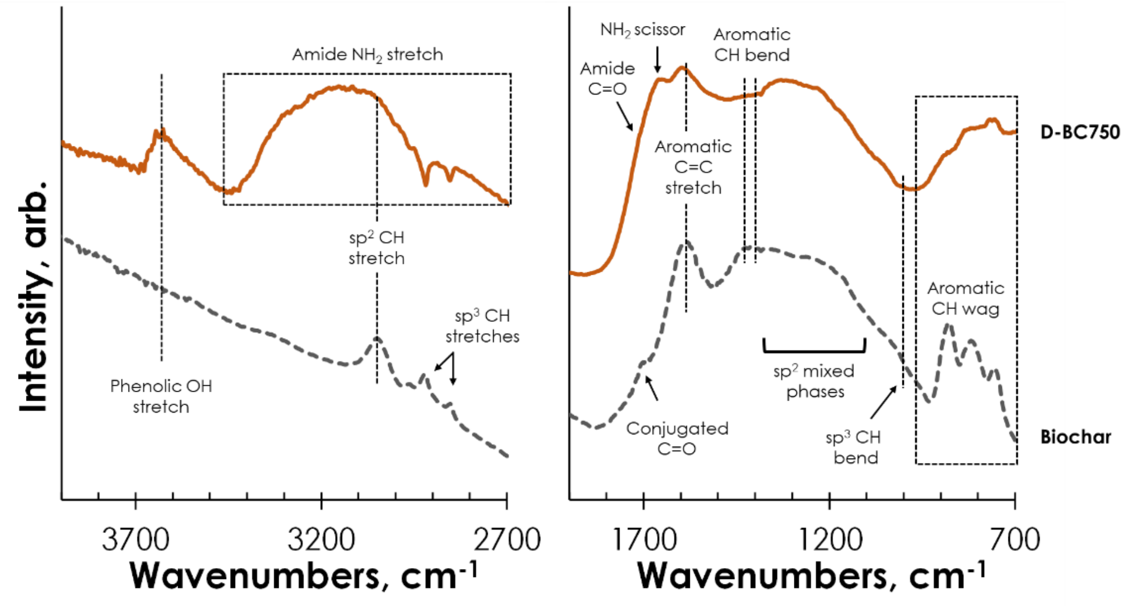

Figure 37: DRIFTS spectra of D-BC750 and biochar. The biochar spectrum was used to illustrate the presence of aromatic clusters and amine and/or amide groups in the bone char carbonaceous phase.

9.3. Nitrogen Physisorption Measurements

Both CHAp and BC750 are primarily mesoporous, showing IUPAC Type IV isotherms that exhibit H1 hysteresis [7].

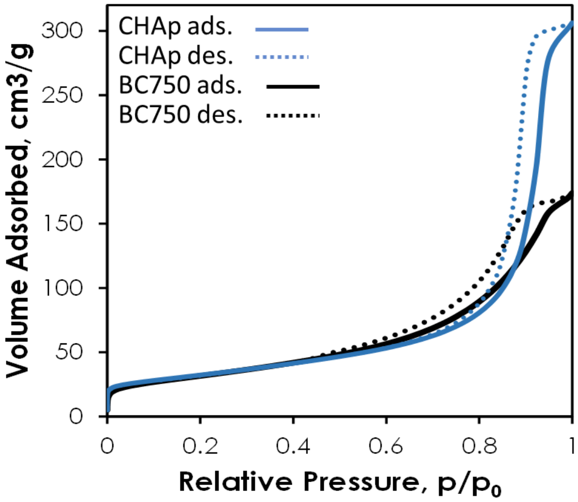

Figure 38: N_2 adsorption/desorption isotherms for CHAp (blue) and BC750 (black). Adsorption follows the solid lines while desorption follows the dotted lines.

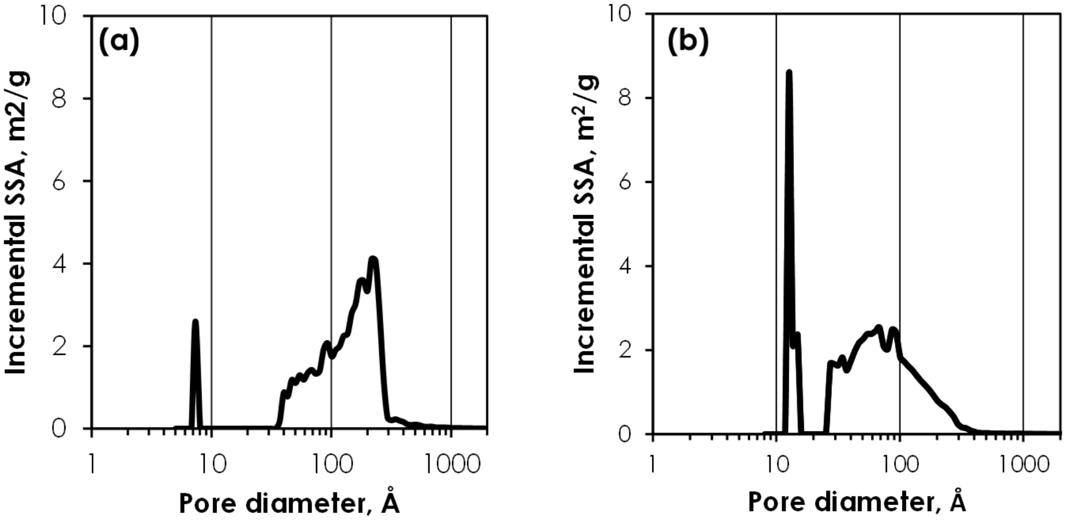

Figure 39: Incremental specific surface area for (a) CHAp, and (b) BC750.

9.4. Raman Fitting

The mathematical form for the BWF function is used to fit the G-peak in all Raman spectra is

Eq. 10

$$\boldsymbol{I(\omega) = \frac{I_0[1+2(\omega-\omega_0/Q\Gamma)]^2}{1+[2(\omega-\omega_0/\Gamma)]^2}}$$

where I_0 is the peak intensity, ω_0 is the peak position, and Γ is the full width at half the peak maximum (FWHM). Q is known as the BWF coupling coefficient which creates a residual intensity in the tail region of the asymmetric line shape. For residual intensity on the lower wavenumber side, Q will be negative. Because of the asymmetry of the BWF lineshape the position of the peak is not the position of the maximum, ω_{max}. The position of the peak maximum is calculated as

Eq. 11

$$\boldsymbol{\omega_{max} = \omega_0 + \Gamma/2Q}$$

The negative value for Q indicates that the peak maximum is at a lower wavenumber than the peak position.

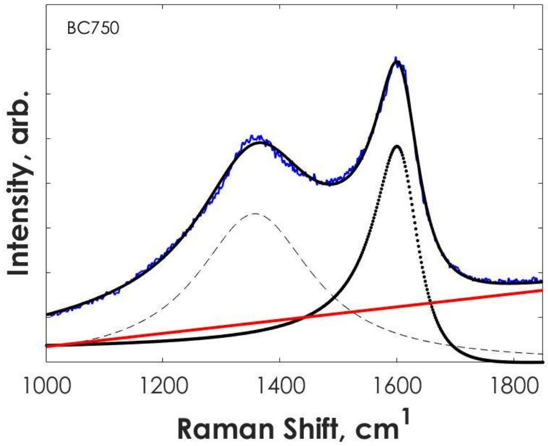

Figure 40: Raman spectrum for BC750 with fitted model and component D and G peaks plus linear background.

9.5. Thermal Analysis TGA and DTG Curves

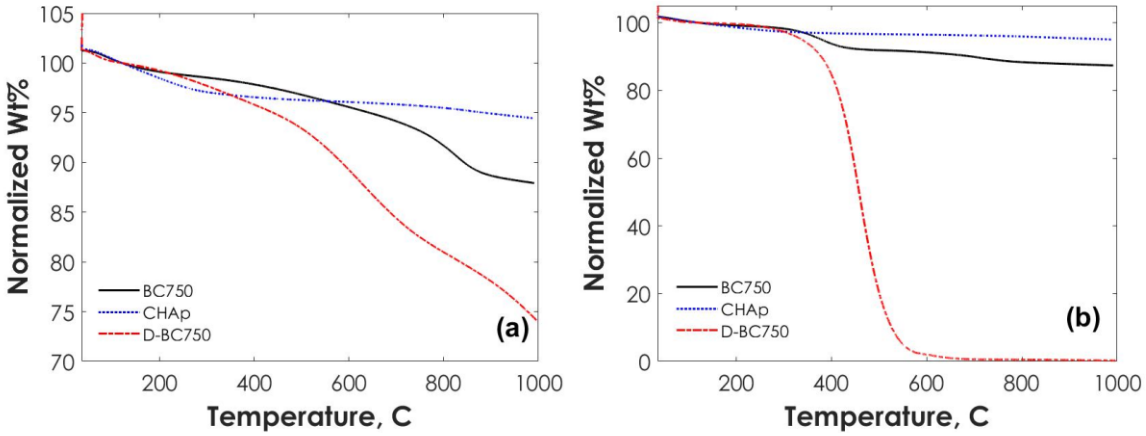

Figure 41: TGA weight loss curves for BC750, CHAp, and D-BC750 in dry argon (left) and 90% O_2 (right), normalized to 120°C

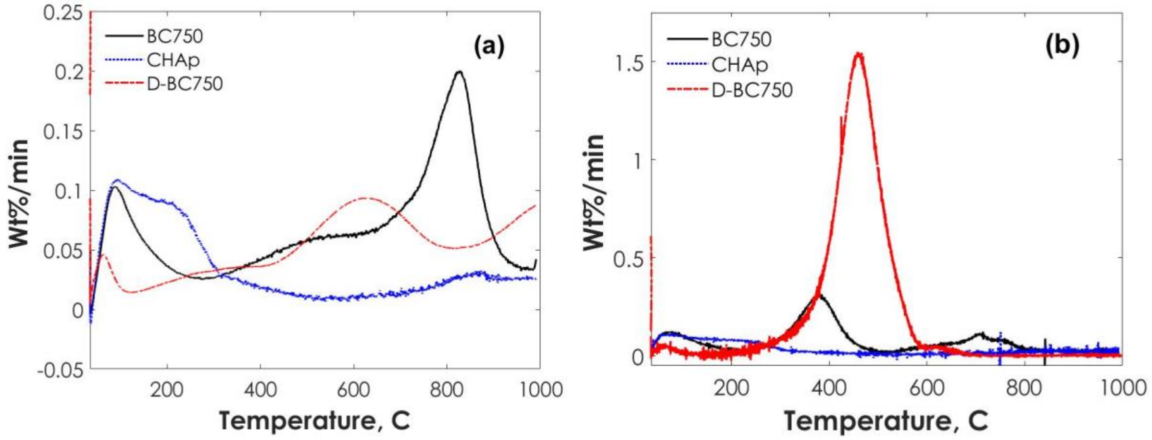

Figure 42: DTG curves for BC750, CHAp, D-BC750 in dry argon (left) and in 90% O_2 (right).